Attosecond Time-Resolved Measurements

Jan Conrad Baggesen

. . .

PhD Thesis

Department of Physics and Astronomy
Aarhus University
July 25, 2011.

This thesis is submitted to the Faculty of Science at Aarhus University, Denmark, in order to fulfill the requirements for obtaining the PhD degree in physics. The studies have been carried out under the supervision of Lars Bojer Madsen at the Department of Physics and Astronomy.

Contents

Preface

This thesis presents the work I have done during my PhD studies at the Department of Physics and Astronomy, Aarhus University, Denmark, under the supervision of Lars Bojer Madsen.

Notation

Atomic units (a.u.) used throughout this thesis, unless indicated otherwise. In atomic units the electron mass, m_e, the elementary charge, e, the reduced Planck's constant, $\hbar$, and the Bohr radius, a_0, all equal unity.

It is customary to use W/cm^2 to give the intensity of laser pulses. The laser field strength (in atomic units) is related to the intensity (in W/cm^2) through $\mathcal{E}_0 = \sqrt{\frac{I}{3.51\times10^{16}}}$. Most of the laser pulses considered here are centred around 800 nm and are in the infrared. We will still refer to them as laser pulses.

All of the streaking spectra plotted throughout this thesis are in arbitrary units when it comes to the strength of the signal. They are all plotted on a linear scale and has dark blue corresponding to 0 and dark red corresponding to 1 in normalised units. The colour scale is indicated in Fig. 1.

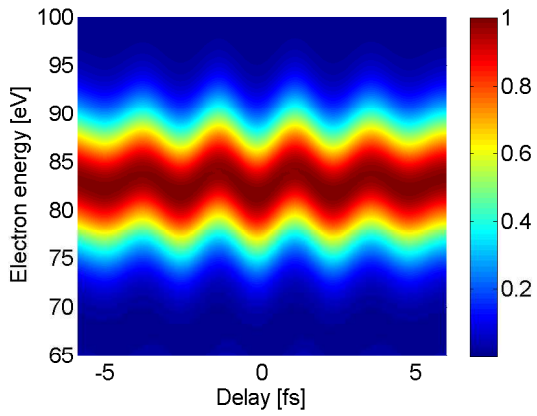

Figure 1 | This figure illustrates the color scale used throughout the thesis.

Acknowledgements

I would like to use this opportunity to thank my supervisor Lars Bojer Madsen for leading me into the subject of attosecond physics and for his inspiring guidance throughout my PhD studies.

Very many friends and colleagues have contributed to making my eight years at Aarhus University both educational and fun. I would like to thank my fellow students for making my time in the office enjoyable, even when the physics was not. This goes for my officemates, the Friday Bar and the friends from my secondary office, TÅGEKAMMERET.

I thank Adam Etches, Niels Baggesen, and Lisbeth Munksgaard Nielsen for proofreading this thesis, but mostly I thank Lisbeth for her loving support especially in the last couple of months.

List of Publications

As part of my PhD studies I have published the following papers. The first five papers serve as part of this thesis and several passages and figures are reused directly from the papers.

A) **Jan Conrad Baggesen and Lars Bojer Madsen**
Theory for time-resolved measurements of laser-induced electron emission from metal surfaces.
Phys. Rev. A **78**, 032903 (2008).

B) **Jan Conrad Baggesen and Lars Bojer Madsen**
Secondary-electron cascade in attosecond photoelectron spectroscopy from metals.
Phys. Rev. A **80**, 030901(R) (2009).

C) **Jan Conrad Baggesen and Lars Bojer Madsen**
Polarization effects in attosecond photoelectron spectroscopy.
Phys. Rev. Lett. **104**, 043602 (2010).

D) **Jan Conrad Baggesen and Lars Bojer Madsen**
Atomic and molecular phases through attosecond streaking.
Phys. Rev. A **83**, 021403(R) (2011).

E) **Jan Conrad Baggesen and Lars Bojer Madsen**
On the dipole, velocity and acceleration forms in high-order harmonic generation from a single atom or molecule.
J. Phys. B: At. Mol. Opt. Phys. **44**, 115601 (2011).

F) **Jan Conrad Baggesen, Eva Lindroth, and Lars Bojer Madsen**
Theory for absorption spectroscopy in krypton.
In preparation.

Unrelated to the work presented in the thesis, I have published another paper covering work primarily done as an undergraduate student.

G) **Jan Conrad Baggesen and Allan Hvidkjær Sørensen**
Influence of atomic screening on fragmentation of ultrarelativistic lead ions in LHC collimators.
Nucl. Instr. and Meth. B **267**(16), 2662-2666 (2009).

Chapter

1 Introduction

Around the turn of the millenium, the advances in intense few-cycle laser pulses lead to the generation of attosecond pulse trains and isolated attosecond pulses[1, 2], where 1 asec is 10^{-18} s. With attosecond pulses it becomes possible to investigate electronic motion at the natural timescale. The atomic unit of time is 24 asec and the Bohr orbit time of the hydrogen 1s electron is $T = 2\pi a_0/v_0 = 150$ asec, where a_0 is the Bohr radius and v_0 the Bohr velocity. The goal of attoscience is to try to understand the evolution of atomic, molecular and solid systems on this timescale. This chapter is a short introduction to some aspects of attosecond physics and shows how the next chapters fit into this context.

1.1 Attosecond Physics

Attosecond pulses are generated from intense few-cycle laser pulses, typically from titanium-sapphire lasers operating at a wavelength of 800 nm, through the process of high-order harmonic generation (HHG). The HHG process is not very efficient and the attosecond pulses are therefore weak and in the perturbative regime, where no more than one photon is absorbed by each atom or molecule. The pulses are typically in the extreme ultra-violet (XUV) regime with a central photon energy of 30-100 eV, corresponding to the 20th to the 60th harmonic of the fundamental

laser pulse. The shortest attosecond pulses have a duration around 80 asec full-width-at-half-maximum (FWHM), but more often the duration is a few hundred attoseconds. The duration of the attosecond pulses is much shorter than the optical period of the fundamental field (2.67 fs at 800 nm), allowing the attosecond pulses to resolve the oscillations of the fundamental field.

The fact that the attosecond pulses are created from the intense laser pulses is the key to most attosecond experiments. The intense laser pulse coming out of the oscillator is split into two at a ratio of about 10:1. The intense part is used for HHG to generate an attosecond pulse, while the other part is sent through a delay line onto the target. Varying the length of the delay line allows a very precise timing between the arrival of the (still rather intense) laser pulse and the generated attosecond pulse. The signal recorded in the experiments is for example the photoelectron energy[3–9], the ion production[10], the molecular fragmentation[11], or the photon absorption[12–14] measured as a function of the relative delay between the two pulses.

The process where an isolated attosecond pulse is used to ionise the target and release electrons into the continuum dressed by the laser pulse is known as attosecond streaking. Looking at it classically, if an electron is released at a time t_0 by the attosecond pulse, it will then be accelerated by the laser pulse from the time of release until the laser pulse is over. The momentum gained in this acceleration (neglecting any effects of the target left behind) is $\Delta\vec{k} = -e\int_{t_0}^{\infty}\vec{\mathcal{E}}(t')dt'$, where $-e$ is the electron charge and $\vec{\mathcal{E}}(t)$ is the electric field due to the laser pulse. When varying the time of ionisation (the attosecond pulse) relative to the laser pulse, one can directly map out the integral of the electric field, which is also the vector potential of the laser pulse[5]. If the attosecond pulse releases electrons from two different initial states, then a delay in the release time will show up as a shift in the streaking spectrum from the different channels. Measuring these shifts allows the timing of very small differences in the release time and has been used to measure the difference in release time for core and valence electrons in tungsten[6] and the difference in ionisation time for electrons from the 2s or 2p shell in neon[8]. The attosecond streaking technique will be the subject of chapter 2, while chapter 3 is dedicated to understanding the time-

resolved measurements from condensed matter and chapter 4 will discuss how secondary electrons may influence the measurements.

Chapter 5 will discuss other effects that may lead to shifts in the streaking spectrum. These include effects of a permanent dipole moment in the initial state, the Coulomb potential of the ion, and the structure of the continuum. Experiments have measured the ionisation time in strong-field ionisation of helium[15] and found that there is no delay once the Coulomb potential is properly included[16]. Similarly, the interpretation of the streaking measurements need a careful consideration of the measurement technique. Furthermore, a near laser resonance in the target may lead to phase-shifts in the streaking signal. The streaking technique may be used to extract some features, like the phase shift around a Cooper minimum[17] and we give a recipe for extracting the relative phase of the ionisation matrix elements from the ground state and the resonant state when the laser. This will be discussed in chapter 6.

If the laser pulse used for the HHG process has several optical cycles, the outcome is not an isolated attosecond pulse but instead a series of attosecond pulses known as an attosecond pulse train (APT)[18]. Spectrally, the train is composed of either the odd harmonics from the fundamental laser frequency corresponding to two attosecond pulses per optical period or both the odd and the even harmonics corresponding to just one pulse per optical period. When electrons are released by the pulse train, they will come in narrow energybands corresponding to the spectral profile of the train. If the target is illuminated by both the pulse train of the odd harmonics and the fundamental field, then the electrons are allowed to exchange photons with the fundamental field and end up with an energy corresponding to an even harmonic. The probability for ending up at the even harmonics or sidebands depends very much on the relative phase or delay between the pulse train and the laser pulse[9, 19–22]. In chapter 7, we will discuss how the photoelectrons from a combination of an attosecond pulse train and the fundamental laser pulse may be used to perform time-resolved measurements and to characterise the pulse train.

Experiments with an XUV pulse that has a duration longer than the optical period of the laser field can also be used for time-resolved measurements, though the temporal resolution is determined by the dura-

tion of the pulse instead of the optical period. This leads to a temporal resolution on the few femtosecond timescale. This process, known as the laser-assisted photoelectric effect, has been used to measure e.g. the Auger lifetime of xenon core states, when the atoms are adsorbed on a platinum surface[23]. Some work on this setup is discussed in chapter 8.

Another approach to attosecond spectroscopy is to look for the absorption of the attosecond pulse as it passes the target, known as attosecond absorption spectroscopy. Again, the tool is the pump-probe experiment with two pulses and looking for the variation in the absorption signal as the relative delay between them is changed. Attosecond absorption spectroscopy has very recently been used to study the real-time motion of a valence hole in krypton atoms ionised with an intense few-cycle pulse[12] and to study time-resolved autoionisation in argon[13]. In chapter 9 we present a model to calculate the absorption signal and give an example of how two attosecond pulses can be used to study the hole formation in krypton with attosecond resolution.

While the process of high-order harmonic generation is not the subject of this thesis, we give a few remarks on how high-order harmonic spectroscopy can be used to probe the dynamics in atoms or molecules in chapter 10. As a spin-off from the considerations made in the absorption spectroscopy, we show that when calculating the high-order harmonic generation from a single atom or molecule, the signal is proportional to the norm-square of the dipole velocity.

Chapter

2 Attosecond Streaking

Photoelectron spectroscopy with a combined attosecond pulse and intense laser pulse is a powerful spectroscopic tool. The photoelectron is liberated by the attosecond pulse in a time-interval which is much shorter than the optical period of the assisting laser pulse. It is then accelerated by the laser pulse and the final energy of the electron holds a signature of the release-time. The acceleration of the electron, known as streaking, can be used both to characterise the pulses involved and for time-resolved measurements.

2.1 The Setup

Very briefly and from a theoreticians point of view, the setup for an attosecond streaking experiment consists of an oscillator providing phase-stabilised, few-cycle laser pulses with a central wavelength around 800 nm and an intensity of the order 10^{14} W/cm^2. This pulse is split into two, with the intense part ($\sim$ 90% of the intensity) providing the attosecond pulse through high-order harmonic generation (HHG) and the remaining part being sent through a delay line and onto the target. The polarisation of the two pulses is usually in the same direction and an energy-resolved photoelectron detector is placed in the polarisation direction from the target. The details of many of the different experiments

around the world can be found in Ref. [2] and references therein.

2.1.1 HHG for Attosecond Pulse Generation

High-order harmonic generation or HHG is often described with a very simple three-step model[24], where the process is split into *i*) ionisation of the target, *ii*) propagation of the electron wave packet in the continuum, and *iii*) recombination of the electron wave packet with the parent ion. The highest harmonics are emitted by electrons ionised just after the peak of the electric field and reach photon energies of up to $\omega_{\max} = 3.17U_p + I_p$, where I_p is the ionisation potential of the target atoms and $U_p = \mathcal{E}_0^2/4\omega_L^2$ is the ponderomotive potential, with $\mathcal{E}_0$ the amplitude of the laser field and ω_L the laser frequency. For laser pulses with several optical cycles, this results in a series of bursts temporally displaced by half the period of the fundamental field. When the laser pulse is very short, only one maximum of the field contributes significantly to this highly non-linear process and an isolated pulse with attosecond duration is produced. For typical experimental conditions the photon energies extend up to about 100 eV.

2.2 Streaking in the Strong-Field Approximation

The strong-field approximation gives a simple, quantum mechanical description of attosecond streaking. In the single-active-electron approximation, the Hamiltonian for the system is given as

$$H = H_0 + V_L(\vec{r}, t) + V_X(\vec{r}, t - t_0), \tag{2.1}$$

where H_0 is the field-free Hamiltonian describing the interaction of the electron with the ion, $V_L(\vec{r}, t) = \vec{r} \cdot \vec{\mathcal{E}}_L(t)$ is the interaction with the laser field and $V_X(\vec{r}, t - t_0) = \vec{r} \cdot \vec{\mathcal{E}}_X(t - t_0)$ is the interaction with the attosecond pulse. t_0 is the delay of the attosecond pulse, relative to the laser pulse (see Fig. 2.1). We calculate the photoelectron spectrum through the T-matrix formalism, where the ionisation probability from the initial state Ψ_i to a final state Ψ_f with asymptotic momentum $\vec{k}_f$ is

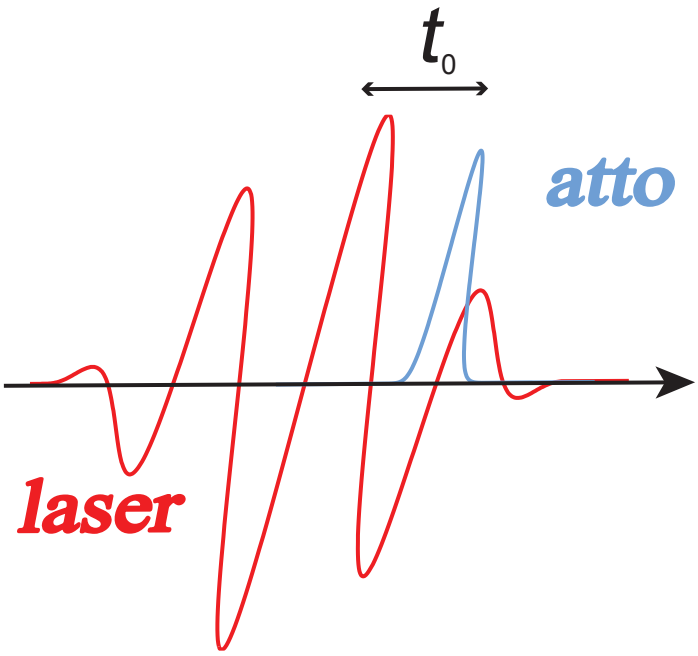

Figure 2.1 | In the streaking experiments a laser pulse and an attosecond pulse is sent onto the target with a variable delay, t_0.

given by

$$\frac{dP}{d\vec{k}_f}(t_0) = |T_{fi}(t_0)|^2 \tag{2.2}$$

and the transition matrix element is

$$T_{fi}(t_0) = -i \int dt \langle \Psi_f(t) | V_L(\vec{r}, t) + V_X(\vec{r}, t - t_0) | \Psi_i(t) \rangle. \tag{2.3}$$

In Eq. (2.3), the $V_L(\vec{r}, t)$ gives the ionisation due to the laser field and $V_X(\vec{r}, t - t_0)$ gives the ionisation due to the attosecond pulse. We are interested in the electrons released with a high kinetic energy, where the contribution from the attosecond pulse dominates and we therefore neglect the electrons released by the laser, known as above-threshold ionisation (ATI) electrons.

In the strong-field approximation we assume that the initial state is unaffected by the laser pulse and is an eigenstate of the field-free Hamiltonian

$$\Psi_i(\vec{r}, t) = \psi_i(\vec{r}) e^{-iE_i t}, \tag{2.4}$$

where $\psi_i(\vec{r})$ is the spatial wave function and E_i is the eigenenergy. We approximate the final state with the Volkov wave function, which is the solution to the Schrödinger equation when the ionic potential is neglected

$$\Psi_f(\vec{r},t) = \frac{1}{(2\pi)^{3/2}} \exp\left[i(\vec{k}_f + \vec{A}(t)) \cdot \vec{r} - \frac{i}{2}\int^t dt'(\vec{k}_f + \vec{A}(t'))^2\right], \tag{2.5}$$

where $\vec{A}(t)$ is the vector potential

$$\vec{A}(t) = -\int_{-\infty}^t dt'\vec{\mathcal{E}}(t'). \tag{2.6}$$

Since the laser field is much more intense than the attosecond pulse, we neglect it and assume that the only the laser field contributes to the final state wave function.

We may now calculate the transition matrix elements

$$\begin{aligned} T_{fi}(t_0) &\approx -i\int dt\langle\Psi_f(t)|V_X(\vec{r},t-t_0)|\Psi_i(t)\rangle && (2.7)\\ &= -i\int dt T^{1B}(\vec{k}_f + \vec{A}(t)) f_X(t-t_0) && (2.8)\\ &\quad \times \exp\left[\frac{i}{2}\int^t dt'(\vec{k}_f + \vec{A}(t'))^2 - iE_i t - i\omega_X(t-t_0)\right]. \end{aligned}$$

Here, we have introduced the first Born amplitude for the transition from the initial state to the final state, $T^{1B}(\vec{k}) = \langle\vec{k}|\vec{\mathcal{E}}_{x,0}\cdot\vec{r}|\psi_i\rangle$ and $\vec{\mathcal{E}}_X(t) = \vec{\mathcal{E}}_{x,0} f_X(t) e^{-i\omega_X t}$, with $\vec{\mathcal{E}}_{x,0}$ the peak electric field strength and polarisation, ω_X the central frequency, and $f_X(t)$ the envelope function. The key to the attosecond streaking is that the attosecond pulse should be much shorter than the optical period of the laser pulse, such that we may assume that the vector potential is constant over the duration of the attosecond pulse, $\vec{A}(t) \approx \vec{A}(t_0)$. Note that the integral in Eq. (2.8) only has support when the attosecond pulse is on, that is when $f_X(t-t_0)$ is non-vanishing. Looking at the Volkov phase, we can now approximate this in order to perform the integration analytically. Since the vector potential is almost constant over the attosecond pulse, we take the first-order Taylor expansion and find that

$$\int^t dt'(\vec{k}_f + \vec{A}(t'))^2 \approx \int^{t_0} dt'(\vec{k}_f + \vec{A}(t'))^2 + (\vec{k}_f + \vec{A}(t_0))^2(t-t_0), \tag{2.9}$$

where the first part on the right hand side is a constant (independent of t). With these approximations, the transition matrix element is given by

$$\begin{aligned} T_{fi}(t_0) &\approx -iT^{1B}(\vec{k}_f + \vec{A}(t_0))e^{i\Phi(t_0)} \\ &\times \int dt f_X(t-t_0)\exp\left[i(\frac{1}{2}(\vec{k}_f + \vec{A}(t_0))^2 - E_i - \omega_X)(t-t_0)\right]. \end{aligned} \tag{2.10}$$

We have introduced $\Phi(t_0) = \frac{1}{2}\int^{t_0} dt'(\vec{k}_f + \vec{A}(t'))^2 - E_i t_0$, which is an overall phase on the transition matrix element and has no influence on the measured photoelectron spectrum. The time integral is the Fourier transform of the envelope function and we find that

$$T_{fi}(t_0) \sim -iT^{1B}(\vec{k}_f + \vec{A}(t_0))e^{i\Phi(t_0)}\tilde{f}_X((\vec{k}_f+\vec{A}(t_0))^2/2 - E_i - \omega_X). \tag{2.11}$$

This is the recipe for calculating the streaking spectrum as a product of the momentum representation of the initial state and the spectral representation of the attosecond pulse. The Fourier transform of the envelope function is peaked around the origin and we find the that the electron energy distribution is peaked around

$$E = \frac{k_f^2}{2} = \omega_X + E_i - \vec{k}_f \cdot \vec{A}(t_0) - \frac{A(t_0)^2}{2}. \tag{2.12}$$

With the field strengths used experimentally, the last term is typically very small and can in many cases be neglected.

2.2.1 The Streaking Spectrum

The common way of plotting the spectra, is to look at the energy-resolved photoelectron spectrum in a particular direction. We note that

$$d\vec{k} = dkd\Omega = \frac{dEd\Omega}{k} \tag{2.13}$$

and find from Eq. (2.2) that the energy-resolved spectrum is given by

$$\frac{dP}{dEd\Omega}(t_0) = k_f|T_{fi}(t_0)|^2, \tag{2.14}$$

where E and Ω are the kinetic energy and the direction of the electron.

A typical streaking spectrum is plotted in Fig. 2.2. The laser has a sine-squared envelope for the vector potential

$$\vec{A}(t) = \vec{A}_0 \sin^2\left(\frac{\pi t}{\tau_L}\right)\cos(\omega_L t). \tag{2.15}$$

The wavelength is 800 nm and the peak intensity is 10^{12} W/cm^2. The duration is $\tau_L = 11$ fs corresponding to 4 optical cycles and the FWHM is $\frac{\tau_L}{2}$ for the sine-squared envelope. The attosecond pulse has a central frequency of 91 eV, a Gaussian envelope and a FWHM duration of 200 asec. The attosecond pulse is assumed to be in the perturbative region, but the amplitude in Fig. 2.2 is in arbitrary units and hence the strength of the attosecond pulse is not important. The binding energy is 13.6 eV corresponding to the hydrogen ground state and it is assumed that $T^{1B}(\vec{k}_f)$ is constant in the relevant energy region.

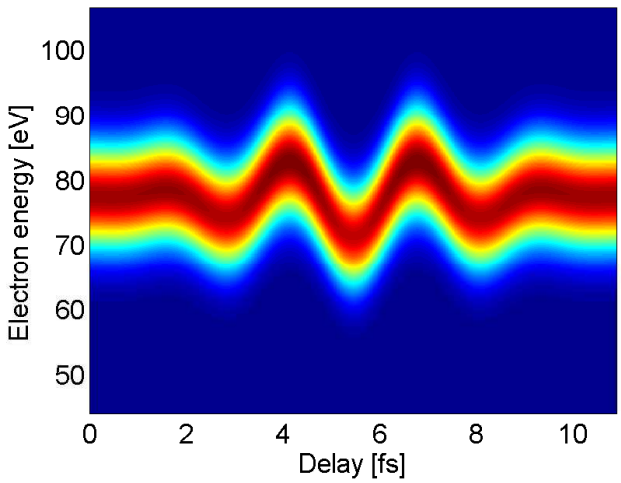

Figure 2.2 | A typical example of a streaking spectrum, that is $\frac{dP}{dEd\Omega}(t_0)$ for a set of pulse parameters given in the text.

In this example, we only look for electrons emitted along the common polarisation axis of the laser and attosecond pulse. In this direction, $\vec{k}_f$ and $\vec{A}$ are parallel and the oscillations in the streaking spectrum are maximal.

From the spectrum, one may calculate the centre of energy (CoE)

to more quantitatively see the oscillations. The CoE is defined as

$$E_{CoE}(t_0) = \frac{\int dE\ E\frac{dP}{dE}(t_0)}{\int dE\ \frac{dP}{dE}(t_0)} \tag{2.16}$$

and gives the average energy of the detected electrons. The CoE is plotted in Fig. 2.3.

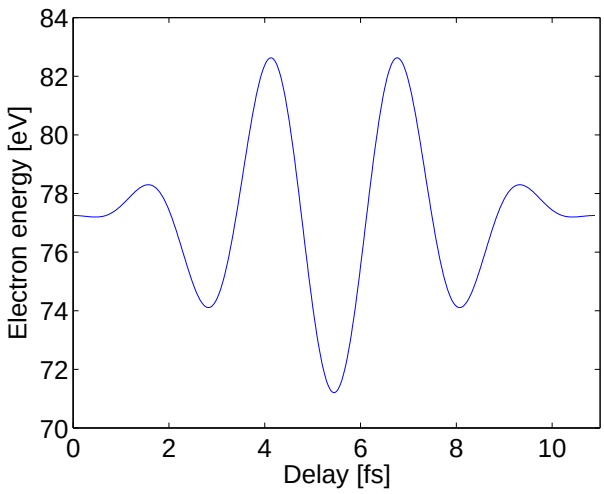

Figure 2.3 | The centre of energy as given by Eq. (2.16) calculated from the data presented in Fig. 2.2. The curve follows the oscillations in the mean energy of the electrons.

2.3 Time-Resolved Measurements

Attosecond streaking can be used to measure the emission time of electrons from two different channels, provided they are well separated in energy. If the electrons from the two channels do not overlap in the streaking spectrum, one measures a streaking spectrum for each of the two independently. If one of the channels is delayed relative to the other, the delayed electrons will not be accelerated in the laser field from time t_0, but instead from a later time $t_0 + \Delta t$, where Δt is the delay. This means that the streaking spectrum will oscillate as $\vec{k} \cdot \vec{A}(t_0)$ for the undelayed channel and $\vec{k} \cdot \vec{A}(t_0 + \Delta t)$ for the delayed channel. The principle is illustrated in Fig. 2.4. The temporal shift between the two curves is a measure of the relative delay between the emission channels.

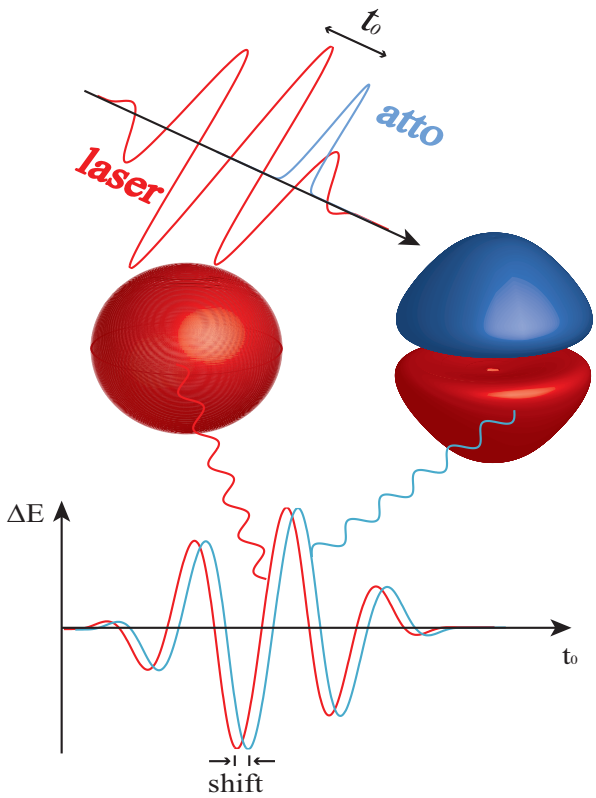

Figure 2.4 | Schematic presentation of the attosecond streaking experiment for time-resolved measurements. A laser pulse and an attosecond pulse with a variable time-delay, t_0, are focused onto a target. The kinetic energy of the photoelectrons depends on the delay between the two pulses, which gives a characteristic signal. If electrons are released from two different channels (sketched as the s-like and the p-like orbitals) and if release from one of the channels is delayed compared to the other, the signal is shifted as shown in the bottom of the figure.

This technique has been used to measure the emission-time of electrons from two different initial states in the metal tungsten[6]. The experiment shows a delay of 110 ± 70 asec between the conduction band electrons and electrons from a localised 4f core state. The interpretation in the paper is that this is a measurement of the travel time from ionisation and until the electrons reach the surface. Theoretical works have explained the results in various ways[25–28]. The interpretation of this experiment is the primary subject of chapters 3 and 4.

Another very recent experiment measured the difference in emission time for 2s and 2p electrons in neon[8]. This experiment will be discussed

in chapter 5, where we will also discuss some complications to the time-resolved measurements with the streaking technique and the fact that a shift in the streaking spectrum is not necessarily the result of a temporal delay.

2.4 Pulse Characterisation

As is seen from Eq. (2.12), the mean energy of the electrons follow the vector potential of the laser pulse. This is used in experiments to make direct measurements of the electromagnetic field[5, 29]. The oscillations in Figs. 2.2 and 2.3 are a direct mapping of the vector potential through the term $-\vec{k}_f \cdot \vec{A}(t_0)$ and the vector potential holds the full information about the laser pulse.

The transition matrix element in Eq. (2.11) is related to the Fourier transform of the attosecond pulse, such that the streaking spectrum can be used to characterise the attosecond pulse. In the analysis presented here, only the norm-square of Fourier transform is available, but a more elaborate analysis shows that the chirp (time-dependent variation of the frequency) of the attosecond pulse can also be extracted[30]. This is known as the attosecond streak camera. Measuring the chirp is important, since the HHG process responsible for creating the attosecond pulses introduces an attosecond chirp, such that the lower frequencies proceed the higher frequencies and the pulse is temporally longer than the Fourier limit due to the spectral width.

Yet another technique relies on the fact that the streaking spectrum in Eq. (2.8) is a gated Fourier transform of the attosecond pulse and effectively fits the attosecond pulse and the laser pulse parameters to the streaking spectrum. This is know as Frequency-resolved optical gating for complete reconstruction of attosecond bursts or FROG CRAB[31]. This is a very powerful tool to reconstruct full information about the attosecond pulse and the laser pulse. The downside is that the FROG CRAB algorithm works like a black box and it may be very difficult to interpret if the reconstruction does not work.

Chapter

3 Attosecond Streaking from Metal Surfaces

The first experiment showing the extension of attosecond spectroscopy to condensed matter was done in 2007[6]. In this attosecond streaking experiment, a 300 asec pulse centered around 91 eV is sent onto a tungsten surface. From the surface, conduction band electrons are emitted with an energy around 83 eV and electrons from localised 4f core states are emitted with an energy centred around 56 eV. The electrons are detected in the direction perpendicular to the surface. With a variable delay, an infrared laser pulse centred around 750 nm is being sent onto the surface, near Brewster's angle to avoid any penetration into the surface. The laser pulse streaks the electrons and the streaking signal from the 4f electrons is delayed by 110 $\pm$ 70 asec compared to the conduction band electrons. This chapter will discuss the interpretation of this result.

3.1 Delayed Electron Emission

If we assume that the laser field does not penetrate the metal surface at all, then an electron wave packet formed within the metal will travel to the surface without experiencing the streaking due to the laser pulse.

The streaking signal would then follow

$$\Delta E \approx -\int_{t_0+\Delta t}^{\infty} dt' \vec{k} \cdot \vec{\mathcal{E}}(t') = -\vec{k} \cdot \vec{A}(t_0 + \Delta t), \tag{3.1}$$

where t_0 is the time of arrival for the attosecond pulse and Δt is the time it takes the electron to travel to the metal surface after excitation.

The modelling presented in the experimental paper is based on a static model of the tungsten surface[6]. From the electronic band structure, the group velocity is calculated for electrons with an energy around 85 eV and 58 eV. The group velocity combined with an electronic mean free path of 4 Å leads to a travel time to the surface of 60 asec for the conduction band electrons, while the mean free path is 5 Å for the slower 4f electrons leading to a propagation time of 150 asec. The difference of 90 asec corresponds well to the measured difference.

Very similar results were found from a one-dimensional time-dependent treatment[27]. Again the assumption is that the laser field does not penetrate the surface or at least that the penetration is much shorter than the electronic mean free path. In the numerical treatment they found a difference of 85 asec. Another work based on numerical simulation of classical transport theory found a smaller delay of only 33 asec[28].

3.1.1 Reference States for Absolute Time Measurements

To make any kind of time-resolved measurement, we need a signal to start and a signal to stop our clock. In the monitoring of the dynamics of electrons these signals will usually be in the form of electrons emitted from different steps in the process under investigation. For example, in the case of laser-assisted Auger decay, the signal to start the clock will be the direct emission of the inner-shell electron and the signal to stop the clock will be the Auger electron [23, 32, 33]. In other measurements it might not be as obvious how to choose these signals.

In the experiment, electron emission from the conduction band of tungsten was used as start signal and emission from the lower-lying band of 4f-electrons was used for stopping the clock [6]. This gives a

measurement of the difference in travel time to the surface of electron wave packets formed in the conduction band and in the 4f-band. It does not, however, give us the absolute travel time for either of the two. In order to measure the absolute travel time, we propose the use of electronic reference states located outside the metal. Electrons emitted from these states will be born directly in the infrared field and present a natural time zero for travel time measurements.

We propose two different kinds of reference states for these absolute measurements. First, classical electrodynamics tells us that a charge outside a conducting surface sees an attractive potential. Quantum mechanically, this gives rise to a series of bound states located outside the surface [34]. For metals with a band gap around the continuum edge, these states can have fairly long lifetimes of several tens of femtoseconds for the ground state and much longer for higher-lying states [35, 36]. This should be sufficient time to make it possible to prepare the system in a state with a high population in these states.

Another and perhaps more easily realisable system is to adsorb a few atoms onto the metal surface. The atomic species should be chosen such that electrons emitted from a certain level in the adsorbed atoms do not coincide in energy with any of the electrons from the metal. Then the electrons emitted from this atomic state serve as a time zero signal (they are already at the surface) and if the amount of adsorbed atoms is sufficiently small then it should not alter the travel time for electrons emitted from the surface.

3.2 Conduction Band Modelling

The jellium or Sommerfeld free electron model is a very simple model for the conduction band at a metal surface[37]. The Hamiltonian describing the system is a step function in z-direction

$$H = \frac{p^2}{2} + \Theta(z)V_0, \tag{3.2}$$

where $\Theta(z)$ is the Heaviside step function, which is 1 for $z > 0$ and 0 elsewhere and V_0 is the size of the step. V_0 is the amount of energy needed to release an electron from the bottom of the conduction band,

given by the sum $V_0 = E_F + \phi$, where E_F is the Fermi energy, the energy of the weakest bound electron and ϕ is the work function, the energy needed to release the weakest bound electron into vacuum. An actual metal is of course a lot more complicated, but since all the nuclei are screened by the electrons, the jellium potential is a fair effective potential for the electrons. The electronic states are found by the Aufbau principle, filling all eigenstates with energy below E_F.

The Hamiltonian is separable in Cartesian coordinates, and the solution to the x and y part is seen to be the free electron wave function

$$\psi(x, y, z) = \psi_{||}(x, y)\psi_{\perp}(z) = \frac{1}{2\pi} e^{i\vec{k}_{||}\cdot\vec{r}_{||}} \psi_{\perp}(z), \tag{3.3}$$

where $\psi_{||}$ and $\psi_{\perp}$ are the wave functions parallel and perpendicular to the metal surface respectively. The problem of finding the full eigenstates has now been reduced to the one-dimensional problem of a step function. The energy of the eigenstate ψ is $E = E_{||} + E_{\perp} = \frac{k_{||}^2}{2} + E_z$.

To find the bound eigenstates of the jellium Hamiltonian, it is seen that the potential is constant for both $z < 0$ and $z > 0$. Looking at $E_z < V_0$, the functional form of the solution in the two regions is

$$Ae^{ik_z z} + Be^{-ik_z z} \qquad z < 0 \tag{3.4}$$

$$Ce^{-\gamma z} \qquad z > 0, \tag{3.5}$$

where the exponentially growing part in $z > 0$ has been discarded. Here $E_z = \frac{k_z^2}{2} = V_0 - \gamma^2/2$. What is left in order to find the stationary states is to match the two solutions in $z = 0$. Both the wave function and the first derivative of the wave function must be continuous. Enforcing both these requirements gives the solutions

$$\psi_{\perp}(z) = A\Big(e^{ik_z z} + \frac{k_z - i\gamma}{k_z + i\gamma} e^{-ik_z z}\Big)\Theta(-z) + A\frac{2k_z}{k_z + i\gamma} e^{-\gamma z}\Theta(z). \tag{3.6}$$

Normalisation is chosen as $A = \frac{1}{\sqrt{2\pi}}$, similar to the normalisation of the free electron states. With this choice of normalisation, the bound state wave functions satisfy that

$$\langle \psi_{k'}(z) | \psi_k(z) \rangle = \delta(k - k'), \tag{3.7}$$

and the three dimensional wave functions satisfy a similar relation with the three dimensional delta function. Along with the choice of normalisation comes a density of states, which in three dimensional k-space is $\rho(\vec{k})d^3k = \frac{V}{8\pi^3}d^3k$[37]. The density of states in energy-space is then given by

$$\rho(E)dE = \frac{3n}{2E_F}\sqrt{\frac{E}{E_F}}, \tag{3.8}$$

where n is the density of conduction band electrons (number per volume) and E_F is the Fermi energy, the energy of the highest occupied state.

The free electron model is quite good at describing the conduction band of simple metals, but not all metals are free electron like. Tungsten, which is the metal used in the streaking experiment[6], is unfortunately not very free electron like. The density of states within the conduction band, as calculated in Ref. [38] shows a lot of structure and does not follow the square root dependence predicted by free electron theory. The free electron model is however applied due to its simplicity.

When calculating photoemission spectra, it is necessary to include the finite mean free path within the metal. After an electron has been excited to an unbound state it will propagate, on average, only the mean free path before being scattered. The dominating part of this scattering is electron-electron scattering as will be discussed in the next chapter. The inelastic mean free path for electrons with a kinetic energy around 50-100 eV within the metal is of the order of only 5 Å[39]. The mean free path is shorter than the penetration depth of the XUV field, even at grazing incidence and comparable to the inter-atomic spacing. This implies that only the outermost electrons may be emitted directly. A simple way to incorporate this limited mean free path, λ, is to let the free electron wave function fall off exponentially within the metal, $\psi_f \to \psi_f e^{z/2\lambda} = \psi_f e^{\kappa z}$, where $\kappa = (2\lambda)^{-1}$ and the 2 ensures that the norm-square of the wave function is damped with the mean free path as damping parameter. Note that $z < 0$ within the metal. The spatial dependence of ψ_f is like a free electron with the momentum shifted by the vector potential (see Eq. (2.5))

$$\psi_{k_f}(\vec{r}) = \frac{1}{(2\pi)^{3/2}} e^{i(\vec{k}_f + \vec{A}(t))\cdot\vec{r}} \tag{3.9}$$

Calculating the first Born transition matrix element from the jellium initial state to the final state, we find

$$\begin{aligned} T^{1B}(\vec{k}_f + \vec{A}(t)) &= \mathcal{E}_{X,0}\frac{\delta(\vec{k}_{f,||} - \vec{k}_{i,||})}{\sqrt{2\pi}} \int dz \exp[-i(k_{f,z} + A(t) - i\kappa)z] z\psi_\perp(z) \\ &= \mathcal{E}_{X,0}\frac{\delta(\vec{k}_{f,||} - \vec{k}_{i,||})}{2\pi} \Bigg\{ \int_0^\infty dz\, z e^{-i(k_{f,z}+A(t)-i\gamma)z} \qquad (3.10) \\ &+ \int_{-\infty}^0 dz\, z \Big[e^{i(k_{i,z}-(k_{f,z}+A(t))-i\kappa)z} + \frac{k_{i,z} - i\gamma}{k_{i,z} + i\gamma} e^{-i(k_{i,z}+(k_{f,z}+A(t))+i\kappa)z} \Big] \Bigg\}. \end{aligned}$$

γ depends on the initial state momentum and the extension of the initial state into the vacuum region is greatest when γ is smallest, which is for electrons right at the Fermi energy. For the electrons at the Fermi energy, $\gamma = \sqrt{2V_0 - k_F^2} = \sqrt{2\phi}$, since $V_0 = \phi + E_F$ and $E_F = k_F^2/2$. This is still about ten times bigger than $\kappa = (2\lambda)^{-1}$. Disregarding the contribution from the positive z-axis, only the two terms from the negative z-axis need to be calculated. This may be done using partial integration, resulting in

$$\begin{aligned} T^{1B}(\vec{k}_f + \vec{A}(t)) &= \mathcal{E}_{x,0}\delta(\vec{k}_{f,||} - \vec{k}_{i,||}) \Big[\{\kappa - i(k_{f,z} + A(t) - k_{i,z})\}^{-2} \\ &+ \frac{k_{i,z} - i\gamma}{k_{i,z} + i\gamma} \{\kappa - i(k_{f,z} + A(t) + k_{i,z})\}^{-2} \Big] \qquad (3.11) \end{aligned}$$

This very simple result is the motivation for choosing the jellium model despite its flaws. Since we are trying to understand the origin of the time-delays, we cannot make the simplifying assumptions leading from Eq. (2.8) to Eq. (2.11), and instead have to solve the temporal integration numerically. In the final state, the free electron state is used in all space, instead of the unbound jellium state. In the limit where the energy of the free electron is large compared to the surface step, V_0, the solution is of course the free electron, but the energy range considered here is not that far above the surface potential. When the electron reaches the detector, it has passed the surface and the energy the electrons will have in the vacuum is given by $E_v = E - V_0$, where E_v is the electron energy in vacuum and E is the electron energy within the metal. Further, there is a finite probability that an electron excited

above the vacuum limit will be reflected from the metal surface or scatter off other electrons. This will be discussed below in chapter 4.

3.2.1 Time Delay in the Jellium Model

Very many electronic states are initially occupied in the metal. To find the distribution of electrons emitted from the surface, we need a summation over all of the initially occupied states and Eq. (2.14) is replaced with

$$\frac{dP}{dEd\Omega}(t_0) = 2k_f \int dE_i \rho(E_i) f^{FD}(E_i, T)|T_{fi}|^2, \tag{3.12}$$

where the integral runs over all initial states, $\rho(E_i)$ is the density of initial states and

$$f^{FD}(E, T) = \frac{1}{1 + \exp[(E - \mu)/k_B T]} \tag{3.13}$$

is the Fermi-Dirac distribution function and μ is the chemical potential, k_B is Boltzmann's constant and T is the temperature. For metals, the chemical potential below a few thousand kelvins is approximated by the Fermi energy. For tungsten, we use $E_F = 4.5$ eV and $\phi = 5.5$ eV and room temperature $T = 295$ K.

We have numerically integrated Eq. (2.11) with the first Born matrix elements from Eq. (3.11) to see if the streaking spectrum is shifted relative to the vector potential. The results are plotted in Fig. 3.1. The attosecond pulse is centered around $\omega_X = 91$ eV and the duration is 290 asec FWHM. The laser pulse is centred at 750 nm, with an intensity of 2×10^{12} W/cm^2 and a sine-squared envelope to make the integration in the Volkov phase analytical.

As is seen from the right panel of Fig. 3.1, the centre of energy of the emitted electrons follows the vector potential without showing any delay. In this calculation we assume that the laser field penetrates the surface with a penetration depth $\delta > \lambda$. The mean free path is of the order 5 Å[39], less than two atomic layers.

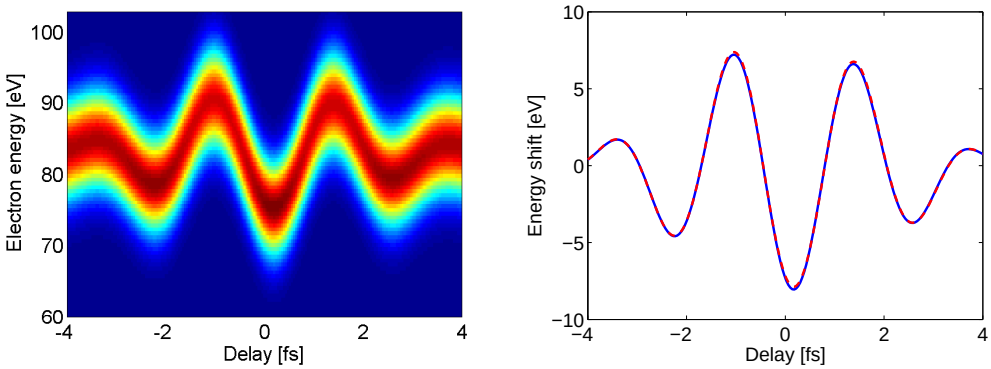

Figure 3.1 | The streaking spectrum calculated from the jellium model (left). In the right panel, the centre of energy (red curve) is plotted along with $-\vec{k}\cdot\vec{A}(t_0)$ (blue curve). The centre of energy follows almost perfectly the vector potential and no delay is seen for the jellium electrons.

3.3 Core Level Modelling

The inner electrons in the atoms do not feel the interaction with the neighbouring atoms, as much as the outer electrons. The electronic state of the outermost electrons in a metal are often completely independent of the atomic species and the simple jellium model, completely neglecting the atomic potential in favour of an average potential, may be used to model the conduction band. The inner electrons are much tighter bound to the nucleus, and it is better to use the atomic orbitals as a starting point. Here, we start from a bulk model of the metal, neglecting the surface. This approach was first employed in Ref. [26].

The potential within the metal has a translational symmetry determined by the lattice of the nuclei. The eigenfunctions of a potential with a discrete translational symmetry are known as Bloch waves, and assuming that the core electrons are tightly bound and hence in orbitals resembling the atomic states, the eigenstates are given as

$$\psi^k_{\text{loc}}(\vec{r}) = \frac{1}{\sqrt{N}}\sum_{\vec{R}} e^{i\vec{k}\cdot\vec{R}}\Phi(\vec{r}-\vec{R}), \tag{3.14}$$

where N is the total number of nuclei in the metal, the sum over $\vec{R}$ runs over all the locations of the nuclei, and $\Phi(\vec{r})$ is the atomic wave function. The energy of this wave function is the energy of the atomic state and

is independent of the lattice momentum, $\vec{k}$. The normalisation of ψ^k_{loc} is such that

$$\begin{aligned}\langle\psi^{k'}_{\text{loc}}|\psi^k_{\text{loc}}\rangle &= \frac{1}{N}\sum_{\vec{R},\vec{R}'} e^{i\vec{k}\cdot\vec{R}-i\vec{k}'\cdot\vec{R}'}\langle\Phi(\vec{r}-\vec{R}')|\Phi(\vec{r}-\vec{R})\rangle \\ &= \frac{1}{N}\sum_{\vec{R},\vec{R}'} e^{i\vec{k}\cdot\vec{R}-i\vec{k}'\cdot\vec{R}'}\delta_{\vec{R},\vec{R}'} = \frac{1}{N}\sum_{\vec{R}} e^{i(\vec{k}-\vec{k}')\cdot\vec{R}} = \sum_{\vec{G}}\delta(\vec{k}-\vec{k}'+\vec{G}).\end{aligned} \tag{3.15}$$

Here, it is assumed that the atomic state is sufficiently tightly bound that it does not overlap with the neighbouring orbitals and that it is normalised. The δ-function in the end is in the limit where the metal occupies all space and $N \to \infty$. The vector $\vec{G}$ is any reciprocal lattice vector, that is, any vector that satisfies that $\vec{R}\cdot\vec{G} = n\cdot 2\pi$ for any lattice vector, $\vec{R}$. The vector $\vec{k}$ is known as the crystal momentum. It is only conserved up to the reciprocal lattice vector introduced in Eq. (3.15).

Without presenting the detailed form of the atomic wave function, it is possible to calculate the first Born matrix element between the Bloch wave and the damped Volkov wave, ψ_{k_f}, at grazing incidence similar to what was done for the jellium conduction band in Sec. 3.2. Here $\vec{k}_f(t) = \vec{k}_f + \vec{A}(t)$ is introduced to make the notation a bit lighter,

$$\begin{aligned}T^{1B}(\vec{k}_f+\vec{A}(t)) =& \frac{\mathcal{E}_{X,0}}{\sqrt{NV}}\int d^3r e^{-i\vec{k}_f(t)\cdot\vec{r}} z e^{\kappa z}\sum_{\vec{R}} e^{i\vec{k}_i\cdot\vec{R}}\Phi(\vec{r}-\vec{R}) \\ =& \frac{\sqrt{v_{\text{cell}}}\mathcal{E}_{X,0}}{V}\sum_{\vec{R}} e^{i\vec{k}_i\cdot\vec{R}} i\frac{\partial}{\partial k_{f,z}}\int d^3r e^{-i\vec{k}_f(t)\cdot\vec{r}} e^{\kappa z}\Phi(\vec{r}-\vec{R}).\end{aligned} \tag{3.16}$$

Here, v_{cell} is the volume of the Wigner-Seitz cell containing one atom. Since the atomic levels are localized, the integration may be limited to just the Wigner-Seitz cell centered around the atom at $\vec{R}$ instead of the entire half-space. At the same time, if the radius of the Wigner-Seitz cell is small compared to the characteristic damping length, κ, the damping may be taken to be constant over the cell. This approximation allows us to evelaluate the space-integral in the first Born transition matrix

element

$$
\begin{aligned}
&\approx i\mathcal{E}_{X,0}\frac{\sqrt{v_{\text{cell}}}}{V}\sum_{\vec{R}} e^{i(\vec{k}_i-\vec{k}_f(t))\cdot\vec{R}}e^{\kappa R_z}\frac{\partial}{\partial k_{f,z}}\int_{\text{cell}} d^3r e^{-i\vec{k}_f(t)\cdot(\vec{r}-\vec{R})}\Phi(\vec{r}-\vec{R}) \\
&= i\mathcal{E}_{X,0}\frac{\sqrt{v_{\text{cell}}}}{V}\frac{\partial}{\partial k_{f,z}}\sum_{\vec{R}} e^{i(\vec{k}_i-\vec{k}_f(t))\cdot\vec{R}}e^{\kappa R_z}\tilde{\Phi}(\vec{k}_f(t)) \qquad (3.17) \\
&= i\mathcal{E}_{X,0}\frac{(2\pi)^2\sqrt{v_{cell}}}{V}\sum_{\vec{G}_{||}}\delta(\vec{k}_{i,||}-\vec{k}_{f,||}(t)+\vec{G}_{||}) \\
&\times\frac{\partial}{\partial k_{f,z}}\frac{\tilde{\Phi}(\vec{k}_f(t))}{1-\exp(i(k_{i,z}-k_{f,z}(t)+i\kappa)a)},
\end{aligned}
$$

where a is the lattice constant along the z direction and $\tilde{\Phi}$ is the Fourier transform of the atomic orbital.

To make a simple model of the atomic state, one may model them by an energy-scaled hydrogenic ground state, which is given by

$$
\tilde{\Phi}(\vec{k}) = \frac{(2I_p)^{5/4}}{\pi(k^2+2I_p)}, \qquad (3.18)
$$

where I_p is the ionisation potential.

3.3.1 Delay from the Bloch Waves of Core States

The denominator in Eq. (3.17) is very sensitive to the mean free path in units of the lattice constant, κa. If this product is small, the denominator and the first Born matrix element depend crucially on the value of the vector potential and we cannot ignore this dependence when calculating the streaking spectrum. As first pointed out in Ref. [26], this interference term between the electrons being emitted from different layers beneath the surface can lead to a delay in the streaking signal. For electrons with a kinetic energy around 50 eV, the inelastic mean free bath is around 5 Å[39] and the lattice constant for tungsten W(110) surface is 3.31 Å perpendicular to the surface.

We have numerically integrated Eq. (2.11) with the first Born matrix elements from Eq. (3.17) to see if the streaking spectrum is shifted relative to the vector potential. The results are plotted in Fig. 3.2. The

attosecond pulse is centred around $\omega_X = 91$ eV and the duration is 290 asec FWHM. The laser pulse is centred at 750 nm, with an intensity of 5×10^{10} W/cm^2 and a sine-squared envelope to make the integration in the Volkov phase analytical. In the same figure, the contribution from the conduction band is also plotted, as discussed in Sec. 3.2.1. The relative strength of the conduction band and the core level electrons is scaled to be of comparable magnitude.

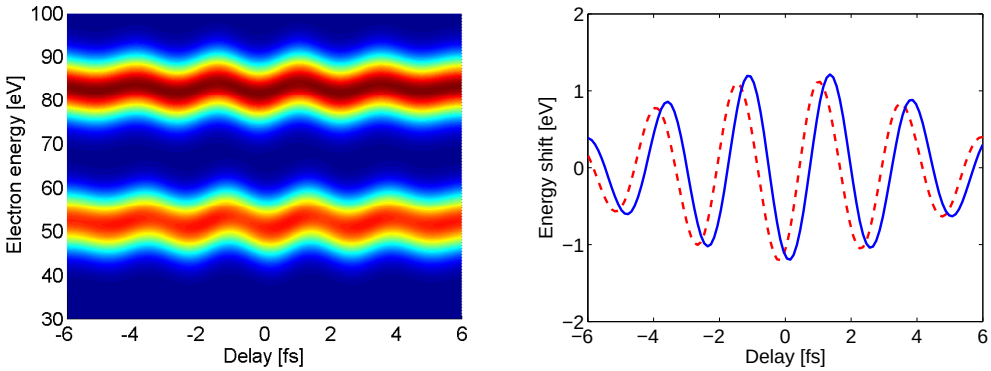

Figure 3.2 | The streaking spectrum calculated from the jellium model and the Bloch waves (left). In the right panel, the centre of energy for the conduction band electrons (red curve) is plotted with the centre of energy from the core electrons (blue curve). The centre of energy from the 4f electrons has been scaled by a factor 1.1 to ease the comparison.

While it may be difficult to see from the streaking spectrum directly, the center of energy analysis clearly shows that the signal from the core electrons is shifted relative to the conduction band signal. We find a shift of 300 asec, about twice as big as what was found in the experiment. This deviation can be remedied if the mean free path were only half as big[40].

The jellium model shows no time delay, but assumes that the electrons are completely free. An alternative reconciliation between the theory and the experiment might be that there is some localised nature to the conduction band electrons, which might be suggested by band structure calculations[38]. If the jellium model does not give a good description, then the conduction band electrons might also be delayed.

3.4 Conclusions on the Time Delay

Several theoretical models have been able to explain the temporal delay measured in the experiment[6], using very different assumptions and leading to different interpretations of the delay[6, 26–28, 41]. The problem is that there is only one data point, namely the 110 ± 70 asec delay measured for tungsten! As long as only this single experimental point exists, it will be impossible to tell which interpretation of the experiment is the correct one. All of the theories presented have their weaknesses; the jellium model does not allow any strucure in the conduction band and the Bloch waves are a good basis for the bulk tungsten, though not neccesarily for the states very close to the surface as is the case here. Similarly, the static theory presented with the experiment[6] is based on bulk properties of the metal, while the numerical solution[27] is actually a calculation for a copper Cu(111) surface and assumes that the laser field does not penetrate the surface.

Hopes are that more data is coming. The group behind the experiment[6] has presented some preliminary data on rhenium covered with a monolayer of xenon. The xenon plays the same role as the image charge states or adsorbates discussed in Sec. 3.1.1, to allow an absolute measurement of the electronic travel time. This and more experimental data will be a valuable guide for further progress in the understanding of streaking experiments from condensed matter surfaces.

Chapter

4 Secondary Electrons

In the attosecond experiment[6], there is a tail of lower energy electrons, not present in the calculated spectra. We develop two different theories to describe the tail of low energy electrons following excitation of a metal surface. One looks at direct electrons and electrons released after exactly one scattering and another is based on secondary electron cascades. Both theories use a semi-classical approach treating the electrons as localised particles propagating within the medium. The amount of electrons released into the vacuum region is then determined by multiplication with the probability of the electron being transmitted through the surface.

The theory is based on a three step model, factoring the photoelectron emission process as *i*) electron excitation to an unbound state within the metal, *ii*) electron propagation to the surface and *iii*) escape through the surface.

4.1 Single-Scattering Theory

First, we develop a theory describing the direct propagation to the surface and propagation with exactly one scattering, based on the work of Berglund and Spicer[42]. We consider how an electron excited to an energy, E, may scatter from another electron still bound in the Fermi sea,

share its energy with the Fermi band electron and in this way produce two excited electrons with energies E' and $E - E'$, both of which may escape the metal surface.

We assume that electron propagation within the metal is described by only the inelastic mean free path and that this is much shorter than the penetration depth of the exciting pulse. In that case, the amount of electrons per volume $P(E)$ formed with energy E, is independent of the distance to the surface. The probability for an electron to propagate to the surface without scattering, from a depth $|z|$ within the metal and at an angle θ to the surface normal, is given by (see Fig. 4.1)

$$p^0_{\text{prop}}(E, z, \theta) = \exp\Big(- \frac{|z|}{\lambda(E)\cos\theta}\Big), \tag{4.1}$$

where $\lambda(E)$ is the inelastic mean free path of an electron with energy E.

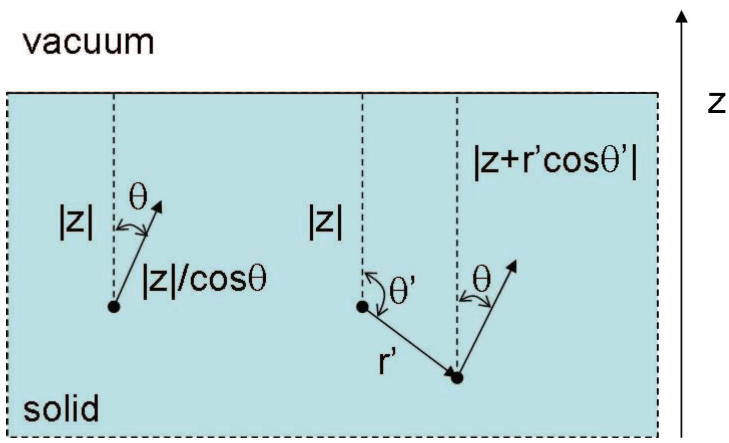

Figure 4.1 | Illustration of emission of a direct(left) and a scattered(right) electron, initially created at a distance $|z|$ from the metal surface ($z = 0$).

Integrating Eq. (4.1) over all depths, z, within the metal yields the total amount of direct electrons emitted at a given angle θ relative to the surface normal as

$$N_0(E, \theta) = \int dz\, p^0_{\text{prop}}(E, z, \theta) P(E) = \lambda(E) P(E) \cos\theta. \tag{4.2}$$

Most often the direction of interest is along the surface normal, in which case $\cos\theta = 1$. For the scattered electrons, we therefore regard only the electrons ending up along the surface normal.

The amount of electrons reaching the surface along the surface normal after one scattering is given by

$$N_1(E) = \int dz \int dE' p^1_{\text{prop}}(E, E', z) P(E'), \tag{4.3}$$

where $p^1_{\text{prop}}(E, E', z)$, the probability of propagating to the surface from the depth $|z|$ suffering one scattering from the energy E' to the energy E, may be factored as

$$p^1_{\text{prop}}(E, E', z) = \int \frac{d^3r'}{4\pi\lambda(E')} \exp\Big(-\frac{r'}{\lambda(E')}\Big) S(E, E') p^0_{\text{prop}}(z + r'\cos\theta', E). \tag{4.4}$$

The first term, $\frac{d^3r'}{4\pi\lambda(E')} \exp\Big(-\frac{r'}{\lambda(E')}\Big)$, is the probability of suffering a scattering between r' and $r' + dr'$. The second term, $S(E, E')$, is the probability density for scattering from the energy E' to the energy E given that a scattering does occur and is assumed to be independent of the angles involved. The third term is the probability that the electron will propagate to the surface without further scatterings, as given by Eq. (4.1). See the right hand side of Fig. 4.1. The integration is over all directions and distances that the electron may travel before suffering the scattering.

Inserting Eq. (4.4) into Eq. (4.3) gives

$$\begin{aligned} N_1(E) = &\int_E^\infty dE' P(E') S(E, E') \\ &\times \int dz \int \frac{d^3r'}{4\pi\lambda(E')} \exp\Big(-\frac{r'}{\lambda(E')}\Big) \exp\Big(-\frac{|z + r'\cos\theta'|}{\lambda(E)}\Big). \end{aligned} \tag{4.5}$$

It is assumed that the mean free path is independent of the energy, $\lambda(E') = \lambda(E) = \lambda$, since the universal curve is reasonable flat in the area $20 - 200$ eV[39].

The integration over $\vec{r}'$ is bounded by the fact that the scattering must take place within the metal. This integration may be done analytically by splitting the integral into two, depending on whether the initial direction of the electron is towards, $\cos\theta' > 0$, or away from the

surface, $\cos\theta' < 0$. For $\cos\theta' < 0$, there is no restriction on r'

$$\int \frac{dr'}{4\pi\lambda} \int_{\pi/2}^{\pi} d\theta' 2\pi \sin\theta' \exp\Big(-\frac{r'}{\lambda}(1-\cos\theta')\Big)$$
$$= \frac{1}{2}\int_{\pi/2}^{\pi} d\theta' \sin\theta' \frac{1}{1-\cos\theta'} = \log 2/2. \tag{4.6}$$

For the part where $\cos\theta' > 0$, the r'-integration is restricted to $r'\cos\theta' < -z$, so that the scattering takes place within the metal. This gives

$$\int_0^{\frac{-z}{\lambda\cos\theta'}} \frac{dr'}{4\pi\lambda} \int_{\pi/2}^{\pi} d\theta' 2\pi \sin\theta' \exp\Big(-\frac{r'}{\lambda}(1-\cos\theta')\Big) \tag{4.7}$$
$$= \frac{1}{2}\int_{\pi/2}^{\pi} d\theta' \sin\theta' \frac{1-\exp[-\frac{z}{\lambda}(1-\sec\theta')]}{1-\cos\theta'} = \frac{1}{2}\int_0^1 d\xi \frac{1-\exp[\frac{z\xi}{\lambda(1-\xi)}]}{\xi},$$

where $\xi = 1-\cos\theta'$. Now, the z-integral of Eq. (4.3) may be performed

$$\int_{-\infty}^{0} dz \left[\frac{\log 2}{2} + \frac{1}{2}\int_0^1 d\xi \frac{1-\exp[\frac{z\xi}{\lambda(1-\xi)}]}{\xi}\right] e^{z/\lambda} \tag{4.8}$$
$$= \frac{\lambda\log 2}{2} + \frac{1}{2}\int_0^1 d\xi \frac{\lambda - \lambda\Big(1+\frac{\xi}{1-\xi}\Big)^{-1}}{\xi}$$
$$= \frac{\lambda\log 2}{2} + \frac{\lambda}{2}\int_0^1 d\xi \frac{1-(1-\xi)}{\xi} = \lambda\frac{1+\log 2}{2} \tag{4.9}$$

Using this result, we find that the total amount of electrons arriving at the surface along the surface normal, unscattered or after one scattering event is given as

$$N(E) = N_0(E) + N_1(E)$$
$$= \lambda P(E) + \lambda\frac{1+\log 2}{2}\int_E^{\infty} dE' P(E') S(E,E'). \tag{4.10}$$

The only thing left is to find an expression for the scattering probability, S. If it is assumed that the scattering probability is independent of the energies involved, the simplest possible form is to say that the

probability for scattering from the energy E' to an energy in the interval $[E, E + dE]$ is given by

$$S^0(E, E')dE = \frac{2dE}{E'}, \tag{4.11}$$

which is to say that all scatterings are equally probable. The factor of 2 is to account for the fact that after each scattering two electrons are present. This model may be improved a bit by including the density of states available for the scattering in a free electron model. In the limit where the energies involved are all much greater than the Fermi energy of the metal, E_F, we can neglect the initial energy of the assisting particle. The probability that an electron with energy E' is scattered to the interval $[E, E + dE]$ is then given by

$$S(E, E')dE = \frac{2\rho(E)\rho(E' - E)dE}{\int dE''\rho(E'')\rho(E' - E'')}. \tag{4.12}$$

The free electron density of states is given by $\rho(E) = \frac{3n}{2E_F}\sqrt{\frac{E}{E_F}}$, where n is the number of conduction band electrons per unit volume. With this approximation the scattering probability becomes

$$S(E, E')dE = \frac{2\sqrt{E}\sqrt{E' - E}dE}{\int dE''\sqrt{E''}\sqrt{E' - E''}}. \tag{4.13}$$

Examples of the electron tails following a Gaussian distribution of primary electrons, with the two scattering probabilities given by Eqs. (4.11) and (4.13) are shown in Fig. 4.2

Neither of these expressions fulfil the Pauli exclusion principle, which states that no scattering can take place that will leave a scattered electron with an energy below the Fermi energy, as these states are already occupied. This, however, only changes the shape of the energy distribution of the secondary electrons in the region close to the direct peak and the region close to the Fermi energy.

In the energy region that is of interest, it turns out that a single scattering is insufficient. Often, more than one scattering is involved, even when the electron is scattered to energies above 30 eV. A theory involving cascades of secondary electrons is therefore made to account for the multiple scatterings. The present theory seems adequate only very close to the direct peak.

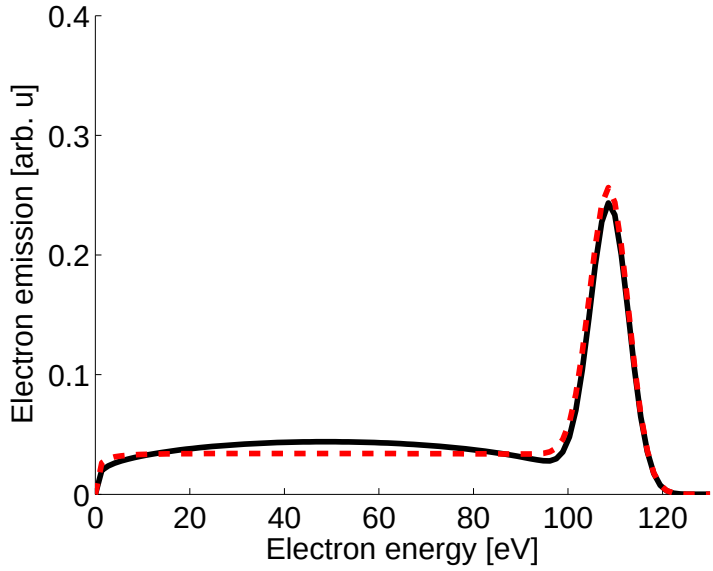

Figure 4.2 | Example of the tail resulting from including a single scattering. The red, dashed curve is obtained using Eq. (4.11) and the black curve is obtained using Eq. (4.13).

4.2 Cascade Theory

Originally, the cascade theory was developed to describe secondary electrons from electron bombardment experiments[43]; a beam of electrons with energy E_0 is directed onto a metal surface along the surface normal. The electrons emitted from the surface are a result of collisions within the metal. Each primary electron has the possibility of colliding inelastically with a conduction band electron, exciting it to an unbound state. Each of the unbound electrons has the possibility of knocking another electron free and a cascade of electrons is formed. A very similar process may take place in a photoelectron experiment, using high-energy photons. An electron initially excited by the photon may collide with a number of conduction band electrons before leaving the metal and hence a similar cascade of secondary electrons is formed. In this work, the interest is in the electrons emitted by an attosecond pulse with energies in the extreme ultraviolet(XUV), around $\omega_X = 100$ eV.

The starting point is Boltzmann's transport equation, describing the

evolution of the free electrons within the metal

$$\frac{\partial \Phi}{\partial t} + \vec{v} \cdot \nabla \Phi = -\frac{v\Phi}{\lambda} + J + \int dE' \int d\Omega' \frac{v'\Phi'}{\lambda'} S, \tag{4.14}$$

where $\Phi = \Phi(\vec{r}, \vec{\Omega}, E, t)$ is the number of electrons per volume, per energy and per angle, v is the speed of an electron with energy E, J is the source term (the amount of electrons created per volume, energy and angle) and S is the scattering probability from energy E' and direction Ω' to E and Ω. From here on, a number of approximations are made. First, it is assumed that the electron distribution has azimuthal symmetry. Second, since the penetration depth of the XUV pulse is several nanometers even at grazing incidence and the inelastic mean free path given by the universal curve is $\lambda \approx 5$ Å[39], it is assumed that the distribution is independent of the distance to the surface. Finally, it is assumed that the electron-electron scattering is determined by the short range, screened Coulomb interaction. In this case, the electron-electron scattering is nearly isotropic[43]. The Boltzmann equation then reduces to

$$\frac{v\Phi(E,t)}{\lambda(E)} = J(E,t) + \int dE' \frac{v'\Phi(E',t)}{\lambda(E')} S(E',E) - \frac{\partial \Phi(E,t)}{\partial t}. \tag{4.15}$$

The energy E is the free electron energy within the metal, with $E = 0$ at the bottom of the conduction band.

The source term, J, is only present for a finite time corresponding to the duration of the exciting pulse, which makes it attractive to perform a temporal integration and regard the total amount of electrons arriving at the surface. Recognising that $v\Phi(E,t)$ is the instantaneous current density through any area parallel to the surface, we find that the amount of electrons arriving at the surface, $N(E)$ satisfies

$$\begin{aligned} \frac{N(E)}{\lambda(E)} &= \int dt J(E,t) + \int dE' \frac{S(E,E')}{\lambda(E')} \int dt\, v'\Phi(E',t) + \int dt \frac{\partial \Phi(E,t)}{\partial t} \\ &= P(E) + \int dE' \frac{N(E')}{\lambda(E')} S(E,E'), \end{aligned} \tag{4.16}$$

where the last $P(E)$ is the time integral of the source term (the total amount of electrons created at energy E per volume) and the last term

vanishes since there are no free electrons in the limits long before or after the pulse.

What remains is to find an expression for the scattering term. The simplest possible scattering term is that which is independent of the angle and the final energy, E. This leads to (compare to Eq. (4.11))

$$S(E, E') = \frac{2}{E'}, \tag{4.17}$$

where the factor of 2 ensures that the normalisation is such that exactly 2 electrons are present after each collision. This expression does not fulfil the Pauli exclusion principle, since it allows scattering to electronic states below the Fermi level, which are already occupied. This leads to a correction for the scattering term when the energy E is only a few times the Fermi energy, which is below the range that we are interested in (for details, see [43]). One can quite easily give better expressions for this scattering term, but none of these allow for a simple, analytical computation of the distribution of the secondary electrons.

The solution to Eq. (4.16) is given by

$$N(E) = -\lambda(E) \int_E^\infty dE' \Big(\frac{E'}{E}\Big)^2 \frac{dP(E')}{dE'} \tag{4.18}$$

which is seen by substitution. $N(E)$ may now be put into a simple form in terms of the source term $P(E)$ by performing integration by parts on Eq. (4.18). This gives the final result for the cascade of electrons inside the metal arriving at the surface

$$N(E) = \lambda(E)P(E) + 2\lambda(E) \int_E^\infty dE' \frac{E'}{E^2} P(E'). \tag{4.19}$$

Eq. (4.19) is easily interpreted. The first term is the direct part, the amount of electrons created inside the metal that escape to the surface without ever being scattered. The second term represents all the scattered electrons. An electron created with an energy E' gives rise to a cascade of lower energy electrons, determined by the cascade factor $\frac{2E'}{E^2}$. In the approximations introduced above, energy distribution as well as the total number of emitted electrons come out as a convolution of the initial spectrum of the formed electrons with a cascade factor. Now the

only thing missing is the probability for an electron reaching the surface to actually overcome the surface barrier and escape into the vacuum.

From this theory we have calculated the electron spectrum. A Gaussian pulse of direct electrons gives rise to a tail of lower energy electrons as shown in Fig. 4.3.

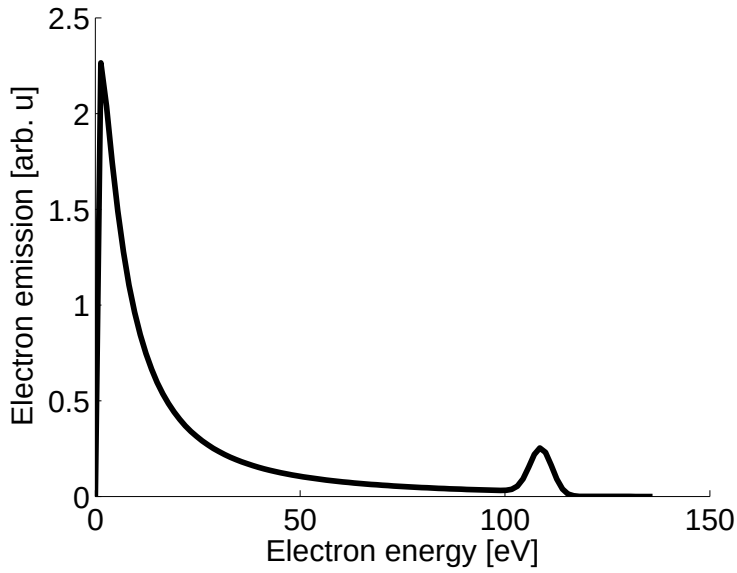

Figure 4.3 | The spectrum of emitted electrons following a Gaussian excitation of 110 eV electrons. The direct electrons are seen as the peak to the right, the rest of the contribution is from the cascade of secondary electrons. This has been multiplied with the transmission probability derived below.

With the assumption that the electron distribution is isotropic within the metal, not only the total amount of electrons passing through a small area of the surface should have this distribution, but also the distribution in each direction on its own. In this way, within the isotropic approximation, the distribution of the electrons reaching the metal surface along the surface normal, should be the same. This expression is therefore used to model the distribution along the surface normal.

4.2.1 Probability for Escaping Through the Surface

The final step missing for describing surface emission is the probability that an electron incident on the surface will escape through the surface. Looking only at the component along the surface normal, a

one-dimensional jellium model gives an expression for the transmission probability[44]. The potential is given by the step potential, as in Sec. 3.2

$$V(z) = V_0\Theta(z), \tag{4.20}$$

where $\Theta(z)$ is the Heaviside step function and $V_0 = \phi + E_F$ is the sum of the work function and the Fermi energy. For electrons coming from within the metal with an energy $E > V_0$, the solution takes the form

$$\psi(z) = \Theta(-z)\Big[e^{ikz} - A_R e^{-ikz}\Big] + \Theta(z)A_T e^{iqz}, \tag{4.21}$$

with A_R and A_T the amplitude for reflection and transmission respectively and $k = \sqrt{2E}$, $q = \sqrt{2(E - V_0)}$. Calculating the current density

$$j = \frac{1}{2i}\Big[\psi^* \frac{d\psi}{dz} - \frac{d\psi^*}{dz}\psi\Big], \tag{4.22}$$

for both $z < 0$ and $z > 0$ and setting them equal since the number of electrons is conserved gives

$$j = k(1 - |A_R|^2) = q|A_T|^2 \Rightarrow |A_R|^2 + \frac{q}{k}|A_T|^2 = 1. \tag{4.23}$$

Enforcing continuity of both wave function and first derivative gives the transmission probability

$$T = \frac{q}{k}|A_T|^2 = \frac{4qk}{(q+k)^2} = \frac{4\sqrt{1 - \frac{V_0}{E}}}{\Big(1 + \sqrt{1 - \frac{V_0}{E}}\Big)^2}. \tag{4.24}$$

The transmission probability for $V_0 = 10$ eV is plotted in Fig. 4.4.

In the limit $E \to V_0$ the transmission probability vanishes as the energy approaches the limit where the electron is bound. In the opposite limit, $E \to \infty$, the transmission probability rapidly approaches unity for $E > 2V_0$.

Another expression is used for the angular integrated scattering with $T(E) = 1 - \sqrt{\frac{\phi + E_F}{E}}$, corresponding to the amount of electrons carrying a sufficiently great momentum orthogonal to the surface to overcome the barrier and escape from the metal. This expression gives a much

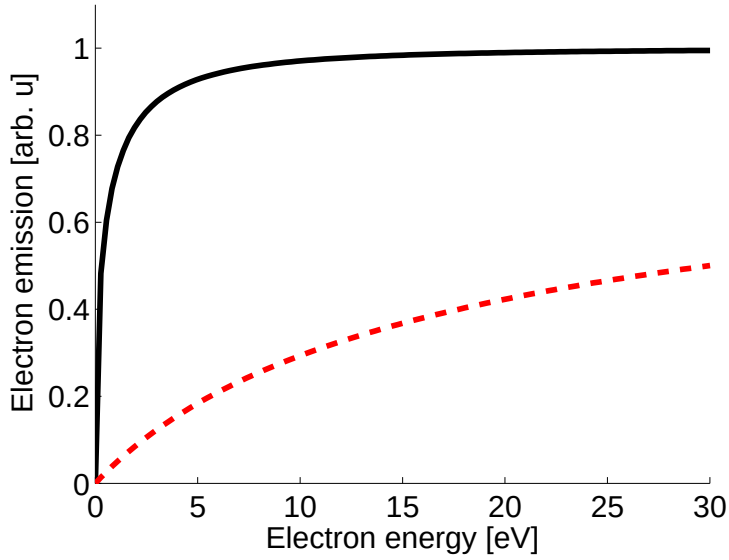

Figure 4.4 | The transmission probability for $\phi + E_F = 10$ eV. The energy scale is relative to the vacuum limit. The transmission probability is for the normal component (black, full) and for the angular integrated emission (red, dashed).

lower amount of emitted electrons and especially shifts the electrons to higher energies.

The total amount of electrons reaching the vacuum may now be found as the product of the amount reaching the surface and the probability of being transmitted through the surface, $N(E)T(E)$.

4.2.2 Application to the Tungsten Experiment

We apply our theory to tungsten and take experimental parameters from Ref. [6]: We use a Gaussian envelope for the attosecond pulse with an intensity-FWHM of 300 asec and a central frequency 91 eV. The modelling of the initial states is discussed in Secs. 3.2 and 3.3. We use an experimental Fermi energy of 4.5 eV for the conduction band, a hydrogenic localized 1s-state with a binding energy of 32.5 eV for the core states and a tungsten work function of 5.5 eV.

In Fig. 4.5 we consider the spectra without an assisting laser field in order to clearly display typical spectra of (a) direct electrons and (b) secondary electrons that have undergone scattering. Figure 4.5(a)

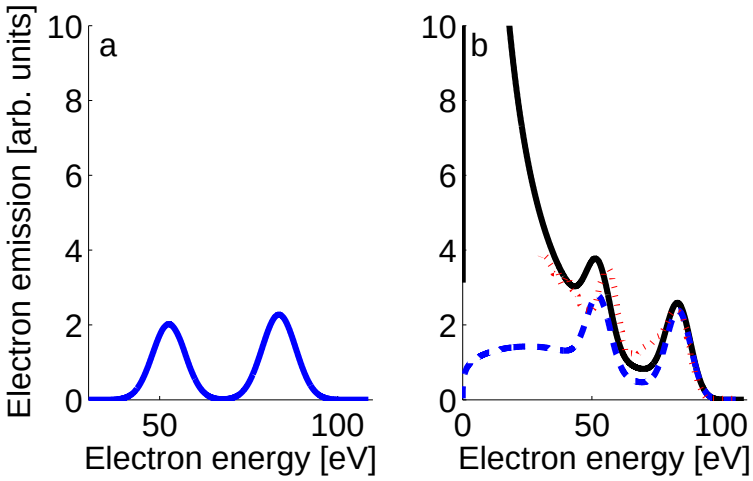

Figure 4.5 | Calculation of the photoelectron spectrum for a 300 attosecond pulse, including (a) only the direct electrons and including (b) both direct and scattered electrons. The full, black curve is with the cascade of secondary electrons while the dashed, blue curve includes only one scattering. The contribution from the conduction band has been scaled to be comparable to the contribution from the core band. The dotted curve in (b) shows data from Ref. [6].

shows that direct emission leads to two peaks, representing electrons released from the deeper-lying localized states and from the conduction band. When the electron-electron scattering is included, the two peaks both have a tail of lower energy electrons. This situation is shown in Fig. 4.5(b), where we also show the experimental results without a laser field[6]. We see that the inclusion of a cascade of electron scatterings explains the background in the spectrum. In the figure, we also plot the electron distribution including direct electrons and electrons that have scattered exactly once, as described in Sec. 4.1. This reproduces the amount of secondaries with energies near the direct peak, but fails to account for the many low-energy electrons that are released, supporting that multiple scatterings and a cascade is at play. Note that the experimental data have been subtracted for electrons stemming from above threshold ionisation (ATI) [6], and hence these do not contribute to the background.

Due to space-charge effects not included in our model, the experimental peaks are expected to be upshifted by approximately 3 eV[6]. While this shift is seen for the core-level electrons in Fig. 4.5(b), the

experimental and theoretical peaks pertaining to the conduction band electrons coincide. This accidental agreement is associated with a shortcoming of the free electron model which captures the qualitative features but does not quantitatively describe the tungsten conduction band, which holds a lot of structure[38]. Consequently, the centre of the peak comes out of our calculation a few eV too high, since many of the conduction band electrons are actually a few eV deeper bound[38].

We now turn to the streaking spectra. We follow[26], and invoke the streaking directly in the source term by adding the appropriate Volkov phase to the final free-electron states. For the laser pulse we use a sine-squared envelope, a duration of 13 fs, a wavelength of 750 nm, and an intensity of 5×10^{10} W/cm^2. Comparing Figs. 4.6(a) and (b) shows the effect of including electron-electron scattering as the primary photoelectron produced by the attosecond pulse propagates to the surface and produces a cascade of secondary electrons. We see that the structure and magnitude of the background matches quite well that seen in the experiment after ATI electrons has been subtracted (Fig. 2(b) in [6]).

Figs. 4.6(c) and (d) show the corresponding centre of energy (CoE) spectra. The CoE analysis is performed on the interval 44 eV - 63 eV (4f-electrons) and above 66 eV (conduction band electrons). The 4f-electron curve is, however, on top of the conduction band electron tail and is damped more than the conduction band curve. As in Refs. [6, 26], the 4f curve is multiplied by a factor (in our case 1.8) to make the 4f and conduction band amplitudes comparable. We see from a comparison of Figs. 4.6(c) and (d) that the inclusion of the background produced by secondary electrons leads to a reduction of the amplitude in the CoE spectrum and a very good agreement with the measured spectrum[6]. We note that the amplitude in the CoE data can be reproduced with the present T-matrix theory not including the background, but for an unrealistic low intensity of the femtosecond laser pulse. In this respect it is essential to have access to data as in Fig. 4.6(b).

With the inclusion of electron scattering within the metal, we are able to reconstruct the significant tail of electrons at lower energies observed experimentally in attosecond photoelectron spectroscopy from metals[6]. In monochromatic experiments there are generally relatively few electrons scattered to lower energies, as compared to what is seen in the attosecond regime. This is due to the fact that the amount of elec-

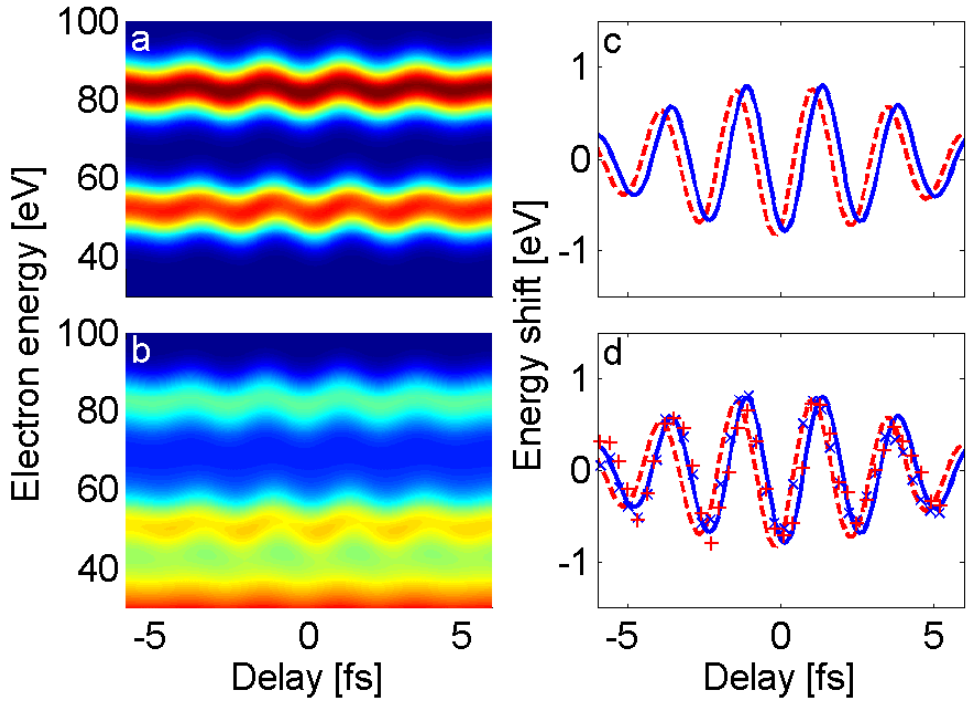

Figure 4.6 | Results for tungsten, with a laser intensity 5×10^{10} W/cm^2. (a) Direct emission spectra with scaled contribution from the conduction band. (b) Emission spectra including scattering to lower energies. (c) Centre-of-energy analysis showing the temporal delay of the 4f-electrons (full, blue) relative to the conduction band electrons (dashed, red) for only the direct electrons. (d) The same as (c) but including scattering. Also shown are experimental data from [6]; blue crosses: 4f electrons; red plusses: conduction band electrons. The energies of the 4f-electrons has been multiplied by 1.1 in (c) and by 1.8 in (d). See text for laser parameters.

trons scattered is proportional to the total amount of excited electrons. In an experiment with a spectrally broad pulse, the tail of electrons becomes comparable to the main peak of direct electrons.

In the modelling presented here, we have developed an analytical theory describing the secondary electrons released due to electron-electron collisions in the surface. The streaking is accounted for through the T-matrix elements and the acceleration of the electrons due to the laser field is included only there. In another simultaneous work[28], a numerical simulation of the classical transport equations showed how the propagation of the electrons in both the laser field and with collisions could lead to a streaking signal and secondary electrons. In that work, they found a delay of the order 40 asec between the conduction band

and core electrons, showing that classical transport theory may be a route to capture some of the many-electron aspects of the metal surface experiments.

Chapter

5 Time Delay in Streaking Spectra from Atoms and Molecules

While a delay in the streaking spectrum from a metal surface may be interpreted as a difference in the time it takes the electrons to escape, the origin of a delay in the spectrum from two different ionisation channels in an atom or molecule is less clear. Nevertheless, the streaking spectrum recorded from neon atoms shows that the signal from the 2p electrons is delayed with 21 ± 5 asec relative to the 2s electrons[8]. The origin of this delay is still not theoretically understood, but the Coulomb potential from the residual ion, the structure of the continuum and many-electron effects are all suggested to be part of the explanation. First, we will show that the streaking signal from an oriented polar molecule is shifted due to the Stark effect. This shift has no interpretation as a true temporal delay, which shows that not all shifts in the streaking signal originate from time-delays.

5.1 Streaking from Polar Molecules

In Sec. 2.2 we showed how to model the streaking experiment in the strong-field approximation and saw that the kinetic energy of the photoelectrons oscillates when the relative delay between the attosecond pulse and the laser pulse is varied. The mean kinetic energy of the

released electrons is (Eq. (2.12))

$$E = \frac{k_f^2}{2} = \omega_X + E_i - \vec{k}_f \cdot \vec{A}(t_0) - \frac{A(t_0)^2}{2}. \tag{5.1}$$

It is now experimentally possible to orient polar molecules[45, 46], such that the molecular dipole moment is fixed in the laboratory frame. We now show how to include a permanent molecular dipole moment in the strong-field approximation (SFA) and show that it leads to a shift in the streaking spectrum.

If the laser pulse is sufficiently weak that it does not excite the molecule, we can include the Stark shift[47] through first-order perturbation theory on the ground state. The initial state is then given by

$$|\Psi_i(t)\rangle = \exp\left[-i\int^t dt'(E_i - \vec{\mu}\cdot\vec{\mathcal{E}}(t'))\right]|\Psi_i\rangle, \tag{5.2}$$

where $\vec{\mu}$ is the fixed-in-space permanent dipole moment of the initial state and

$$|\Psi_i\rangle = \frac{1}{\sqrt{N}}\det\big|\psi_1(\vec{r}_1)\cdots\psi_N(\vec{r}_N)\big| \tag{5.3}$$

is the Slater determinant of single-particle states. For the final state, we use an unrelaxed electronic state, where $N-1$ electrons are in the same single-particle state as for the initial state and the single active electron is in the Volkov free-electron state, see Eq. (2.5). The final state is then

$$\begin{aligned}|\Psi_f(t)\rangle &= \exp\left[-i\int^t dt'(E_f^{\text{ion}} - \vec{\mu}_{\text{ion}}\cdot\vec{\mathcal{E}}(t') + \frac{1}{2}(\vec{k}_f + \vec{A}(t'))^2)\right] \\ &\times \frac{1}{\sqrt{N}}\det\big|\psi_1(\vec{r}_1)\cdots\psi_{N-1}(\vec{r}_{N-1})\frac{1}{(2\pi)^{3/2}}e^{i(\vec{k}_f+\vec{A}(t))\cdot\vec{r}_N}\big|.\end{aligned} \tag{5.4}$$

We can now calculate the transition matrix elements

$$T_{fi}(t_0) = -i\int dt\langle\Psi_f(t)|V_X(t-t_0)|\Psi_i(t)\rangle, \tag{5.5}$$

with $V_X(t) = \sum_{j=1}^N \vec{r}_j\cdot\vec{\mathcal{E}}_X(t)$. Since the interaction is a sum of single-particle operators, we can apply the Slater-Condon rules to reduce the

many-body matrix element to a one-electron matrix element

$$T_{fi}(t_0) = -i \int dt\, T^{1B}(\vec{k}_f + \vec{A}(t)) f_X(t - t_0) \tag{5.6}$$
$$\times \exp\left[i \int^t dt' \left(I_p + \Delta\vec{\mu} \cdot \vec{\mathcal{E}}(t') + \frac{1}{2}(\vec{k}_f + \vec{A}(t'))^2 \right) - i\omega_X(t - t_0) \right],$$

where $I_p = E_f^{\text{ion}} - E_i$ is the ionisation potential of the active orbital and $\Delta\vec{\mu} = \vec{\mu} - \vec{\mu}_{\text{ion}}$ is the difference in the dipole moment between the neutral molecule and the unrelaxed ion. The first Born transition amplitude is introduced and the attosecond pulse has been factored as $\vec{\mathcal{E}}(t) = \vec{\mathcal{E}}_{X,0} f_X(t) e^{-i\omega_X t}$. The calculation presented here is very similar to what was done in Sec. 2.2.

If we assume that the duration of the attosecond pulse is much shorter than the period of the laser field, we can use the fact that the integration over t has support only when $f_X(t - t_0)$ is non-vanishing. The first Born matrix element is assumed to be constant over this time and Taylor expand the exponent in the last factor to first order in $t - t_0$. We find that

$$\int^t dt' \left(I_p + \Delta\vec{\mu} \cdot \vec{\mathcal{E}}(t') + \tfrac{1}{2}(\vec{k}_f + \vec{A}(t'))^2 \right) \tag{5.7}$$
$$\approx \Phi(t_0) + (I_p + \Delta\vec{\mu} \cdot \vec{\mathcal{E}}(t_0) + \tfrac{1}{2}(\vec{k}_f + \vec{A}(t_0))^2)(t - t_0), \tag{5.8}$$

where $\Phi(t_0) = \int^{t_0} dt' \left(I_p + \Delta\vec{\mu} \cdot \vec{\mathcal{E}}(t') + \frac{1}{2}(\vec{k}_f + \vec{A}(t'))^2 \right)$. Introducing this approximation into Eq. (5.6) and recognising that the time-integral is now the Fourier transform of the attosecond pulse envelope, we find

$$T_{fi} = -iT^{1B}(\vec{k}_f + \vec{A}(t_0)) e^{i\Phi(t_0)} \tilde{f}_X(\tfrac{1}{2}(\vec{k}_f + \vec{A}(t_0))^2 + \Delta\vec{\mu} \cdot \vec{\mathcal{E}}(t_0) + I_p - \omega_X). \tag{5.9}$$

The photoelectron spectrum at a given delay, t_0, is centred around

$$E(t_0) = \omega_X - I_p - \vec{k}_f \cdot \vec{A}(t_0) - \Delta\vec{\mu} \cdot \vec{\mathcal{E}}(t_0), \tag{5.10}$$

where the A^2 term has been neglected as it is usually quite small. Eq. (5.10) should be compared to the result using the strong-field approximation without the Stark term, Eq. (2.12). The extra term shows that the oscillations are not only determined by the vector potential

through $\vec{k}_f \cdot \vec{A}(t_0)$, but modified by the Stark shift following the electric field strength, $\Delta\vec{\mu} \cdot \vec{\mathcal{E}}(t_0)$. Since the vector potential and the electric field are out of phase, the addition of the two terms leads to a phase shift.

We parametrise the vector potential as

$$\vec{A}(t) = \vec{A}_0 f_L(t) \cos(\omega_L t + \phi), \tag{5.11}$$

where $f_L(t)$ is the envelope function. If the duration of the laser pulse is several optical periods, then the electric field is approximately

$$\vec{\mathcal{E}}(t) = -\frac{d\vec{A}}{dt} \sim A_0 \omega_L f_L(t) \sin(\omega_L t + \phi). \tag{5.12}$$

To see that the result of adding a Stark term is actually a phase shift of the vector potential, we need the mathematical identity

$$\cos(x) + a\sin(x) = \sqrt{1+a^2}\cos(x + \arctan(a)). \tag{5.13}$$

With this identity, we may express the oscillations in the photoelectron spectrum as

$$\begin{aligned}
&\vec{k}_f \cdot \vec{A}(t_0) + \Delta\vec{\mu} \cdot \vec{\mathcal{E}}(t_0) \\
&\approx \vec{k}_f \cdot \vec{A}_0 f_L(t_0) \left(\cos(\omega_L t + \phi) + \omega_L \frac{\Delta\vec{\mu} \cdot \vec{A}_0}{\vec{k}_f \cdot \vec{A}_0} \sin(\omega_L t + \phi) \right) \\
&= \vec{k}_f \cdot \vec{A}_0 f_L(t_0) \sqrt{1 + \omega_L^2 \frac{(\Delta\vec{\mu} \cdot \vec{A}_0)^2}{(\vec{k}_f \cdot \vec{A}_0)^2}} \cos\left(\omega_L(t + \Delta\tau) + \phi\right) \\
&= \vec{k}_f \cdot \vec{A}(t_0 + \Delta\tau) \sqrt{1 + \omega_L^2 \frac{(\Delta\vec{\mu} \cdot \vec{A}_0)^2}{(\vec{k}_f \cdot \vec{A}_0)^2}},
\end{aligned} \tag{5.14}$$

where we have introduced the apparent temporal delay,

$$\Delta\tau = \frac{1}{\omega_L} \arctan\left(\omega_L \frac{\Delta\vec{\mu} \cdot \vec{A}_0}{\vec{k}_f \cdot \vec{A}_0} \right) \tag{5.15}$$

The value of the extra amplitude factor is very close to unity for the common parallel geometric configuration and realistic parameters. In

a parallel geometry with detection along the polarisation axis and with 800 nm light, $\Delta\mu = 5$ Debye, and $k_f = 2.5$ a.u. ($\frac{k_f^2}{2} = 85$ eV), we find $\sqrt{1 + \omega_L^2 \frac{(\Delta\vec{\mu}\cdot\vec{A}_0)^2}{(\vec{k}_f\cdot\vec{A}_0)^2}} = 1.001$. This amplitude term becomes important only if the detection is orthogonal to the polarisation of the laser field, in which case the usual streaking signal, $\vec{k}_f \cdot \vec{A}(t_0)$ is vanishing.

The main result in this section is Eq. (5.15). It serves to show that while a temporal delay in the photoemission will lead to a shift in the streaking signal, a shift in the streaking signal is not necessarily caused by a temporal delay. In the limit where $\Delta\tau$ is small compared to the optical period of the laser, arctan is nearly linear and the shift is independent of the laser frequency and the apparent shift may be difficult to separate from a true temporal delay. One very characteristic feature is however the angular dependence of the apparent shift. In Fig. 5.1 we plot the apparent shift as a function of the detection angle for RbI, which has a change in the dipole moment of 5.9 Debye[48]. We assume an electron energy of 85 eV, a laser wavelength of 800 nm and that the molecular dipole moment is aligned parallel to the polarisation of the laser.

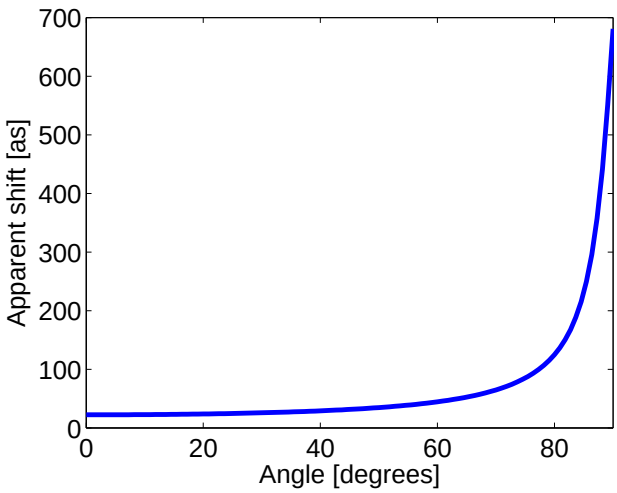

Figure 5.1 | The apparent temporal delay versus the angle between the laser polarisation and the photoelectron detection for RbI, with parameters given in the text. At 90 deg the streaking spectrum follows the electric field instead of the vector potential and the delay approaches $\frac{\pi}{2\omega_L} = 680$ asec.

When the detection is parallel to the polarisation, the temporal shift is only 22 asec, but as the direction of detection is orthogonal to the polarisation, $\vec{k}_f \cdot \vec{A}_0 \to 0$, the oscillations are only due to the Stark shift and the oscillations will follow $\Delta\vec{\mu}\cdot\vec{\mathcal{E}}(t_0)$. Since the oscillations due to the Stark shift are typically much smaller, this means that the amplitude of the oscillations is much smaller than for the parallel geometry. Since the oscillations now follow the electric field instead of the vector potential and these two are 90 deg out of phase, the signal appears to be shifted by $\frac{\pi}{2\omega_L} = 680$ asec.

5.1.1 Streaking from Stark Eigenstates in Hydrogen

The 2s and 2p states in atomic hydrogen are degenerate and when an electric field is applied along the z axis, the 2s and $2p_z$ states are mixed into two Stark eigenstates $\psi_\pm = (\psi_{200} \pm \psi_{210})/\sqrt{2}$. These states have permanent dipole moments of $\vec{\mu}_\pm = \mp 3\hat{z}$, where $\hat{z}$ is a unit vector along the z direction. The streaking spectra from these two states are shown in Fig. 5.2. The laser wavelength is 800 nm, the pulse duration is 11 fs and the intensity is 10^{12} W/cm^2. The attosecond pulse has a FWHM duration of 290 asec and a central frequency of 91 eV.

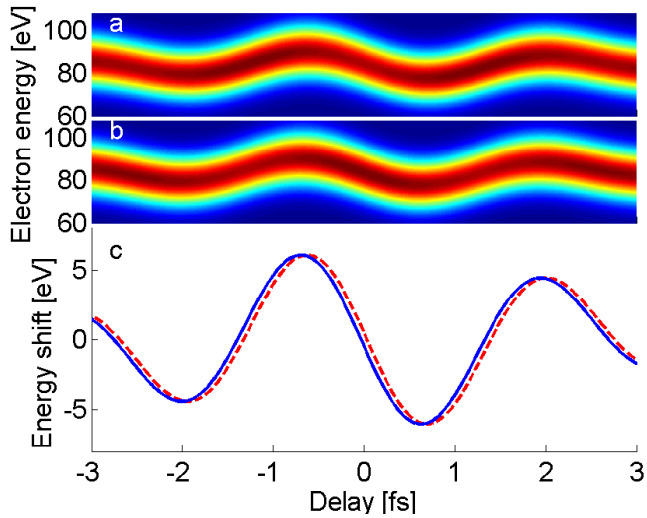

Figure 5.2 | (a) Streaking spectra from the ψ_+ state and (b) from the ψ_- state in the positive z direction. (c) Centre of energy analysis of the two spectra, showing the signal from the ψ_+ (full, blue) and the signal from the ψ_- state (dashed, red). The two signals are shifted by 60 as.

In Fig. 5.2 we see that the streaking signal is shifted by 60 asec. From the previous section, we would expect a shift of the order

$$\Delta\tau = \frac{1}{\omega_L} \arctan\left(\omega_L \frac{\Delta\vec{\mu} \cdot \vec{A}_0}{\vec{k}_f \cdot \vec{A}_0}\right) = 68 \text{ asec}, \tag{5.16}$$

showing that the analytical approximations in the previous section are reasonable.

5.1.2 Implications for Surfaces?

The surface of a solid is in many ways similar to an oriented polar molecule in the sense that the solid-vacuum interface has the same up-down symmetry breaking. The electronic states associated with the surface may hence have a permanent dipole moment and this may give rise to a similar apparent temporal delay. In the surface, very many electrons are available and the screening of the electric field makes it difficult to assess such a dipole moment. At the same time, if the electrons are able to follow the electric field on a few-fs time scale then any energy shift proportional to the electric field (as opposed to the vector potential) will give rise to an oscillation out of phase with the non-polar streaking signal and will appear as an apparent temporal delay. We have not been able to do any calculations on tungsten and hence we cannot say whether polarisation effects should be included in the interpretation of the delay measured in Ref. [6].

5.2 Wigner Time Delay

The structure of the continuum may give rise to true temporal delays in the photoionisation of atoms and molecules, known as Wigner time delays[49]. These temporal delays depend only on the atomic or molecular properties and are in this sense very fundamental.

Here, we illustrate the concept similarly to Ref. [8] by referring back

to Eq. (2.8),

$$T_{fi}(t_0) \approx -i \int dt\, T^{1B}(\vec{k}_f + \vec{A}(t)) f_X(t - t_0) \times \exp\left[\frac{i}{2}\int^t dt'(\vec{k}_f + \vec{A}(t'))^2 - iE_i t - i\omega_X(t - t_0)\right]. \tag{5.17}$$

In the strong-field approximation, we assumed that the first Born matrix element did not contain any interesting features, but if instead we assume that the phase variation is linear in the energy, then

$$T^{1B}(\vec{k}_f + \vec{A}(t)) = |T^{1B}(\vec{k}_f + \vec{A}(t))| \exp\left(i\alpha \frac{(k_f + \vec{A}(t))^2}{2}\right). \tag{5.18}$$

This adds an extra variation to the streaking signal, as was seen in the case with polar molecules. Looking at the phase in Eq. (5.17), we find that

$$\Phi(t) = \tfrac{1}{2}\int^t dt'(\vec{k}_f + \vec{A}(t'))^2 - E_i t - \omega_X(t - t_0) + \tfrac{1}{2}\alpha(k_f + \vec{A}(t))^2. \tag{5.19}$$

The average energy of the photoelectrons may be found by Taylor expanding the phase around the centre of the attosecond pulse, t_0, and looking for the stationary points. If we neglect the terms of the order A^2, we find

$$\tfrac{k_f^2}{2} = \omega_X + E_i - \vec{k}_f \cdot \vec{A}(t_0) + \alpha \vec{k}_f \cdot \vec{\mathcal{E}}(t_0). \tag{5.20}$$

The oscillations are now a sum of a contribution following the vector potential and a contribution following the electric field, as was the case in Eq. (5.10). The sum of the two gives us a phase-shifted oscillation and a time delay. We find a time delay which is

$$\Delta\tau = \frac{1}{\omega_L}\arctan(\alpha\omega_L). \tag{5.21}$$

In a more general case, the phase of the first Born transition matrix element is not necessarily linear in the kinetic energy and $\alpha = \frac{d\phi}{dE}$, where ϕ is the phase of the matrix element.

The Wigner time delay is not just an artefact of the streaking process, but a fundamental quantity in photoionisation. In a streaking experiment with ionisation from the 2s and 2p orbitals of atomic neon[8], it was found that the 2p electrons were delayed relative to the 2s electrons by 21 $\pm$ 5 asec. This delay could, however, only partially be explained by the Wigner time-delay.

5.3 Coulomb Effects

So far, we have used the strong-field approximation and neglected the effects of the residual ion. This is of course not completely accurate, and it turns out that the coupling of the laser and the Coulomb potential may also lead to temporal shifts[8, 50–52]. While the contribution from the Coulomb potential to the Wigner-time delay is analytically known, the coupling to the laser field is a theoretical challenge.

The first work showing that the combination of the Coulomb potential and the streaking laser pulse could introduce a delay in the measurement was done by Zhang and Thumm in Ref. [50]. In that work, the time-dependent Schrödinger equation (TDSE) is solved numerically in 1D for the combined action of the laser and the Coulomb potential and a model based on the semi-classical eikonal approximation is developed. In that paper, the streaking spectrum is calculated for a hydrogen atom in the ground state, exposed to a laser pulse with a duration of 5 fs, a central photon energy of 1.6 eV and an intensity of 2×10^{12} W/cm^2. The attosecond pulse has a duration of 300 asec and a variable central photon energy from 25 eV up to 90 eV. Both the numerical results and the model show that the streaking signal is shifted relative to the result of the strong-field approximation (see Sec. 2.2) and that the shift is sensitive to the photon energy, which is also the kinetic energy of the electrons. The shift decreases from 60 asec at $\omega_X = 25$ eV to about 10 asec at $\omega_X = 90$ eV. Whenever time resolved measurements are performed, the need to separate the electrons from the different channels means that the energy of the electrons must be different and hence the Coulomb-laser coupling shift is different. This shift is an artefact of the streaking measurement technique and must be understood in order to make reliable measurements on the atomic or molecular system.

In a very recent work[52] a numerical solution of the one-electron 3D TDSE and a classical-trajectory Monte Carlo simulation of the streaking spectra from the helium 1s, 2s, $2p_0$, and $2p_1$ states were calculated. In that work, where the full numerical solution of the TDSE includes both the Coulomb-laser coupling and the Wigner type time-delays, they find delays of the order 10-20 asec between the 2s and the $2p_0$ electrons, similar to what was found in the experiment from neon[8]. This work does not include any of the multi-electron effects or the structure of neon and hence cannot account for the Wigner type delay in neon. The interpretation of the delay in neon[8] still remains an open theoretical challenge.

Chapter

6 Measuring Atomic Phases through Streaking

In this chapter, we discuss how the attosecond streaking technique can be used to measure the phase of atomic or molecular ionisation matrix elements. As already discussed in Sec. 5.2, the structure of the continuum and hence the phase of the ionisation matrix elements is closely linked to the time-delay involved in the ionisation process. We show how the complete knowledge of the laser field derived from the streaking spectrum can be used to characterise the oscillations between two coupled atomic or molecular states, and how the interference in the ionisation from these states can be used to extract the relative phase of their ionisation matrix elements. In another work[17], the streaking technique is used to measure the change in the phase when the electron energy crosses a Cooper minimum or a Fano resonance. In this work, we will focus on how streaking may be used to measure the relative phase between two coupled bound states.

6.1 Laser Driven Two-Level System

We consider the situation where an initial state, $|1\rangle$, is coupled weakly by the laser field to a detuned excited state, $|2\rangle$. The coupling is such that only a small part of the initial state population is transferred to $|2\rangle$ and only while the driving laser pulse is on, adiabatically following the

laser pulse envelope.

The two-level system is described by the wave function

$$|\Psi(t)\rangle = c_1(t)e^{-iE_1t}|1\rangle + c_2(t)e^{-iE_2t}|2\rangle, \tag{6.1}$$

with E_1 the ground state energy, E_2 the excited state energy and with the initial conditions $c_1(-\infty) = 1$ and $c_2(-\infty) = 0$. The total Hamiltonian of the system is

$$H = H_0 + V_L(t), \tag{6.2}$$

where H_0 is the field-free atomic or molecular Hamiltonian for which the two states are eigenstates, $H_0|i\rangle = E_i|i\rangle$ and $V_L(t)$ is the interaction with the electromagnetic field. The coefficients $c_i(t)$ may be found by solving the set of coupled differential equations

$$i\dot{c}_1 = \langle 1|V_L(t)|1\rangle c_1 + \langle 1|V_L(t)|2\rangle e^{i(E_1-E_2)t}c_2 \tag{6.3}$$

$$i\dot{c}_2 = \langle 2|V_L(t)|1\rangle e^{-i(E_1-E_2)t}c_1 + \langle 2|V_L(t)|2\rangle c_2. \tag{6.4}$$

We treat the interaction in the length gauge and parametrise the interaction as

$$\langle 1|V_L(t)|2\rangle = \rho\mathcal{E}(t), \tag{6.5}$$

where ρ is the dipole transition matrix element along the laser polarisation direction or the coupling strength. For simplicity, we assume that the two states are parity Eigenstates, such that $\langle i|V_L(t)|i\rangle = 0$. The set of equations can now be solved either numerically or analytically. Here we are interested in the regime when the detuning, δ, is large

$$\delta = E_2 - E_1 - \omega_L > \rho\mathcal{E}. \tag{6.6}$$

In this regime, there are no Rabi oscillations and the population in the excited state follows the field adiabatically. When the detuning is very large, $\delta \gg \rho\mathcal{E}$, we can employ the rotating wave approximation and an approximate solution to the time evolution is $c_1(t) \approx 1$ and

$$c_2(t) \approx -i\int^t dt'\rho\mathcal{E}(t')e^{i(E_2-E_1)t'} \approx -\frac{\rho\mathcal{E}_0(t)e^{i\delta t}}{2\delta}e^{-i\phi}, \tag{6.7}$$

where $\mathcal{E}(t) = \mathcal{E}_0(t)\cos(\omega_L t + \phi)$ with $\mathcal{E}_0(t)$ the envelope function and ϕ the carrier-envelope phase. In this regime, the relative phase evolution of the two terms in Eq. (6.1) is determined by the laser frequency,

independently of the energy difference between the two levels and the population follows the envelope of the laser pulse.

We consider a system where the coupling between the two states is equal to one Bohr radius, $\rho = a_0$ and the energy difference between the two levels is 1.85 eV corresponding to the difference between the ground state and the first excited state in atomic lithium. The laser pulse is centred around 800 nm, has a 50 fs duration, a sine-squared envelope and a peak intensity of $I = 10^{12}$ W/cm^2. The excited state population is plotted in Fig. 6.1.

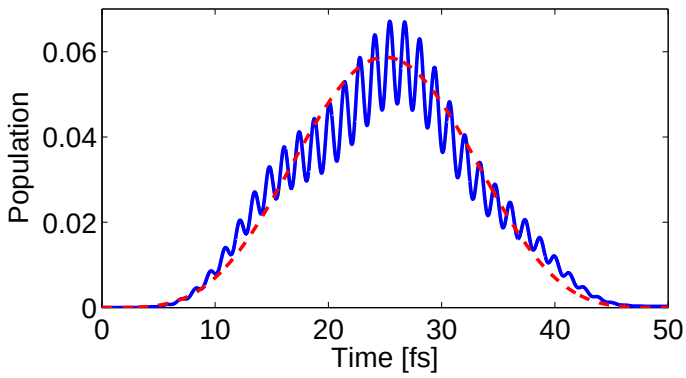

Figure 6.1 | Numerically calculated excited state population $|c_2(t)|^2$ (blue) and the approximate value from Eq. (6.7) (red). The laser and system parameters are given in the text.

The population transfer is at all times less than 7%. The oscillations in the numerical solution are due to the off resonant term and the lack of oscillations in the approximate result shows that while first order perturbation theory is valid, the rotating wave approximation is questionable. If we calculate the excited state population without the rotating wave approximation, the result fits the numerical result nicely (not shown). The interpretation and the discussion of the phase retrieval is however much simpler within the rotating wave approximation and we proceed with the discussion based on the approximation, while the results shown are calculated from a numerical solution.

6.2 Attosecond Ionisation from Laser Driven Two-Level System

We want to characterise the phase between the two terms in Eq. (6.1) by ionisation with an attosecond pulse. The energy difference between the two levels is much smaller than the spectral width of an isolated attosecond pulse so that the electron contributions from the two states interfere in the continuum. This is illustrated in Fig. 6.2.

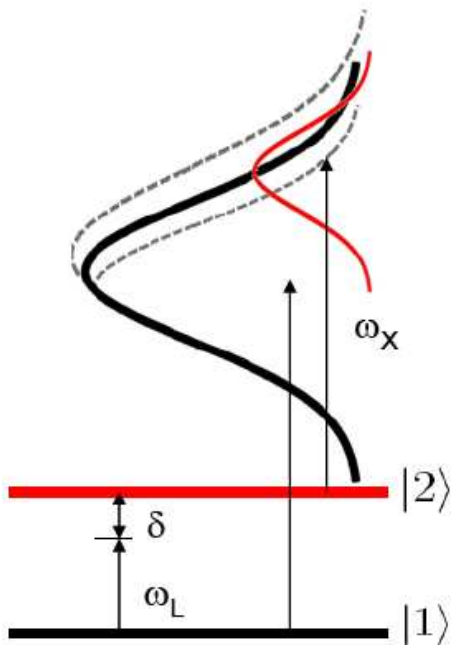

Figure 6.2 | Schematic view of the ionisation process. The levels $|1\rangle$ and $|2\rangle$ are coupled by the laser field of frequency ω_L and detuning δ. The spectral width of the attosecond pulse of frequency ω_X is sufficiently large that photoelectrons from both levels overlap energetically. The interference between the two ionisation channels in the overlapping region carries a signature of the phase difference between the ionisation matrix elements. The interference may be either constructive or destructive (dashed lines).

We refer back to Sec. 2.2 and calculate the transition matrix element for a transition from the initial superposition state to a final state with asymptotic momentum, $\vec{k}_f$, as

$$T_{fi}(t_0) = -i \int dt \langle \vec{\Psi}_f(t) | V_X(t - t_0) | \Psi(t) \rangle. \tag{6.8}$$

We once again approximate phase evolution of the final state with the Volkov phase and assume that the final state may be factored as

$$|\Psi_f(t)\rangle = |\vec{k}_f\rangle \exp\left[-\frac{i}{2}\int^t dt'(\vec{k}_f + \vec{A}(t'))^2\right], \tag{6.9}$$

where $|\vec{k}_f\rangle$ is the scattering state with asymptotic momentum $\vec{k}_f$. We may factorise the transition matrix elements from each of the two bound states as

$$\langle \vec{k}_f|V_X(t-t_0)|n\rangle = M_n(\vec{k}_f)\vec{\mathcal{E}}_X(t-t_0), \qquad n = 1,2 \tag{6.10}$$

where $M_n(\vec{k}_f)$ is the transition matrix element from the initial state n to a final state with momentum $\vec{k}_f$ and $\vec{\mathcal{E}}_X$ is the electric field of the attosecond pulse. With this factorisation we find that

$$\langle \vec{k}_f|V_X(t-t_0)|\Psi(t)\rangle = \sum_{n=1,2} c_n(t)e^{-iE_n t}M_n(\vec{k}_f)\vec{\mathcal{E}}_X(t-t_0). \tag{6.11}$$

Introducing the approximation for the coefficients from Eq. (6.7), we can calculate the transition matrix elements

$$\begin{aligned} T_{fi}(t_0) &= -i\sum_{n=1,2} M_n(\vec{k}_f)\int dt\vec{\mathcal{E}}_X(t-t_0)c_n(t)e^{\frac{i}{2}\int^t dt'(\vec{k}_f+\vec{A}(t'))^2 - iE_n t} \\ &\approx -iM_1(\vec{k}_f)e^{-iE_1t_0}\int dt\vec{\mathcal{E}}_X(t-t_0)e^{\frac{i}{2}\int^t dt'(\vec{k}_f+\vec{A}(t'))^2 - iE_1(t-t_0)} \\ &+iM_2(\vec{k}_f)\frac{\rho\mathcal{E}_0(t_0)e^{-i(E_1+\omega_L)t_0 - i\phi}}{2\delta}\int dt\vec{\mathcal{E}}_X(t-t_0)e^{\frac{i}{2}\int^t dt'(\vec{k}_f+\vec{A}(t'))^2 - i(E_1+\omega_L)(t-t_0)}, \end{aligned} \tag{6.12}$$

where we have used that $E_2 - \delta = E_1 + \omega_L$. If we Taylor expand the integral as was done in Sec. 2.2 (Eqs. (2.8) to (2.11)), we may evaluate the integral as the Fourier transform of the attosecond pulse. The result is

$$\begin{aligned} T_{fi}(t_0) &\approx -iM_1(\vec{k}_f)e^{-iE_1t_0}\vec{\mathcal{E}}_{X,0}\tilde{f}_X(\tfrac{1}{2}(\vec{k}_f + \vec{A}(t_0))^2 - E_1 - \omega_X) \\ &+iM_2(\vec{k}_f)\frac{\rho\mathcal{E}_0(t_0)e^{-i(E_1+\omega_L)t_0 - i\phi}}{2\delta}\vec{\mathcal{E}}_{X,0}\tilde{f}_X(\tfrac{1}{2}(\vec{k}_f + \vec{A}(t_0))^2 - E_1 - \omega_L - \omega_X). \end{aligned} \tag{6.13}$$

The spectral width of the attosecond pulse is much greater than the energy difference between the two bound states as discussed above. In the energy domain, the electrons coming from each of the two states will therefore overlap and interfere. The electron energy distribution from each of the two terms is determined by the temporal integral. The total (energy integrated) ionisation probability for electron emission in the direction determined by $\vec{k}_f$ is (see Eq. (2.14))

$$P(t_0) = \int dE\, 2\sqrt{2E}|T_{fi}|^2 \tag{6.14}$$

$$= \int dE\, 2\sqrt{2E}\left|M_1(\vec{k}_f)\hat{f}_X(E_1) - M_2(\vec{k}_f)\frac{\rho\mathcal{E}_0(t_0)e^{-i\omega_L t_0 - i\phi}}{2\delta}\hat{f}_X(E_1+\omega_L)\right|^2,$$

where we have introduced $\hat{f}_X(E) = \tilde{f}_X(\frac{1}{2}(\vec{k}_f + \vec{A}(t_0))^2 - E - \omega_X)$ for brevity. We introduce the symbol K, and we use the fact that the attosecond pulse is wide, to assume that

$$K = \int dE 2\sqrt{2E}\hat{f}_X(E_1)^2 \approx \int dE 2\sqrt{2E}\hat{f}_X(E_1)\hat{f}_X(E_1+\omega_L), \tag{6.15}$$

where we have also assumed that the attosecond pulse is symmetric around $t = 0$, such that the Fourier transform is real. With these assumptions and keeping only the two leading terms, we find that the total ionisation probability is proportional to

$$\begin{aligned} P(t_0) &\approx K\left|M_1(\vec{k}_f) - M_2(\vec{k}_f)\frac{\rho\mathcal{E}_0(t_0)e^{-i\omega_L t_0 - i\phi}}{2\delta}\right|^2 \\ &\propto 1 - C\mathcal{E}_0(t_0)\frac{\rho}{\delta}\cos(\omega_L t_0 + \phi + \Theta), \end{aligned} \tag{6.16}$$

where the ratio between the ionisation matrix elements has been rewritten as

$$\frac{M_2(\vec{k}_f)}{M_1(\vec{k}_f)} = Ce^{i\Theta}, \tag{6.17}$$

and the term that is quadratic in the excited state population has been neglected. The relative phase between the two matrix elements, Θ, is the primary object of interest. The above result shows that the energy integrated ionisation probability oscillates with the periodicity of the

laser pulse when varying the relative delay between the laser and the attosecond pulse. These oscillations are the basis for the phase retrieval procedure presented below.

6.3 Retrieving Ionisation Phases from Streaking Spectra

The mean kinetic energy of the electrons released oscillates with the periodicity of the laser field, as

$$\Delta E(t_0) = -\vec{k}_f \cdot \vec{A}(t_0) = -\frac{\vec{k}_f \cdot \vec{\mathcal{E}}_0(t_0)}{\omega_L} \sin(\omega_L t_0 + \phi). \tag{6.18}$$

These observations lead to a three-step algorithm for retrieving the relative phase between the two states, Θ;

i) Measure the streaking spectrum, $S(E, t_0)$, i.e., the photoelectron distribution against the delay between the two pulses, t_0.

ii) Calculate the energy integrated ionisation probability,

$$P(t_0) = \int dE S(E, t_0) \tag{6.19}$$

and the energy shift

$$\Delta E(t_0) = \int dE (E - E_0) S(E, t_0)/P(t_0) \tag{6.20}$$

from the measured data. E_0 is the average energy when there is no overlap between the two pulses.

iii) Retrieve the phase, Θ, from the two curves by fitting

$$P(t_0) - P(-\infty) \propto \Delta E \left(t_0 - \tfrac{\Theta - \pi/2}{\omega_L} \right). \tag{6.21}$$

We will denote the reconstructed phase from the three-step algorithm by Θ_r. As will be discussed in the following section, the interference from

the two bound states may also lead to a phase shift in the streaking signal. This shift can be corrected for as shown in Sec. 6.4 below.

We show two examples of phase retrievals. The laser parameters are in both cases the same as in Sec. 6.1. The wavelength is 800 nm, the pulse duration is 50 fs and the intensity is 10^{12} W/cm^2. The attosecond pulse has a FWHM duration of 290 asec and a central photon energy of 91 eV. The target system is lithium like, with a ground state ionisation potential of 5.39 eV and an energy separation between the ground state and the first excited state of 1.85 eV. We assume that the electrons are detected parallel to the laser polarisation direction. The set of equations coupling the ground and the excited state, Eqs. (6.3), are solved numerically.

In the first example, we assume that the two ionisation matrix elements are equal in magnitude and $\pi/2$ out of phase, such that $M_2(\vec{k}_f) = iM_1(\vec{k}_f)$. This would be the case if $|\vec{k}_f\rangle$ is assumed to be a plane wave and the two states have opposite inversion symmetry along the line of detection, such as if the ground state has s symmetry and the excited state has p symmetry and is directed along the line of detection. The result is shown in Fig. 6.3.

The energy shift and the energy integrated ionisation probability is plotted in Fig. 6.3(b). The two curves oscillate in phase, which is a signature that the phase of the ionisation matrix elements is $\pi/2$ out of phase. When fitting the two curves as devised in the three-step algorithm, the reconstructed phase is $\Theta_r = \pi/2 - 0.004$, deviating only 4 mrad from the true value.

In another example, we use the same set of pulse parameters, but assume that the two ionisation matrix elements have the same phase, such that $M_2(\vec{k}_f) = M_1(\vec{k}_f)$. We again calculate the streaking spectrum, the ionisation probability and the energy shifts. The result is shown in Fig. 6.4.

Retrieving the relative phase of the matrix elements, we find $\Theta_r = 0.0476$. This result deviates more from the true value of 0, than was the case in the first example presented above. The reason for this deviation is discussed in the following section.

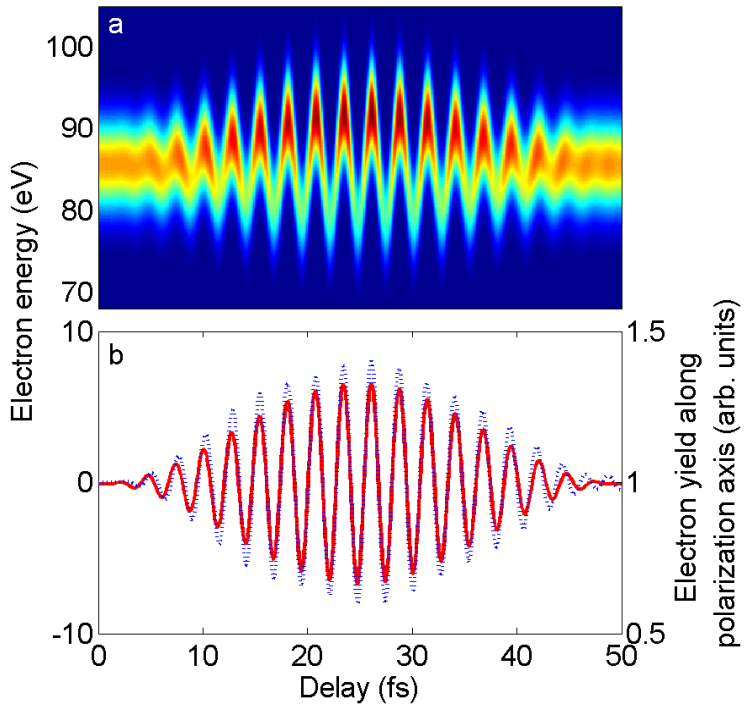

Figure 6.3 | (a) Photoelectron spectrum as a function of delay between the laser and the attosecond pulse, from the laser driven two-level system discussed in the text. (b) The energy shift (full, red) and the energy integrated ionisation yield (dashed, blue). The two curves oscillate in phase, which is a signature of the $\pi/2$ phase difference between the two matrix elements M_1 and M_2.

6.4 Streaking Phase Shifts from Interference

The interference between the two different ionisation channels may cause a shift in the streaking spectrum, such that the center of energy follows

$$\Delta E(t_0) = -\frac{\vec{k}_f \cdot \vec{\mathcal{E}}_0(t_0)}{\omega_L} \sin(\omega_L t_0 + \phi + \Delta), \tag{6.22}$$

where Δ is the phase shift induced by the interference. The origin of this phase shift can be seen from Fig. 6.2. In the regime of interest the primary contribution is always from the ground state. The contribution from the excited state is much smaller and is either constructive or destructive, depending on the relative phase. Since the contribution from

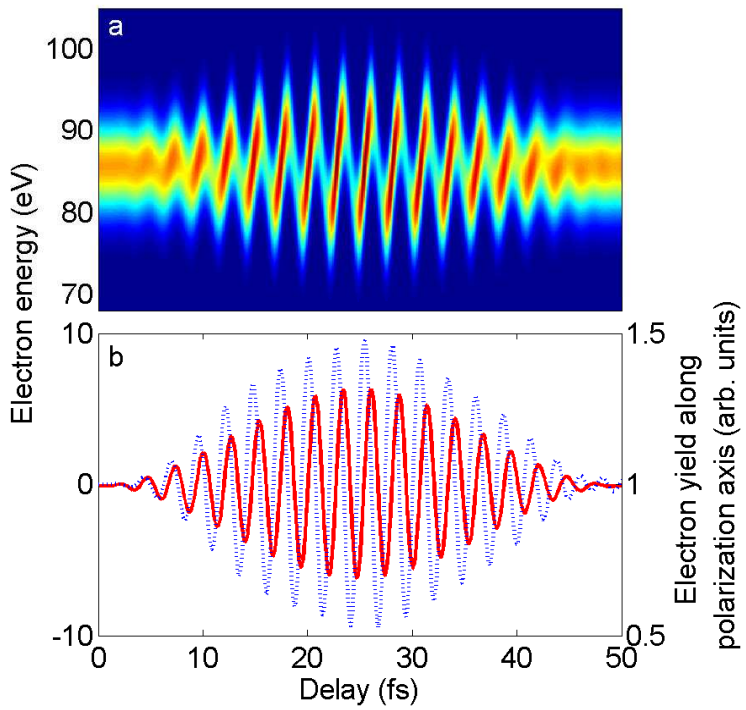

Figure 6.4 | (a) Photoelectron spectrum from the laser driven two-level system discussed in the text, similar to Fig. 6.3(a), but with the two matrix elements in phase. (b) The energy shift (full, red) and the energy integrated ionisation yield (dashed, blue). The two curves oscillate $\pi/2$ out of phase, which is a signature of the two matrix elements M_1 and M_2 being in phase.

the excited state is at a higher energy, constructive interference means that the average energy of the electrons is higher, while destructive interference leads to a lower average electron energy. This is illustrated in Fig. 6.2 with the gray, dashed lines. If the constructive (destructive) interference coincides with the maxima of the of the energy shift, $\Delta E(t_0)$, this leads to a bigger (smaller) amplitude for the oscillations. If the interference is shifted in phase relative to the streaking spectrum, this leads to a phase shift. This is the case when $e^{i\Theta}$ has a real part.

To quantify the shift, we calculate the average energy as

$$E_{av}(t_0) = \int dE\, 2\sqrt{2E}E|T_{fi}(t_0)|^2/P(t_0), \tag{6.23}$$

and refer back to Eq. (6.13). Very similar to the treatment in Sec. 6.2, we assume that the spectral width of the attosecond pulse is very large

and we neglect the part that is second order in c_2. If the matrix elements do not vary over the width of the laser pulse, we find

$$E_{av}(t_0)P(t_0) \approx |M_1|^2 \int dE 2\sqrt{2E}E\hat{f}(E_1)^2 \tag{6.24}$$
$$-2\mathrm{Re}\Big(M_1 M_2 \frac{\rho\mathcal{E}(t_0)e^{-i\omega_L t_0 - i\phi}}{2\delta}\Big) \int dE\, 2\sqrt{2E}E\hat{f}(E_1)\hat{f}(E_1+\omega_L),$$

where the momentum dependence of the matrix elements is implied. The centre of energy for the distribution is

$$\int dE 2\sqrt{2E}E\hat{f}(E_1)^2 = E_0 K, \tag{6.25}$$

where K was introduced in Eq. (6.15) and $E_0 = \omega_X + E_1 - \vec{k}_f \cdot \vec{A}(t_0)$. Since the distribution of the electrons is wide compared to the laser photon energy, the product of the two distribution functions in the second term in Eq. (6.24) is peaked around $E_0 + {}^{\omega_L}/_2$ and we can approximate

$$\int dE\, 2\sqrt{2E}E\hat{f}(E_1)\hat{f}(E_1+\omega_L) \approx (E_0 + {}^{\omega_L}/_2)\, K. \tag{6.26}$$

With these approximations, we can calculate the average energy through

$$\begin{aligned} E_{av}(t_0)P(t_0) &= |M_1|^2 K E_0 \left[1 - C\frac{\rho\mathcal{E}(t_0)}{\delta}\cos(\omega_L t_0 + \phi + \Theta)\right] \\ &\quad -|M_1|^2 K \frac{\omega_L}{2} C \frac{\rho\mathcal{E}(t_0)}{\delta}\cos(\omega_L t_0 + \phi + \Theta). \end{aligned} \tag{6.27}$$

The parenthesis in the first term is exactly the ionisation probability, $P(t_0)$, found in Eq. (6.16). Neglecting the terms of the order c_2^2, we approximate ${}^{|M_1|^2 K}/_{P(t_0)} \approx 1$ in the second term and we find the final result

$$E_{av}(t_0) \approx \omega_X + E_1 - \vec{k}_f \cdot \vec{A}(t_0) - \frac{C\rho\mathcal{E}(t_0)\omega_L}{2\delta}\cos(\omega_L t_0 + \phi + \Theta). \tag{6.28}$$

The first oscillating term is

$$\vec{k}_f \cdot \vec{A}(t_0) = \frac{\vec{k}_f \cdot \vec{\mathcal{E}}_0(t_0)}{\omega_L}\sin(\omega_L t_0 + \phi), \tag{6.29}$$

such that the two contributions are out of phase unless $\Theta = \pm\pi/2$. We use the trigonometric identity

$$\cos(\omega_L t_0+\phi+\Theta) = \cos(\omega_L t_0+\phi)\cos(\Theta)-\sin(\omega_L t_0+\phi)\sin(\Theta). \quad (6.30)$$

Here, we are interested in assessing the magnitude of the delay. The second term is oscillating in phase with the streaking signal and therefore leads to no delay, but only a change in the amplitude. The first term is the interesting part as it oscillates out of phase

$$\begin{aligned}\Delta E(t_0) &\approx -\frac{\vec{k}_f\cdot\vec{\mathcal{E}}_0(t_0)}{\omega_L}\left[\sin(\omega_L t_0+\phi)+\frac{C\rho\mathcal{E}(t_0)\omega_L^2}{2\delta\vec{k}_f\cdot\vec{\mathcal{E}}(t_0)}\cos(\Theta)\cos(\omega_L t_0+\phi)\right]\\ &= -\frac{\vec{k}_f\cdot\vec{\mathcal{E}}_0(t_0)}{\omega_L}\sqrt{1+\tan(\Delta)^2}\sin(\omega_L t_0+\phi+\Delta), \quad (6.31)\end{aligned}$$

with

$$\Delta = \arctan\left(\frac{C\rho\omega_L^2}{2\delta\vec{k}_f\cdot\vec{\epsilon}_L}\cos(\Theta)\right), \quad (6.32)$$

where $\vec{\epsilon}_L$ is the laser polarisation vector. This formula shows that if $e^{i\Theta}$ has a real part, then the strong-field approximation does not accurately describe the phase of the electron energy oscillation. This is important both for time-resolved measurements and for phase reconstruction as described in the previous section. The reconstructed phase from the three-step algorithm should be corrected for this effect, through

$$\Theta_R = \Theta_r - \Delta, \quad (6.33)$$

where Θ_R is the corrected phase. For the example presented in Fig. 6.4, we find that $\Delta = 0.0589$ and we find $\Theta_R = -0.0113$ in better agreement with the true phase, $\Theta = 0$. The reconstruction is still not perfect, but now deviates by only 11 mrad. The approximations introduced in the calculation of Δ may be part of the explanation for the deviation.

As another example, where the shift is even greater, we now consider a driving laser pulse with a wavelength of 750 nm, closer to resonance for the lithium-like system and with a lower intensity of 10^{11} W/cm^2. The attosecond pulse is the same as in the previous examples, a FWHM duration of 290 asec and a central photon energy of 91 eV. The results are shown in Fig 6.5.

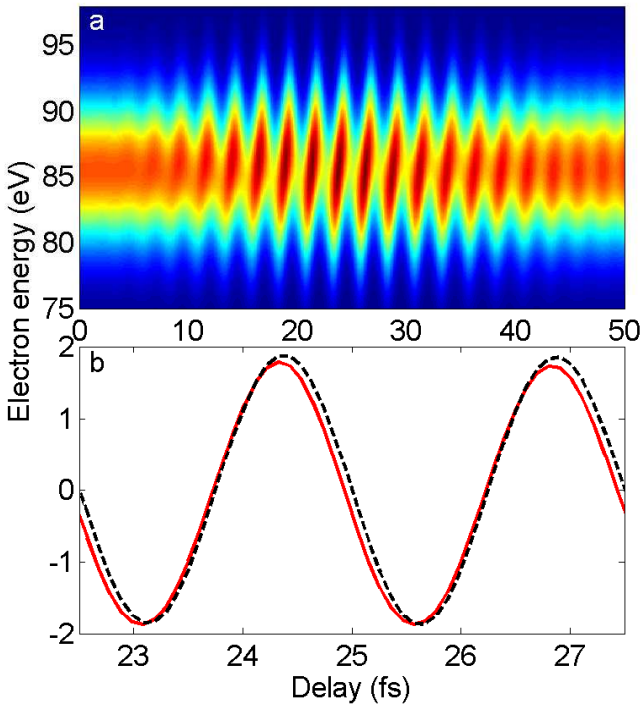

Figure 6.5 | (a) Photoelectron spectrum from the laser driven two-level system presented in the text. (b) Part of the centre of energy (full, red) is plotted along with the strong-field approximation estimate of the energy variation from Eq. (2.12) (dashed, black). The two curves are displaced by 40 asec or 0.1026 rad.

In part (b) of the figure, the centre of energy is plotted with the estimate from the strong-field approximation. The two are shifted and the oscillations are 0.1026 rad or 40 asec out of phase with the simple estimate. The shift calculated in using Eq. (6.32) is $\Delta = 0.1065$ or $\Delta/\omega_L = 41$ asec explains this. If the objective is a time-resolved measurement using the streaking technique, then the shift due to coupling to an excited state may be considered a complication. The analysis in this section shows how to compensate this shift.

6.5 Application for Phase Measurements

While we have mostly discussed the atomic case here, the theory applies equally well to molecules. The effect of a molecular permanent dipole moment would again give rise to shifts in the streaking spectrum as

discussed in Sec. 5.1. In order to accurately retrieve molecular phases, one must know the permanent dipole moment to correct for it or have access to a reference state, ideally with no dipole moment and no near resonances. Access to the phase of the ionisation matrix element is a way to test theory and to get another view towards the Wigner time-delays as discussed in Sec 5.2. The ability to vary the photon energy in the attoscond pulse will allow a series of measurements to scan the phase dependence for different electron energies. The Wigner time-delay is related to the energy derivative of the phase.

Another interesting aspect is the fact that the electron energy is affected by the Coulomb-laser coupling, while the ionisation probability is not. This means that the method presented in this chapter may be able to make absolute measurements of the shift due to the Coulomb-laser coupling. Using atomic lithium as a target, the ground state has s symmetry and the first excited state has p symmetry. Performing the experiment with the detection parallel to the laser polarisation means that the laser will excite the p state along the polarisation axis. These states have opposite symmetry and we should expect the ionisation probability and electron energy to oscillate in phase as was seen in Fig. 6.3. The phase shift discussed in Sec. 6.4 vanishes and the phase deviation will be due entirely to the Coulomb-laser coupling. By scanning through different attosecond pulse photon energies one should be able to directly measure the Coulomb-laser coupling, which is otherwise very difficult to identify.

Chapter

7 Attosecond Pulse Trains

In the previous sections, we have discussed how the combination of an isolated attosecond pulse with an intense laser field may be used for time-resolved measurements on a sub-femtosecond time-scale through the attosecond streaking technique. In this section we will discuss how a very similar approach, with a train of attosecond pulses in combination with the fundamental laser field may be used to provide similar temporal resolution.

If a laser pulse with several optical periods is used to make high-order harmonics, the generated radiation forms a train of attosecond pulses[18] with two pulses for each optical period (corresponding to one pulse for each extremum of the field). If the laser field is combined with the second harmonic, the up-down symmetry of the field is broken and one can produce a pulse train with only one attosecond pulse per optical period[53, 54]. With one attosecond pulse per optical cycle, all electrons liberated by the attosecond pulses are born at the same phase of the laser field and we find a streaking signal very similar to what was seen for the isolated pulses. With two pulses per cycle, the frequency spectrum of the pulse train consists of only the odd harmonics. When the fundamental laser field is added, a process like the laser assisted photoelectric effect leads to electrons with an energy corresponding to an even harmonic, $2n$. This final energy can be reached either by absorbing a photon with energy $(2n-1)\omega_L$ from the pulse train and absorbing a

photon from the laser field or by absorbing a photon with energy $(2n+1)\omega_L$ and emitting a photon into the laser field by stimulated emission. The interference between these two pathways is sensitive to the relative delay between the pulse train and the laser field[18, 19, 55]. Both these situations are discussed and modelled through the same approach as was taken in the previous chapters. The latter is the basis of the so-called RABBITT technique and its application to time- and phase-resolved measurements[9, 20, 56] is discussed.

7.1 Pulse Train Description

As before, we consider the Hamiltonian

$$H = H_0 + V_L(\vec{r}, t) + V_X(\vec{r}, t - t_0) \tag{7.1}$$

The interactions with the electromagnetic fields are in the length gauge. The difference from the earlier chapters is in the shape of the pulses. The electric field from the attosecond pulse train is given by

$$\vec{\mathcal{E}}_X(t) = \vec{\mathcal{E}}_{X,0} \sum_{n=0}^{N-1} f_X\left(t - \tfrac{nT}{\kappa}\right) e^{-i(\omega_X t + n\phi_X)}, \tag{7.2}$$

where N is the number of attosecond pulses in the train, $f_X(t)$ is the pulse envelope function, $T = {}^{2\pi}/_{\omega_L}$ is the optical period of the fundamental field, κ is the number of pulses per optical period (we consider $\kappa = 1, 2$), ω_X is the central frequency of the attosecond pulses and ϕ_X is the relative phase between the pulses, which we assume to be constant. We assume that the duration of the individual attosecond pulses is much shorter than the optical period of the fundamental field. We give a description in the time-domain, but the pulse is of course equally well described in the frequency-domain.

The laser pulse is assumed to be very long, such that we may neglect the envelope function

$$\vec{\mathcal{E}}(t) = \vec{\mathcal{E}}_0 \sin(\omega_L t + \phi). \tag{7.3}$$

7.2 One Attosecond Pulse per Laser Period

While the case with two pulses per laser period is perhaps the most interesting, we treat the case with only one pulse first, to use this result in the next section. We calculate the transition matrix elements similar to what was done in Sec. 2.2 and use the same Volkov wave functions for the final state,

$$\begin{aligned} T_{fi}(t_0) &= -i \int dt \langle \Psi_f(\vec{r},t)|V_X(\vec{r},t-t_0)|\Psi_i(\vec{r},t)\rangle \qquad (7.4) \\ &= -i \sum_{n=0}^{N-1} e^{-in\phi_X} \int dt\, T^{1B}(\vec{k}_f + \vec{A}(t)) f_X(t-t_0-nT) \qquad (7.5) \\ &\quad \times \exp\left[\frac{i}{2}\int^t dt'(\vec{k}_f + \vec{A}(t'))^2 - iE_i t - i\omega_X(t-t_0)\right]. \end{aligned}$$

In each of the temporal integrations, the integrand only has support when the attosecond pulse is on, such that $t \sim t_0 + nT$. Since the electric field is assumed to be long, the vector potential is also periodic with period T, such that $\vec{A}(t+nT) = \vec{A}(t)$ for any integer n. This implies that

$$\int_0^{nT} dt'(\vec{k}_f + \vec{A}(t'))^2 = n\int_0^T dt'(\vec{k}_f + \vec{A}(t'))^2 = nT\left(k_f^2 + \frac{\mathcal{E}_0^2}{2\omega_L^2}\right), \quad (7.6)$$

where we use the fact that the vector potential is sinusoidal. We may now change the integration variable $t \to t - t_0 - nT$ in Eq. (7.5)

$$\begin{aligned} T_{fi}(t_0) &= -i \sum_{n=0}^{N-1} e^{-in\phi_X} \int dt\, T^{1B}(\vec{k}_f + \vec{A}(t+t_0)) f_X(t) \qquad (7.7) \\ &\times \exp\left[\frac{i}{2}\int^{t+t_0+nT} dt'(\vec{k}_f + \vec{A}(t'))^2 - iE_i(t+t_0+nT) - i\omega_X(t+nT)\right]. \end{aligned}$$

where the support is now around $t = 0$. To perform the integrals analytically, we assume that the first Born matrix element is almost constant and Taylor expand the terms in the exponent to first order in t. If we

again neglect terms of the order A^2, we find that

$$T_{fi}(t_0) = -iT^{1B}(\vec{k}_f + \vec{A}(t_0)) \sum_{n=0}^{N-1} \exp\left[-in\phi_X + inT\left(\frac{k_f^2}{2} - E_i - \omega_X\right)\right]$$
$$\times e^{i\Phi(t_0)} \int dt f_X(t) \exp\left[i\frac{k_f^2}{2}t + i\vec{k}_f \cdot \vec{A}(t_0)t - iE_i t - i\omega_X t\right], \quad (7.8)$$

where $\Phi(t_0) = \frac{1}{2}\int^{t_0} dt'(\vec{k}_f + \vec{A}(t'))^2 - E_i t_0$ is an overall phase that does not influence the photoelectron spectrum. We recognise the last term as the Fourier transform of one of the attosecond pulses and the sum as the geometric series. We may then perform both analytically and find

$$\begin{aligned} T_{fi}(t_0) &= -ie^{i\Phi(t_0)}T^{1B}(\vec{k}_f + \vec{A}(t_0))\tilde{f}_X(\tfrac{k_f^2}{2} + \vec{k}_f \cdot \vec{A}(t_0) - \omega_X - E_i) \\ &\times \frac{1 - \exp\left[-iN\left(\phi_X - T(k_f^2/2 - E_i - \omega_X)\right)\right]}{1 - \exp\left[-i\left(\phi_X - T(k_f^2/2 - E_i - \omega_X)\right)\right]}. \end{aligned} \quad (7.9)$$

This result should be compared to Eq. (2.11) which is the result for the isolated attosecond pulse. The two results are identical except for the last fraction, which is the result of the interference from the different attosecond pulses. For $N = 1$ the result for the isolated attosecond pulse is reproduced. The result of the interference is that the broad spectrum of photoelectron energies is split into narrow peaks, with a peak when

$$\phi_X - T(\tfrac{k_f^2}{2} - E_i - \omega_X) \to 2\pi k, \qquad k \text{ integer}. \quad (7.10)$$

When this condition is fulfilled, the fraction approaches N. The photoelectron spectrum is proportional to the norm-square of the T-matrix elements, such that the height of the peaks scales with the number of attosecond pulses as N^2. The width, on the other hand, scales as N^{-1}, such that the number of electrons released is linear in N.

As an example, we calculate the photoelectron spectrum for an infinitely long laser pulse with a wavelength of 800 nm and an intensity of 2×10^{11} W/cm^2, and a train of N Gaussian attosecond pulses with a FWHM duration of 290 asec, a central frequency of $\omega_X = 91$ eV and $N = 1, 2, 8$. We assume that the first Born matrix element is constant and have arbitrarily chosen the binding energy to be 1 atomic unit. The results are shown in Fig. 7.1.

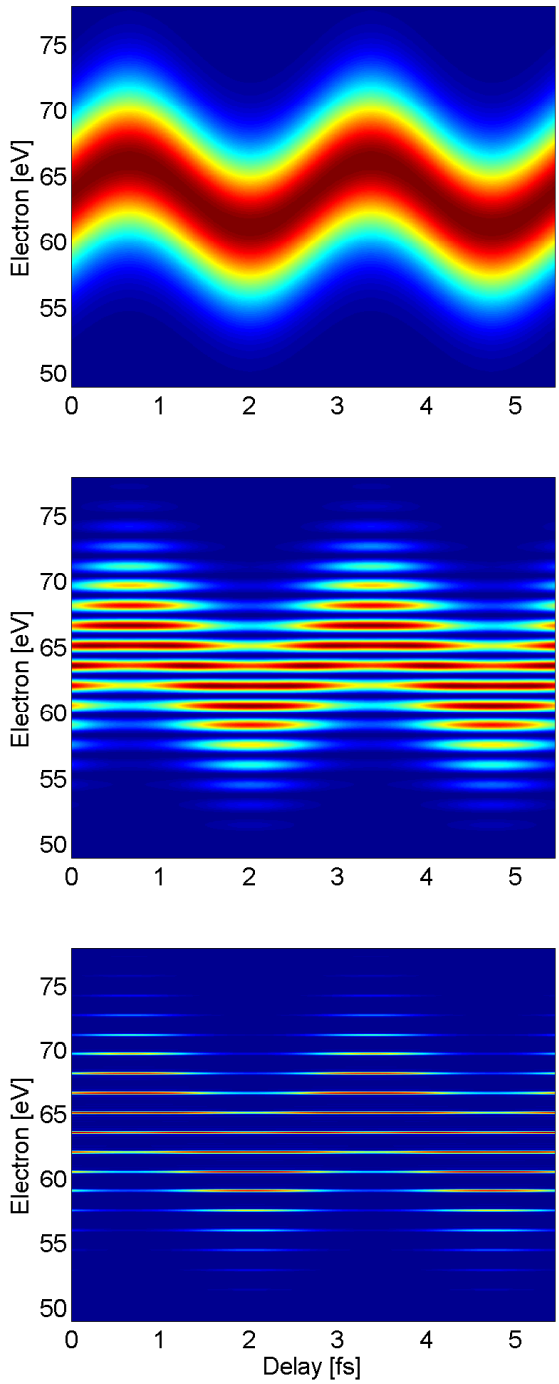

Figure 7.1 | Photoelectron spectra for an isolated attosecond pulse (top). The laser field is considered infinitely long and the spectrum is therefore periodic in time. The duration of the attosecond pulse is 290 asec, while the laser has an intensity of 2×10^{11} W/cm^2 and a wavelength of 800 nm. (middle) The same, but with two attosecond pulses one optical cycle apart. (bottom) The same, but with 8 attosecond pulses each separated by one optical cycle.

In the spectra we see that the energy distribution is continuous for the isolated attosecond pulse, while it is discretised for the attosecond pulse trains. The peaks are separated by the fundamental laser frequency. The width of the peaks is much narrower for 8 pulses than for 2, as previously discussed, and this trend continues if we move to even longer trains.

The spectra show the same oscillation for the pulse trains as for the isolated attosecond pulse. The streaking signal from a train of attosecond pulses may therefore be used in time-resolved measurements. In this example we have considered an infinite laser pulse and the streaking signal is periodic in the relative delay with the periodicity of the laser field. This means that we cannot decide whether streaking signals originating from two different ionisation channels are shifted by an integer number of full periods. If we know that the shift is only a small fraction of a period it is equally viable and in practice, the laser pulse will never be infinitely long.

7.3 Two Attosecond Pulses per Laser Period

The more interesting case is when there are two attosecond pulses per optical period of the fundamental field, corresponding to an attosecond pulse for each extremum of the pulse used in the high-order harmonic generation process. The frequency spectrum of such a pulse train has a series of peaks separated by twice the fundamental frequency, usually all of the odd harmonics of the laser field.

We treat the train with two pulses per optical period as a sum of two trains, each with one pulse per optical period. If we assume that the total number of pulses in the train, N, is even then we may write the electric field of the pulse train as

$$\begin{aligned}\vec{\mathcal{E}}_X(t) &= \vec{\mathcal{E}}_{X,0} \sum_{n=0}^{N/2-1} f_X(t-nT)e^{-i(\omega_X t+2n\phi_X)} \\ &\quad +\vec{\mathcal{E}}_{X,0} \sum_{n=0}^{N/2-1} f_X(t-(n+\tfrac{1}{2})T)e^{-i(\omega_X t+(2n+1)\phi_X)}, \quad (7.11)\end{aligned}$$

which is the same field as in Eq. (7.2) for $\kappa = 2$. We calculate the T-matrix elements as a sum of the contributions from each of the two terms in Eq. (7.11). Referring back to Eq. (7.5) we find

$$\begin{aligned} T_{fi}(t_0) &= -i \sum_{n=0}^{N/2-1} e^{-i2n\phi_X} \int dt\, T^{1B}(\vec{k}_f + \vec{A}(t)) f_X(t - t_0 - nT) \\ &\quad \times \exp\left[\frac{i}{2}\int^t dt'(\vec{k}_f + \vec{A}(t'))^2 - iE_i t - i\omega_X(t - t_0)\right] \qquad (7.12) \\ &- i \sum_{n=0}^{N/2-1} e^{-i(2n+1)\phi_X} \int dt\, T^{1B}(\vec{k}_f + \vec{A}(t)) f_X(t - t_0 - (n + \tfrac{1}{2})T) \\ &\quad \times \exp\left[\frac{i}{2}\int^t dt'(\vec{k}_f + \vec{A}(t'))^2 - iE_i t - i\omega_X(t - t_0)\right]. \end{aligned}$$

The first sum is exactly like the expression in the previous section, except $N \to N/2$ and $\phi_X \to 2\phi_X$. This means that we can reuse the findings from there and the first sum gives us

$$\begin{aligned} T^1_{fi}(t_0) &= -ie^{i\Phi(t_0)} T^{1B}(\vec{k}_f + \vec{A}(t_0)) \tilde{f}_X(\tfrac{k_f^2}{2} + \vec{k}_f \cdot \vec{A}(t_0) - \omega_X - E_i) \\ &\times \frac{1 - \exp\left[-i\frac{N}{2}\left(2\phi_X - T(\frac{k_f^2}{2} - E_i - \omega_X)\right)\right]}{1 - \exp\left[-i\left(2\phi_X - T(\frac{k_f^2}{2} - E_i - \omega_X)\right)\right]}. \qquad (7.13) \end{aligned}$$

The second term is a bit different and requires a more detailed treatment. We start with the integral in the phase and note that

$$\int_0^{(n+1/2)T+t_0} dt'(\vec{k}_f + \vec{A}(t'))^2 \qquad (7.14)$$

$$= \int_0^{nT} dt'(\vec{k}_f + \vec{A}(t'))^2 + \int_{t_0}^{t_0+T/2} dt'(\vec{k}_f + \vec{A}(t'))^2$$

$$= (n + \tfrac{1}{2})T\left(k_f^2 + \frac{\mathcal{E}_0^2}{2\omega_L^2}\right) + 2\Phi_2(t_0), \qquad (7.15)$$

where the first part is the same as was found in Eq. (7.6), and we have introduced $\Phi_2 = \int_{t_0}^{t_0+T/2} dt' \vec{k}_f \cdot \vec{A}(t_0)$. With this observation, we can calculate the second part of the transition matrix element the same way

as was done in the previous section. We neglect the part of the phase that is second order in the vector potential and perform the substitution $t \to t - t_0 - (n + 1/2)T$

$$\begin{aligned}
T^2_{fi}(t_0) &= -i \sum_{n=0}^{N/2-1} e^{-i(2n+1)\phi_X} \int dt\, T^{1B}(\vec{k}_f + \vec{A}(t + t_0 + T/2)) f_X(t) \\
&\quad \times \exp\left[\frac{i}{2} \int^{t+t_0+(n+1/2)T} dt' (\vec{k}_f + \vec{A}(t'))^2\right] \\
&\quad \times \exp\left[-iE_i(t + t_0 + (n + 1/2)T) - i\omega_X(t + (n + 1/2)T)\right]. \\
&= -i \sum_{n=0}^{N/2-1} e^{-i(2n+1)\phi_X + i(n+1/2)T(k_f^2/2 - E_i - \omega_X)} e^{i\Phi(t_0) + i\Phi_2(t_0)} \\
&\quad \times \int dt\, T^{1B}(\vec{k}_f - \vec{A}(t + t_0)) f_X(t) \\
&\quad \times \exp\left[i\tfrac{k_f^2}{2}t - i\vec{k}_f \cdot \vec{A}(t_0)t - iE_i t - i\omega_X t\right]. \qquad (7.16)
\end{aligned}$$

We have used that $\vec{A}(t)$ is sinusoidal, such that $\vec{A}(t + T/2) = -\vec{A}(t)$ to simplify the expressions. If we again assume that the variation in the first Born matrix element is small, then we can perform the integral analytically and we obtain

$$\begin{aligned}
T^2_{fi}(t_0) &= -ie^{i\phi(t_0) + i\Phi_2(t_0)} T^{1B}(\vec{k}_f - \vec{A}(t_0)) \tilde{f}_X(\tfrac{k_f^2}{2} - \vec{k}_f \cdot \vec{A}(t_0) - \omega_X - E_i) \\
&\quad \times \sum_{n=0}^{N/2-1} e^{-i(2n+1)(\phi_X - \frac{T}{2}(\frac{k_f^2}{2} - E_i - \omega_X))} \qquad (7.17)
\end{aligned}$$

The sum is again the geometric series and can be evaluated in closed form to give us the final expression

$$\begin{aligned}
T^2_{fi}(t_0) &= -ie^{i\phi(t_0) + i\Phi_2(t_0)} T^{1B}(\vec{k}_f - \vec{A}(t_0)) \tilde{f}_X(\tfrac{k_f^2}{2} - \vec{k}_f \cdot \vec{A}(t_0) - \omega_X - E_i) \\
&\quad \times e^{-i(\phi_X - \frac{T}{2}(\frac{k_f^2}{2} - E_i - \omega_X))} \frac{\exp\left[-i\frac{N}{2}(2\phi_X - T(\frac{k_f^2}{2} - E_i - \omega_X))\right]}{\exp\left[-i(2\phi_X - T(\frac{k_f^2}{2} - E_i - \omega_X))\right]}. \qquad (7.18)
\end{aligned}$$

This expression is to be compared to Eq. (7.13). First we note the many similarities. The last fraction is identical for the two. It shows

that the spectrum for the two pulses per laser period is again a series of lines, separated by the fundamental photon frequency. The fact that two attosecond pulses per optical cycle corresponds to only every second of the harmonics is not seen until we add the two terms and look at the relative phase between the contributions

$$\begin{aligned} T_{fi}(t_0) &= -ie^{i\Phi(t_0)}\frac{\exp\left[-i\frac{N}{2}(2\phi_X - T(\frac{k_f^2}{2} - E_i - \omega_X))\right]}{\exp\left[-i(2\phi_X - T(\frac{k_f^2}{2} - E_i - \omega_X))\right]} \\ &\quad \times\Big[T^{1B}(\vec{k}_f + \vec{A}(t_0))\tilde{f}_X(\tfrac{k_f^2}{2} + \vec{k}_f\cdot\vec{A}(t_0) - \omega_X - E_i) \\ &\quad + e^{i\Phi_2(t_0)}e^{-i(\phi_X - \frac{T}{2}(\frac{k_f^2}{2} - E_i - \omega_X))} \\ &\quad \times T^{1B}(\vec{k}_f - \vec{A}(t_0))\tilde{f}_X(\tfrac{k_f^2}{2} - \vec{k}_f\cdot\vec{A}(t_0) - \omega_X - E_i)\Big] \end{aligned} \tag{7.19}$$

This is the final expression for the transition matrix element for a pulse train with two attosecond pulses per laser period. The fraction in front of the expression has maxima whenever

$$(2\phi_X - T(\tfrac{k_f^2}{2} - E_i - \omega_X)) = 2\pi k, \qquad k \text{ integer.} \tag{7.20}$$

This is the same condition as for the case with only one cycle per optical period, meaning that the fraction is non-zero at each of the harmonics, both odd and even. The difference is in the final term. In the limit $A(t) \to 0$ when there is no laser field on, we find that the two terms exactly cancel for every second of the maxima. The surviving peaks are separated by twice the laser frequency, but whether it is the odd harmonics is determined by the relative phase between the attosecond pulses, ϕ_X. We will refer to the field-free peaks as the odd harmonics and those that vanish for $A(t) \to 0$ as the even harmonics.

Examples of calculated photoelectron spectra are shown in Fig. 7.2. The spectra are to be compared with those presented in Fig. 7.1. The top two spectra are for a weak laser field corresponding to an intensity of 2×10^{10} W/cm^2, while the bottom spectra are for the same field strength as in Fig. 7.1, corresponding to 2×10^{11} W/cm^2.

For only two pulses in the train we see that the train characteristics are not yet clear. There is neither a clear oscillatory signal as in the

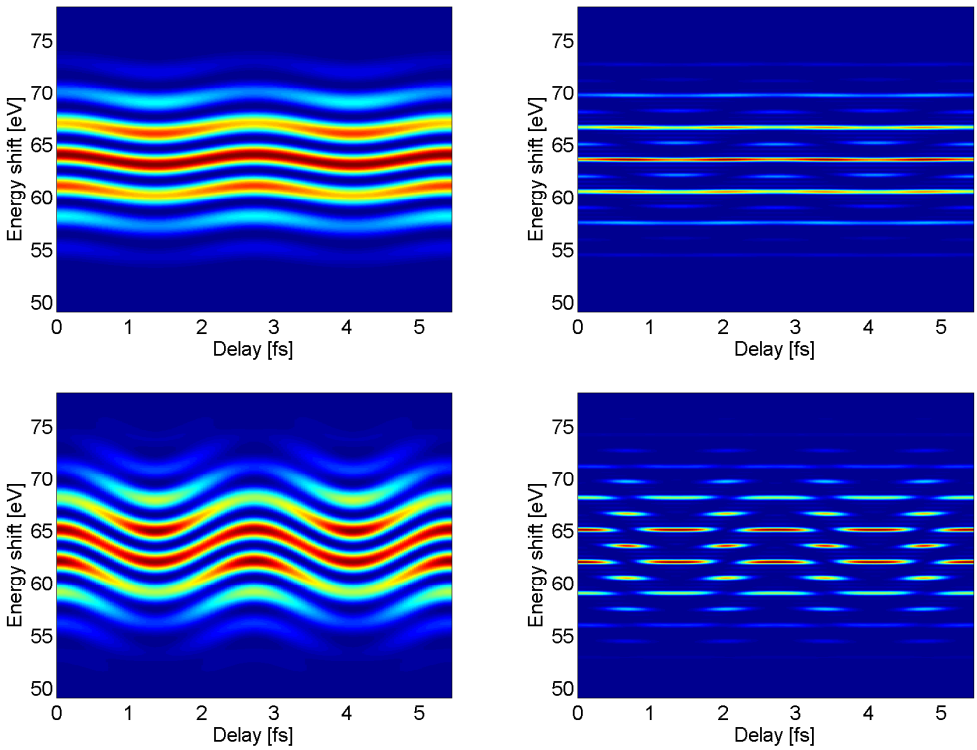

Figure 7.2 | Photoelectron emission spectra for 2 attosecond pulses per optical cycle of the laser field. The two figures in the top are for laser intensity, $I = 2 \times 10^{10}\mathrm{W/cm}^2$, while the two bottom figures are for $I = 2 \times 10^{11}\mathrm{W/cm}^2$. The two figures to the left are for $N = 2$ pulses in the pulse train, while the two figures to the right are for $N = 8$.

one-pulse case, nor clear odd and even harmonics. For 8 pulses and the weak field (top right figure) we clearly see that half of the lines are quite strong and the other half is a lot weaker and the strength oscillates as a function of the delay. For a stronger field, the whole thing becomes a lot more messy. The signal is still periodic with the periodicity of twice the laser field, but the odd and even harmonics are of comparable strength.

7.4 Strength of the Even Harmonics

We now look at a scenario for time-resolved measurements and for pulse train characterisation, known as Reconstruction of Attosecond Beating By Interference of Two-photon Transitions (RABBITT)[18, 21]. We calculate the strength of the even harmonics and show that this will

oscillate with the relative phase between the attosecond pulse train and the fundamental laser field. When the delay between the pulse train and the laser field is varied, these oscillations may be used for time-resolved measurements similar to the streaking signal.

The even harmonics satisfy that

$$e^{-i(\phi_X - \frac{T}{2}(\frac{k_f^2}{2} - E_i - \omega_X))} = -1, \tag{7.21}$$

such that the two terms in the square parenthesis in Eq. (7.19) cancel for vanishing laser field. The typical fields used in the RABBITT experiments are weaker than what is used in streaking experiments, typically $10^{10} - 10^{11}$ W/cm^2. We can write the intensity ratio of the even harmonic to the neighbouring odd harmonics, $|S|^2$ as

$$S = \frac{1 - e^{i\Phi_2(t_0) + i\Theta(t_0)}}{1 + e^{i\Phi_2(t_0) + i\Theta(t_0)}} \approx \frac{1 - e^{i\Phi_2(t_0) + i\Theta(t_0)}}{2}, \tag{7.22}$$

where we have introduced

$$\frac{T^{1B}(\vec{k}_f - \vec{A}(t_0))\tilde{f}_X(\frac{k_f^2}{2} - \vec{k}_f \cdot \vec{A}(t_0) - \omega_X - E_i)}{T^{1B}(\vec{k}_f + \vec{A}(t_0))\tilde{f}_X(\frac{k_f^2}{2} + \vec{k}_f \cdot \vec{A}(t_0) - \omega_X - E_i)} \approx e^{i(\Theta_A(t_0) + \Theta_H(t_0))} = e^{i\Theta(t_0)}. \tag{7.23}$$

Θ_A is the part originating from the ratio of the first Born matrix elements and is related to the atomic structure, while Θ_H is the part originating from the attosecond pulses and is related to the pulse train. If there is an energy dependent phase of the first Born matrix element, then the energy-derivative of this phase is associated with the Wigner time-delay as discussed in Sec. 5.2. Similarly, if there is an energy dependent phase in the Fourier transform of the attosecond pulses, $\tilde{f}_X$, this will give rise to a similar temporal delay as we shall see now. We look at the strength of the even harmonic and assume that both $\Phi_2(t_0)$ and $\Theta(t_0)$ are small, since the laser field is weak. We find

$$S \approx \frac{-i(\Phi_2(t_0) + \Theta(t_0))}{2}, \tag{7.24}$$

where

$$\Phi_2(t_0) = \int_{t_0}^{t_0 + T/2} dt' \, \vec{k}_f \cdot \vec{A}(t_0) = -2\frac{\vec{k}_f \cdot \vec{\mathcal{E}}_0}{\omega_L^2} \sin(\omega_L t_0 + \phi). \tag{7.25}$$

If we assume that the phase of the first Born matrix element varies linearly with energy, like in Sec. 5.2, we find

$$e^{i\Theta_A(t_0)} = \exp\left[i\alpha\frac{(\vec{k}_f - \vec{A}(t_0))^2}{2} - i\alpha\frac{(\vec{k}_f + \vec{A}(t_0))^2}{2}\right] = e^{-i2\alpha\vec{k}_f\cdot\vec{A}(t_0)} \tag{7.26}$$

or

$$\Theta_A(t_0) = -2\alpha\vec{k}_f \cdot \vec{A}(t_0) = \frac{2\alpha\vec{k}_f \cdot \vec{\mathcal{E}}_0}{\omega_L}\cos(\omega_L t_0 + \phi). \tag{7.27}$$

Similarly, if the phase of the attosecond pulse varies linearly with the frequency, we find that

$$\Theta_H(t_0) = -2\beta\vec{k}_f \cdot \vec{A}(t_0) = \frac{2\beta\vec{k}_f \cdot \vec{\mathcal{E}}_0}{\omega_L}\cos(\omega_L t_0 + \phi). \tag{7.28}$$

Adding these contributions we find that the oscillations in the strength of the even harmonics will follow

$$\begin{aligned} S &= -2\frac{\vec{k}_f \cdot \vec{\mathcal{E}}_0}{\omega_L^2}\left(\sin(\omega_L t_0 + \phi) + \omega_L(\alpha+\beta)\cos(\omega_L t_0 + \phi)\right) \\ &\propto \sin(\omega_L t_0 + \phi + \Delta_A + \Delta_H), \end{aligned} \tag{7.29}$$

where $\Delta_A = \arctan(\omega_L\alpha)/\omega_L$ and $\Delta_H = \arctan(\omega_L\beta)/\omega_L$. Eq. (7.29) is the main result of this section. The strength of the even harmonics, $|S|^2$, oscillates with the angular frequency $2\omega_L$ and a phase determined by the phase of the laser field and the sum of the atomic and harmonic phase, Δ_A and Δ_H. In this strong-field model, the atomic phase is essentially the Wigner time delay, which was also discussed in the context of streaking experiments in Sec. 5.2.

If we use the same pulse train to ionise from two different initial states, then the harmonic phase is the same for the two different sets of emitted electrons. In this way we are able to measure the Wigner time-delay directly. This was done in Ref. [9], where the delay between electrons emitted from the 3s and 3p shells in atomic argon was measured. In that work, shifts on the order of tens to a hundred asec was found, with the emission delay being measured at different energies through the use of different even sidebands. The delays were explained through a combination of Wigner time-delay and the Coulomb-laser coupling

mehcanism, which was also discussed earlier, in Sec. 5.3. Time-resolved measurements using the RABBITT technique, similar to the streaking technique, measures the phase of the laser field mapped onto the electron distribution. These phase measurements are sensitive to quite a lot of subtle effects and the RABBITT measurements are equally sensitive to polarisation effects and Coulomb-laser coupling effects as the streaking measurements are.

7.5 Frequency-Domain Approach to RABBITT

It is worth noting that a lot of work have been done on the RABBITT scheme and that most has been done in the frequency-domain, with quite a different approach from what was presented in the previous sections. In the frequency-domain, the attosecond pulse train is described by a series of odd harmonics from the fundamental laser field. A final state with energy corresponding to one of the even harmonics can be reached either through absorption of the lower harmonic and a photon from the laser field or through absorption of the higher harmonic and emission of a photon into the laser field. This is shown in Fig. 7.3.

In a photon picture the intensity in the even $2n\omega_L$ band is related to the harmonic phase of the harmonic components $(2n-1)\omega_L$ and $(2n+1)\omega_L$. The atomic phase is similarly related to the ionisation matrix elements describing the continuum at these harmonic components[18, 55]. This is in contrast to what was seen in the previous section, where the atomic and harmonic phase were related to the structure of the continuum and the Fourier transform of the attosecond pulses near the final state, $2n\omega_L$, only. It is clear that the harmonic phase can be compensated for when performing time-resolved measurements, when photoelectrons from two different channels are ionised by the same train of attosecond pulses. The harmonic phase introduced in both measurements using the same pulse train is identical and has no influence on the phase-difference, which is thus related to the atomic phase.

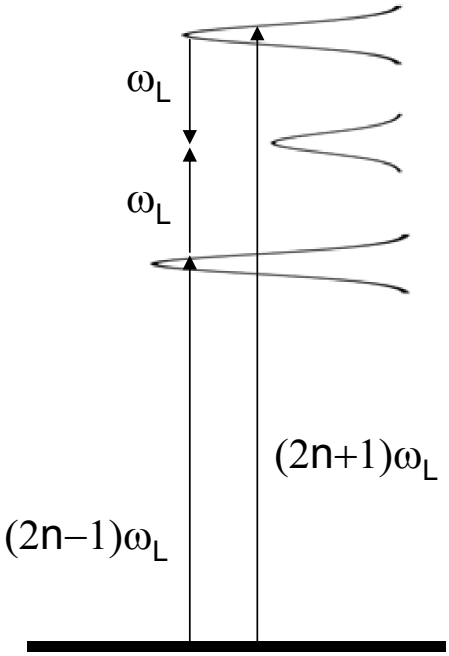

Figure 7.3 | Schematic representation of the two different pathways leading to the final state with energy corresponding the even harmonic, $2n\omega_L$.

Chapter

8 Laser Assisted Photoelectric Effect

In the previous sections we have shown how a combination of an attosecond pulse and a laser field may be used for time-resolved measurements. In streaking experiments the key is to use an attosecond pulse which is shorter than the optical period of the laser field, in order to release all of the electrons at the same phase of the laser field and give the electrons a characteristic momentum kick. In this chapter we will discuss how longer XUV pulses in combination with an assisting laser field can be used for time-resolved measurements[23, 32, 33, 57]. When using long pulses, the signal is not a mapping of the phase of the laser pulse, but only the envelope. This means that the temporal resolution is determined by the laser envelope and is thus not as good as for streaking. On the other hand, the laser assisted photoelectric effect (LAPE) technique is not sensitive to phase effects.

8.1 Modelling the Laser Assisted Photoelectric Effect

The electric field is given by

$$\vec{\mathcal{E}}(t) = \vec{\mathcal{E}}_0(t)\sin(\omega_L t + \phi) \tag{8.1}$$

and we assume that the duration of the pulse is long, such that the variation of the envelope is very slow compared to the oscillations of the carrier wave. We can then calculate the phase in the Volkov wave function in Eq. (2.5) analytically. We neglect the terms of the order $\mathcal{E}_0^2$ and find

$$\Psi_f(\vec{r},t) = \frac{1}{(2\pi)^{3/2}} \exp\left[i(\vec{k}_f + \vec{A}(t)) \cdot \vec{r} - i\frac{k_f^2}{2} - i\frac{\vec{k}_f \cdot \vec{\mathcal{E}}_0(t)}{\omega_L^2} \sin(\omega_L t + \phi) \right]. \tag{8.2}$$

Functions of the type $e^{z\sin(x)}$ can be expanded in terms of Bessel functions of integer order[58] and we find

$$e^{-i\frac{\vec{k}_f \cdot \vec{\mathcal{E}}_0(t)}{\omega_L^2}\sin(\omega_L t+\phi)} = \sum_{n=-\infty}^{\infty} e^{-in(\omega_L t+\phi)} J_n\left(\frac{\vec{k}_f \cdot \vec{\mathcal{E}}_0(t)}{\omega_L^2}\right). \tag{8.3}$$

This expansion allows us to calculate the transition amplitude for ionisation by an XUV pulse in the presence of an assisting laser field, when the duration of the XUV pulse is longer than the optical period of the assisting laser field. We calculate the transition matrix element as

$$\begin{aligned} T_{fi}(t_0) &\approx -i \int dt \langle \Psi_f(\vec{r},t) | V_X(\vec{r}, t-t_0) | \Psi_i(\vec{r},t) \rangle \\ &= -i \sum_{n=-\infty}^{\infty} \int dt\, T^{1B}(\vec{k}_f + \vec{A}(t)) f_X(t-t_0) J_n\left(\frac{\vec{k}_f \cdot \vec{\mathcal{E}}_0(t)}{\omega_L^2}\right) \\ &\quad \times \exp\left[i\frac{k_f^2}{2} + in(\omega_L t + \phi) - iE_i t - i\omega_X (t-t_0) \right]. \end{aligned} \tag{8.4}$$

If the vector potential is small compared to the final state momentum, $k_f \gg A(t)$, then we can neglect the vector potential dependence in the first Born matrix element. If we furthermore assume that the change in the laser envelope is negligible over the duration of the XUV pulse, then the time integral in Eq. (8.4) is just the Fourier transform of the XUV pulse.

$$T_{fi} = -iT^{1B}(\vec{k}_f) \sum_{n=-\infty}^{\infty} e^{i\Phi_n(t_0)} J_n\left(\frac{\vec{k}_f \cdot \vec{\mathcal{E}}_0(t_0)}{\omega_L^2}\right) \tilde{f}_X(\tfrac{k_f^2}{2} + n\omega_L - E_i - \omega_X), \tag{8.5}$$

where $\Phi_n(t_0) = \frac{k_f^2}{2}t_0 + n(\omega_L t_0 + \phi) - E_i t_0$ is a phase which is unimportant for long, spectrally narrow XUV pulses, where the different peaks do not interfere. If the duration of the XUV pulse is longer than the optical period of the assisting laser field, then the spectral width of the pulse may be less than the laser frequency. In that case, the spectrum from Eq. (8.5) gives a series of peaks in the energy spectrum of the electrons, centred around

$$E_f = \frac{k_f^2}{2} = \omega_X + E_i - n\omega_L \tag{8.6}$$

and the relative strength of the peaks is

$$J_n^2\left(\frac{\vec{k}_f \cdot \vec{\mathcal{E}}_0(t_0)}{\omega_L^2}\right), \tag{8.7}$$

where n runs through all the integers[59]. For small arguments, x, the Bessel functions satisfy that $J_n(x) \approx (x/2)^n/\Gamma(n+1)$[58]. In this case only a few terms $n = 0, \pm 1, \pm 2$ are important in the expansion.

The result is approximately true as long as the envelope of the laser pulse does not vary significantly over an optical period of the laser field or over the duration of the XUV pulse. The criterion for the validity of the approximation that the sidebands depend only on the envelope of the laser field is that the duration of the laser pulse is long compared to both the optical period and the duration of the XUV pulse, $\tau_L \gg 2\pi/\omega_L, \tau_X$. The magnitude of the first sidebands $n = \pm 1$ is then given by

$$P_1 = J_1^2\left(\frac{\vec{k}_f \cdot \vec{\mathcal{E}}_0(t_0)}{\omega_L^2}\right) \approx \left(\frac{\vec{k}_f \cdot \vec{\mathcal{E}}_0(t_0)}{2\omega_L^2}\right)^2. \tag{8.8}$$

For weak laser pulses this is the only significant band. Eq. (8.8) shows that the intensity of the sideband is proportinal to the instantaneous intensity of the laser pulse at the time of ionisation.

8.2 LAPE for Time-Resolved Measurements

As is seen from Eq. (8.8), the intensity of the first sideband is an indication of the time that the electron was released into the continuum,

similarly to the streaking spectra used in the previous chapters for time-resolved measurements. If an electron is liberated with a delay, Δt, the magnitude of the sideband should instead follow $\vec{\mathcal{E}}_0(t_0+\Delta t)$. If we have two different ionisation channels, the sidebands from the two channels would be shifted in time, if there is a delay in one of the channels[23]. For pulses of finite length, the accurate retrieval is not as simple, as the signal is a convolution of the XUV and the laser pulse[23, 57], but still, the delay can be measured directly in the time-domain.

In Fig. 8.1 we present an example of the photoelectron spectrum. The laser pulse is centred around 800 nm wavelength and is 10 optical periods or 25 fs FWHM. The intensity is 3.2×10^{10} W/cm^2. The XUV pulse is centred around 91 eV and has a duration corresponding to 2 optical periods of the laser field. The binding energy of the initial state is 13.6 eV. The photoelectron spectrum is plotted on a logarithmic scale to enhance the rather weak first and second sidebands. To better use the colour scale, everything below 10^{-10} has been given the same colour. The spectrum is calculated by numerical integration of Eq. (8.4), without assuming that the laser pulse is much longer than the XUV pulse.

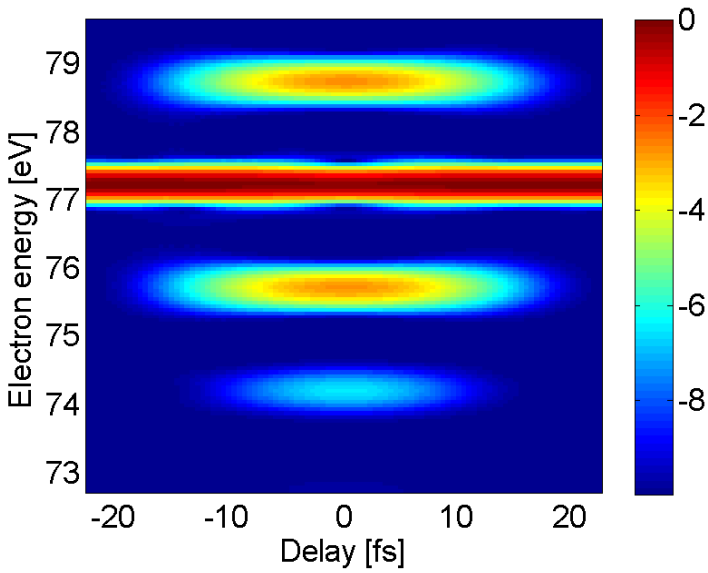

Figure 8.1 | Photoelectron spectrum in the LAPE regime. The laser intensity is 3.2×10^{10} W/cm^2 and the pulse durations are 25 fs FWHM for the laser pulse and 5 fs for the XUV pulse.

Fig. 8.2 is a vertical intersect through Fig. 8.1 for $t_0 = 0$, presented on a linear scale. The height of the first sideband is only 7% of the height of the central peak, but the total area under the sideband peak is 9% of the total volume. This is because even the 10 cycle laser pulse is short enough to introduce some broadening in the sidebands, such that these are wider than the central peak. The ratio of the area under the peaks is to be compared with the result found in Eq. (8.8). The estimate found from the Bessel function in Eq. (8.8) is 11% and the first order approximation to the Bessel function also shown in Eq. (8.8) gives 13%. This shows that the long pulse limit is not a good approximation and that the Taylor expansion is not accurate, even for the relatively weak laser pulse considered here.

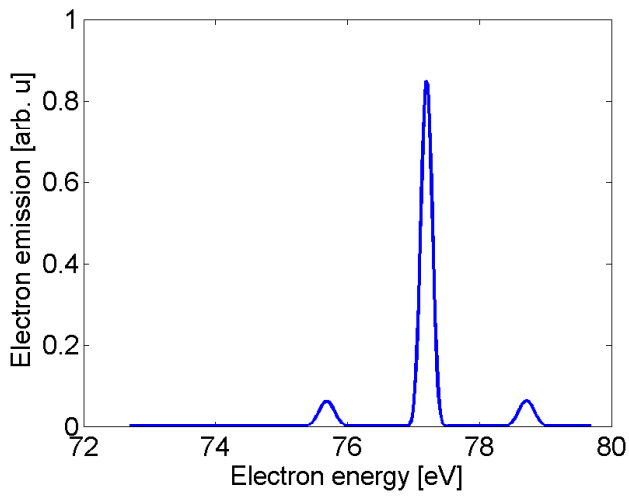

Figure 8.2 | Photoelectron distribution at $t_0 = 0$ when the overlap between the XUV and the laser pulse is maximal. The height of the first sideband is only 7%.

LAPE has recently been demonstrated from metal surfaces[60, 61] and the LAPE technique has also been used to measure the Auger lifetime of xenon atoms adsorbed onto a platinum surface[23, 57]. The lifetime was found to be 7 ± 1 fs in good agreement with results for free atoms. In the experiment, a laser pulse with a duration of 35 fs in combination with an XUV pulse of undetermined duration on the order 6 fs was used to get the required temporal resolution. In order to get even better temporal resolution and be able to resolve delays on the order 1 fs, it may be necessary to push the duration of the pulses down to a few

optical periods. We have calculated the photoelectron spectrum from the conduction band in a metal using the jellium model presented in Sec. 3.2, for a short laser pulse with only 3 optical cycles and an XUV pulse with a duration of only 1 laser optical cycle. The result is shown in Fig. 8.3.

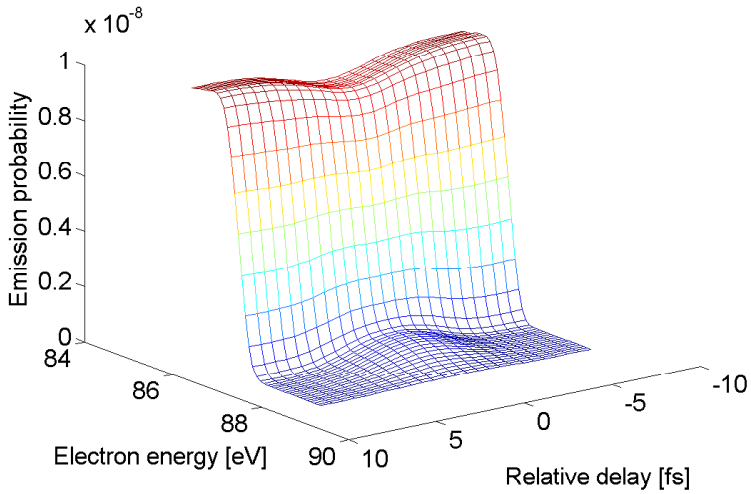

Figure 8.3 | Electron emission from a jellium surface for a laser pulse with a central wavelength of 800 nm and a peak intensity of 3.2×10^{10} W/cm^2 and an XUV pulse with a central photon energy of 90 eV. The first sideband can be seen as the shoulder to the contribution from the main peak. The laser pulse length is 3 optical cycles and the duration of the XUV pulse equals a single laser optical cycle.

To see how far one can push the temporal resolution, we have calculated the magnitude of the first sideband to the main peak for different laser pulse durations. The result is shown in Fig. 8.4.

The sidebands form even for very short laser pulses, showing that the technique can be pushed quite far with respect to the temporal resolution. The sidebands are almost fully developed for pulse durations longer than 10 optical cycles. When there is a competition between having a measurable sideband for signal and a short pulse duration for temporal resolution, it is advantageous to move to pulse lengths of 10 optical cycles or even shorter. As can be seen from Eq. (8.8), it may also be advantageous to move to longer wavelengths, because the strength of the signal scales approximately as λ^4. This enhancement has been observed experimentally[62], but comes with the cost that longer wave-

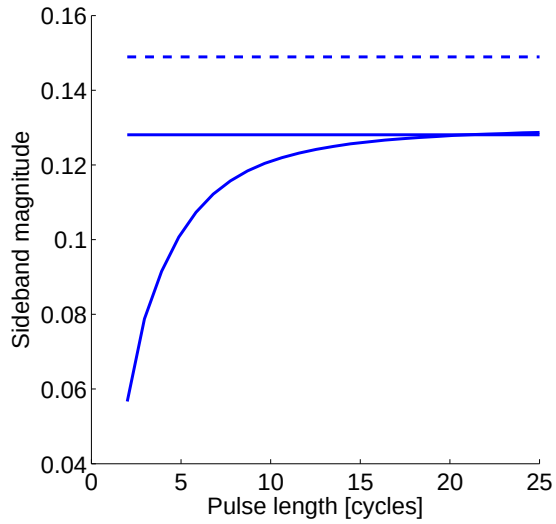

Figure 8.4 | Magnitude of the first sideband compared to the laser-field-free photopeak as a function of the duration of the laser pulse in optical cycles. The laser is centered around 800 nm and has a peak intensity of 3.2×10^{10} W/cm^2. The full increasing curve is a result of a fully time-dependent calculation within the jellium model. The two horizontal lines are the long pulse limits, given by Eq. (8.8), the full being the Bessel function and the dashed line the Taylor expansion.

lengths leads to longer laser pulses and hence worse temporal resolution. Another work has shown that the sidebands from a Bloch-like surface state (similar to what was studied in Sec. 3.3) are enhanced[57], making the laser-assisted photoelectric effect more attractive when working with surfaces, because a lower intensity is needed and fewer ATI electrons are released.

Chapter

9 Attosecond Absorption Spectroscopy

In absorption spectroscopy the measured signal is the back-action of the target system onto the electromagnetic field. Very recently, experiments have been performed where the signal is the frequency resolved absorption of the attosecond pulse[12–14] rather than the ion production or the photoelectron distribution. In this chapter we will set up a time-domain formulation of the absorption. Though one has to be very careful when discussing time and frequency simultaneously, we discuss how frequency-resolved absorption spectroscopy can be used to make time-resolved measurements even on the attosecond time scale.

9.1 Time-Domain Theory for Absorption Spectroscopy

Ideally, calculating the back-action of the target onto the electromagnetic field requires a full quantum mechanical treatment of the target as well as the electromagnetic field. Since this is a formidable task, we settle for a semi-classical model, where we solve the classical Maxwell wave equation approximately for the electromagnetic field while treating the target quantum mechanically. This procedure allows us to obtain an expression for the time- and position-dependent electromagnetic field,

which is related to the measured absorption spectrum in a simple manner (see Eq. (9.5) below).

The Maxwell wave equation for the electric field, $\vec{\mathcal{E}}$, reads

$$\left(\nabla^2 - \frac{1}{c^2}\frac{\partial^2}{\partial t^2}\right)\vec{\mathcal{E}}(\vec{r},t) = \frac{4\pi}{c^2}\frac{\partial^2}{\partial t^2}\vec{P}(\vec{r},t), \tag{9.1}$$

where c is the speed of light and $\vec{P}(\vec{r},t)$ is the induced polarisation in the target. In atomic units, we use $c = \alpha^{-1} \approx 137$ for the speed of light in Eq. (9.1) instead of the fine structure constant.

To allow for an analytical solution, we impose a series of approximations. First we assume that the electric field is a pulse propagating in the x-direction and that it is sufficiently wide in the transverse directions to neglect the $\frac{\partial^2}{\partial y^2}$ and $\frac{\partial^2}{\partial z^2}$ terms. A more restrictive approximation is that the target is very thin, such that we may neglect any propagation or phase-matching effects by treating the target as a point potential. With these approximations, the Maxwell equation reduces to

$$\left(\frac{\partial^2}{\partial x^2} - \frac{1}{c^2}\frac{\partial^2}{\partial t^2}\right)\vec{\mathcal{E}}(x,t) = \frac{4\pi}{c^2}\frac{\partial^2}{\partial t^2}\vec{P}(t)\delta(x), \tag{9.2}$$

where $\delta(x)$ is a Dirac delta function. If we assume that the incoming field is a pulse propagating in the positive x-direction and split the electric field into the incoming and the generated fields, the solution to this equation is

$$\vec{\mathcal{E}}(x,t) = \vec{\mathcal{E}}_{\text{in}}\left(t - \frac{x}{c}\right) + \vec{\mathcal{E}}_{\text{gen}}(x,t), \tag{9.3}$$

where

$$\vec{\mathcal{E}}_{\text{gen}}(x,t) = -\frac{2\pi}{c}\left[\Theta(x)\frac{\partial}{\partial t}\vec{P}\left(t - \frac{x}{c}\right) + \Theta(-x)\frac{\partial}{\partial t}\vec{P}\left(t + \frac{x}{c}\right)\right] \tag{9.4}$$

as can be seen by insertion. Here $\Theta(x)$ is the Heaviside step function, which is 1 for $x > 0$ and 0 elsewhere.

The signal in the absorption experiment is the frequency-resolved electromagnetic field at a given position, $x > 0$, after the pulse has passed through the target. The spectrum of interest may be expressed as

$$S(\omega) \propto \left|\int dt\, e^{i\omega t}\vec{\mathcal{E}}(x,t)\right|^2. \tag{9.5}$$

If we introduce the expression from Eq. (9.3) into this expression for the signal, we find three terms

$$S(\omega) \propto \left|\vec{\mathcal{E}}_{\text{in}}(\omega)\right|^2 + 2\text{Re}\left(\vec{\mathcal{E}}^*_{\text{in}}(\omega)\cdot\vec{\mathcal{E}}_{\text{gen}}(\omega)\right) + \left|\vec{\mathcal{E}}_{\text{gen}}(\omega)\right|^2, \tag{9.6}$$

where the Fourier transform of the incoming field is given by

$$\vec{\mathcal{E}}_{\text{in}}(\omega) = \int dt\, e^{i\omega t}\vec{\mathcal{E}}_{\text{in}}(t). \tag{9.7}$$

The Fourier transform of the generated field due to the induced polarisation is given by

$$\vec{\mathcal{E}}_{\text{gen}}(\omega) = -\frac{2\pi}{c}\int dt\, e^{i\omega t}\frac{\partial}{\partial t}\vec{P}(t) \tag{9.8}$$

$$= \frac{2\pi\omega i}{c}\int dt\, e^{i\omega t}\vec{P}(t). \tag{9.9}$$

Here we assume that the polarisation vanishes for $t \to \pm\infty$ due to relaxation and use the fact that the integration over all times allows us to make a coordinate transformation and eliminate the x dependence.

From the above equations we see that what is left in order to determine the spectrum is to find a way of calculating the polarisation, $\vec{P}(t)$. For a gas of atomic or molecular targets, the polarisation may be written as

$$\vec{P}(t) = nl\langle\vec{D}(t)\rangle, \tag{9.10}$$

where n is the density of the target, l is the length and $\langle\vec{D}(t)\rangle$ is the expectation value of the atomic or molecular dipole moment. We calculate the expectation value of the dipole moment from a quantum mechanical model describing the interaction of the incoming laser pulses with the target, assuming that the generated electric field is too weak to influece the induced dipole moment.

In this formulation it is clear that the signal in short-pulse, e.g., attosecond absorption spectroscopy does not only originate from the times when the incoming electric field is non-vanishing. The integration over time, needed for the frequency-resolved signal, will pick up contributions over the entire lifetime of the polarisation signal. For attosecond spectroscopy this latter lifetime will typically be determined by system-dependent relaxation processes such as radiative or Auger decay and

will often be much longer than the duration of the pulses involved. The long temporal integration time is the reason why it is possible, also in attosecond absorption spectroscopy, to obtain a frequency-resolution much better than the Fourier limit related to the duration of the pulse.

Here we formulate the problem in the time-domain as opposed to the more standard treatment in the frequency-domain [63–65]. The formulation in the time-domain is natural for studying many dynamical problems. The typical experimental setup is a pump – probe scenario with two laser pulses. The present formulation readily describes situations where the pump and the probe pulse overlap in time or when the probe pulse preceeds the pump pulse as was the case in Ref. [13].

9.2 Atomic Response

We need to calculate the expectation value of the time-dependent dipole moment

$$\langle \vec{D}(t) \rangle = \langle \Psi(t) | \sum_{i=1}^{N} \vec{r}_i | \Psi(t) \rangle, \tag{9.11}$$

where we have neglected any nuclear contribution. We consider the Hamiltonian

$$H = H_0 + V_1(t) + V_2(t - t_0), \tag{9.12}$$

where H_0 denotes the field-free Hamiltonian, V_1 the interaction with the pump pulse, and V_2 the interaction with the probe pulse. The laser-atom interaction is in the length-gauge dipole approximation, $V_i(t) = D_z \mathcal{E}_i(t)$ $(i = 1, 2)$, and $D_z = \sum_{i=1}^{N} z_i$ is the dipole operator. We stress the fact, that the probe pulse described by V_2 arrives with a variable delay, t_0, relative to the pump pulse.

The many-body wave function is expressed in an essential state expansion

$$\begin{aligned} |\Psi(t)\rangle &= c_0(t)|0\rangle + \sum_{a,r} c_a^r(t) e^{-i(E_r - E_a)t} |a^{-1}, r\rangle \\ &\quad + \sum_{b,s} c_b^s(t) e^{-i(E_s - E_b)t} |b^{-1}, s\rangle, \end{aligned} \tag{9.13}$$

where $|0\rangle = |\{abc...n\}\rangle$ denotes the Slater determinant of orbitals for the ground state of the neutral atom. The sum over a runs through all

of the states accessible by single photon ionisation from the first (pump) pulse. The sum over r or s runs through all of the accessible continuum states and the sum over b runs through all of the core states that are accessible by the second (probe) pulse promoting an electron into one of the hole states. In Eq. (9.13) we have suppressed the integral over the continua associated with r, s for notational convenience. The state $|a^{-1}, r\rangle$ denotes that in which an electron from one orbital a has been removed and excited to orbital r. Similar for the state $|b^{-1}, s\rangle$.

We first consider the experiment described in Refs. [12, 65]. An intense laser pulse is used to remove a valence electron from atomic krypton. The 4p valence electrons are split into two fine-structure levels $4p_{1/2}$ and $4p_{3/2}$ separated by 0.7 eV, and the hole is created in a superposition of the two states. After the intense laser pulse is over an attosecond pulse is sent onto the krypton ions. The attosecond pulse can promote an electron from the 3d core states to the 4p hole. The energy diagram is shown in Fig. 9.1.

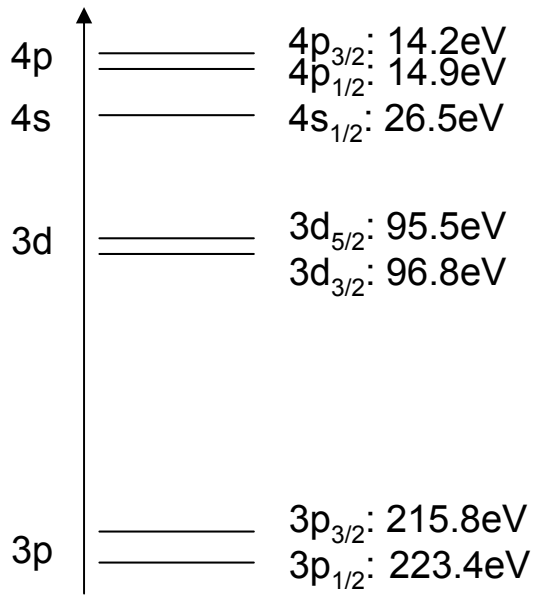

Figure 9.1 | Binding energies for the least bound states in atomic krypton (Z=36). The binding energies are calculated in a Dirac-Fock framework by Eva Lindroth.

In the essential state expansion, Eq. (9.13), the sum over a runs through the 4p states, and the sum over b runs through the 3d states.

If we consider only $t_0 > \tau_1$, where τ_1 is the duration of the laser pulse and we treat the interaction with the attosecond pulse in first-order perturbation theory, then $c_a^r(t) = c_a^r$ is constant in time. We determine the coefficients for the core hole states as

$$c_b^s(t) = -i \sum_{a,r} c_a^r \int^t dt' \, \mathcal{E}_2(t' - t_0) e^{i(E_s - E_r + E_a - E_b)t'} \langle b^{-1}, s | D_z | a^{-1}, r \rangle. \tag{9.14}$$

Since $D_z = \sum_{i=1}^N z_i$ is a sum of single-particle operators, the Slater-Condon rules allows us to reduce the many-body matrix elements to single-electron integrals, $\langle b^{-1}, s | D_z | a^{-1}, r \rangle = \langle a | z | b \rangle \delta_{r,s}$, where we have used that a sum of single-particle operators may change the state of only one electron[66]. Introducing the Slater-Condon rules in Eq. (9.14) we arrive at

$$\begin{aligned} c_b^s(t) &= -i \sum_a c_a^s \langle a | z | b \rangle \int^t dt' \, \mathcal{E}_2(t' - t_0) e^{i(E_a - E_b)t'} \qquad (9.15) \\ &= -i \sum_a c_a^s \langle a | z | b \rangle \mathcal{E}_{0,2} e^{i(E_a - E_b)t_0} \tilde{f}_2(E_a - E_b - \omega_X) \qquad t > t_0. \end{aligned}$$

In the final result we have assumed that the attosecond pulse is much faster than any other time scale involved and that we can perform the integral over all of the pulse for $t > t_0$. For $t < t_0$ there is no population in the core states and $c_b^s(t) = 0$. Turning to the time-dependent dipole moment, we find

$$\begin{aligned} \langle D_z(t) \rangle &= \sum_{a,b,r} c_b^r(t)^* c_a^r(t) e^{i(E_a - E_b)t} \langle a | z | b \rangle + c.c. \qquad (9.16) \\ &= -i \mathcal{E}_{0,2} \sum_{a,a',b,r} e^{-i(E_a - E_b)t} c_{a'}^{r*} c_a^r \langle b | z | a' \rangle \langle a | z | b \rangle \\ &\quad \times e^{-i(E_{a'} - E_b)t_0} \tilde{f}_2(E_a - E_b - \omega_X) + c.c., \end{aligned}$$

where the last expression again is only for $t > t_0$. The core state has a finite lifetime due to autoionisation, which we can model by introducing an imaginary part to the energy as $E_b \to E_b - i\frac{\Gamma_b}{2}$, where Γ_b is the decay rate of the state b. Performing the Fourier transform to find the absorption signal, we neglect the complex conjugate part since it has a variation in time as $e^{-i(E_a - E_b)t}$, which corresponds to emission of a

photon with frequency $E_a - E_b$ when the system is excited. The dipole moment in the frequency domain is

$$D_z(\omega) = \mathcal{E}_{0,2} \sum_{a,a',b,r} c_{a'}^{r*} c_a^r \langle b|z|a'\rangle\langle a|z|b\rangle \tag{9.17}$$

$$\times \frac{e^{i(E_a - E_{a'})t_0}}{\omega_X + E_b - i\Gamma_b/2 - E_a} \tilde{f}_2(E_a - E_b - \omega_X), \tag{9.18}$$

which is to be introduced into Eqs. (9.9) and (9.6) in order to obtain the signal. We assume that the generated signal is much weaker than the incoming attosecond pulse and keep only the term that is first order in the generated signal

$$\begin{aligned} S(\omega) &\propto 2\mathrm{Re}\left(i\frac{2\pi\omega nl}{c}\mathcal{E}_{\mathrm{in}}^*(\omega)D_z(\omega)\right) \\ &= \frac{4\pi\omega nl}{c}\mathcal{E}_{0,2}^2 \mathrm{Im}\left(\sum_{a,a',b,r} c_{a'}^{r*} c_a^r \frac{\langle b|z|a'\rangle\langle a|z|b\rangle e^{i(E_a - E_{a'})t_0}}{\omega_X + E_b - i\Gamma_b/2 - E_a}\right. \\ &\quad \left.\times \tilde{f}_2^*(\omega - \omega_X)\tilde{f}_2(E_a - E_b - \omega_X)\right). \end{aligned} \tag{9.19}$$

The result found here is identical to what was found in Refs. [12, 65], except for the fact that they have introduced the reduced density matrix

$$\rho_{a,a'} = \sum_r c_{a'}^{r*} c_a^r. \tag{9.20}$$

The result in Eq. (9.18) shows that even if the lifetime of the coherence introduced through the absorption of the attosecond pulse is much longer than the duration of the pulse, attosecond absorption spectroscopy can still be used to make time-resolved measurements with a precision determined by the duration of the pulse. In this case, the absorption signal oscillates with a frequency determined by $e^{i(E_a - E_{a'})t_0}$, where the energy difference between the two valence states is 0.7 eV. These oscillations, with a period of 6.3 fs, can be resolved even though the absorption process is determined by the much longer lifetime of the 3d state. The absorption lines corresponding to the different fine-structure levels can also be separated because the width of the lines is

determined by the lifetime of the coherence (in this case the 3d state) and not the duration of the attosecond pulse. Probing the oscillations in Eq. (9.19) gives access to the relative phase between the $4p_{1/2}$ and $4p_{3/2}$ parts of the valence hole and in that sense the oscillations show how the valence hole changes in time as $|4p_{1/2}\rangle + |4p_{3/2}\rangle$ and $|4p_{1/2}\rangle - |4p_{3/2}\rangle$ have different spatial forms.

9.2.1 Absorption Spectroscopy with Two Attosecond Pulses

We now consider the case where two attosecond pulses are used in a transient absorption experiment. In the previous case, an intense laser pulse was used to set up a superposition state by coherently ionising from two valence states. The attosecond pulse was used to subsequently probe the evolution of the created state. The first attosecond pulse is used to ionise atomic krypton and the second attosecond pulse with a different central frequency can then drive a transition from a core level to the hole created by the first pulse. We present two examples of attosecond absorption spectroscopy schemes used to study the hole formation and the hole evolution in krypton atoms. We refer to a state that is created by the pump pulse as a hole state and a state from which the probe pulse may promote an electron into the hole state as a core state. In the first example the hole states are the $4p$ states and the core states are the $3d$ states. In the other example we consider a hole in the $4s$ or $3d$ states and probe it through the coupling to the $3p$ core states. The relevant states in krypton are shown in Fig. 9.1, along with the calculated binding energy for each of the states. The advantage with switching to two attosecond pulses, instead of a longer pulse in combination with an attosecond pulse, is that you can probe not only the evolution of the hole after the creation, but also the creation of the hole on the attosecond time-scale[67]. The creation of the hole is determined by the first laser pulse, but theoretical works show that the reorganisation of the electrons also leads to a response to the ionisation on the attosecond time-scale[68]. Currently, however, the intensity of the attosecond pulses is too low for attosecond pump – attosecond probe experiments.

We consider the same Hamiltonian as in Eq. (9.12) and the same essential state expansion as in Eq. (9.13). We suggest a pump-probe scheme with two attosecond pulses, which sets some restrictions. We assume that the pulses are sufficiently weak that we may treat the interaction in lowest-order perturbation theory and that the probe pulse is weaker than the pump pulse such that we can neglect any ionisation due to the probe pulse that induces transitions between bound states. The population in the core states due to the ionisation by the pump pulse followed by excitation by the probe pulse is proportional to V_1V_2, whereas the ionisation and excitation by the probe pulse is proportional to V_2^2. To be able to use the pump-probe scheme, we need the first term to dominate, $V_1 > V_2$, since the second part does not hold any information about the evolution that occurs in the time in-between the two pulses. Assuming that V_1 dominates, we neglect the ionisation due to V_2, which leads to the following equations for the coefficients in Eq. (9.13)

$$\begin{aligned} c_0(t) &= 1 \\ c_a^r(t) &= -i\int^t dt'\,\mathcal{E}_1(t')e^{i(E_r-E_a)t'}\langle r|z|a\rangle \\ c_b^s(t) &= -i\sum_a\int^t dt'\,\mathcal{E}_2(t'-t_0)c_a^s(t')e^{i(E_a-E_b)t'}\langle a|z|b\rangle. \end{aligned} \tag{9.21}$$

We have used the Slater-Condon rules to reduce the many-body matrix elements to single electron integrals, similar to what was done in Eq. (9.15). After both pulses are over, the time-evolution of the dipole moment is trivial as none of the expansion coefficients change. To proceed, we will make approximations allowing us to calculate the time integrals in the above expressions analytically. First we assume that the duration of the attosecond pulses is shorter than the coherence lifetimes and the Auger lifetimes of the states involved. We need to calculate

$$D_z(\omega) = \int dt\, e^{i\omega t}\langle D_z(t)\rangle, \tag{9.22}$$

with

$$\langle D_z(t)\rangle = \sum_{a,b,r} c_b^r(t)^* c_a^r(t) e^{i(E_a-E_b)t}\langle a|z|b\rangle + c.c. \tag{9.23}$$

If the attosecond pulses are both very short, then most of the contribution to the integral in Eq. (9.22) comes from after both pulses are over.

To be able to reproduce some of the subtle effects like in Refs. [67, 68] it may be advantageous to do numerical integration of Eq. (9.22) to catch all of the very short lived effects. Here we take an analytical approach. If we assume that the pulses have sine-squared envelopes

$$\vec{\mathcal{E}}_i(t) = \vec{\mathcal{E}}_{0,i} \sin^2\left(\frac{\pi t}{\tau_i}\right) \cos(\omega_i t), \tag{9.24}$$

then we can analytically integrate the coefficients in Eq. (9.21) up to a time $\tau > \max(\tau_1, t_0 + \tau_2)$ after which both pulses are over and the coefficients are constant. In Eq. (9.24), $\vec{\mathcal{E}}_{0,i}$ is the peak electrical field strength, τ_i is the duration of the pulse (with the FWHM $\tau_{\mathrm{FWHM,i}} = \tau_i/2$) and ω_i is the central frequency.

Once the coefficients $c_a^r(\tau)$ and $c_b^r(\tau)$ are determined at a time τ after the pulses are over, the full evaluation of the absorption spectrum is easily calculated from Eqs. (9.9)-(9.22)

$$\vec{\mathcal{E}}_{\mathrm{gen}}(\omega) = \frac{2\pi i\omega}{c} nl\vec{D}(\omega), \tag{9.25}$$

with

$$\begin{aligned} \vec{D}(\omega) &= \int dt\, e^{i\omega t} \langle \vec{D}(t) \rangle \\ &= \sum_{a,b,r} c_b^r(\tau)^* c_a^r(\tau) \langle a|z|b\rangle \\ &\quad \times \int_{t_0}^{\infty} dt e^{i\omega t} e^{-i(E_a - E_b)t} e^{-\frac{\Gamma_{ab}}{2}(t-t_0)} \\ &= i \sum_{a,b,r} c_b^r(\tau)^* c_a^r(\tau) \langle a|z|b\rangle \frac{e^{-i(E_a - E_b - \omega)t_0}}{E_a - E_b - i\frac{\Gamma_{ab}}{2} - \omega} \end{aligned} \tag{9.26}$$

Here we have introduced $\Gamma_{ab} = \tau_{ab}^{-1}$, with τ_{ab} the lifetime of the coherence between the states a and b. We approximate this coherence lifetime with the Auger lifetime of the shorter living core state. The complex conjugate part in Eq. (9.23) has been discarded, since it does not have any contribution in the frequency range of interest for absorption.

If the hole state a has a finite lifetime, we may again model this by adding an imaginary part to the energy, $E_a \to E_a - i\frac{\Gamma_a}{2}$. Assuming that

this lifetime is much longer than the duration of the attosecond pulses, we can introduce it directly into Eq. (9.26).

We assume that the lifetime is much longer than the lifetime of the coherence with the core states b and note that the lifetime of the hole state enters into both the coefficient $c_a^r(t)$ and $c_b^r(t)$, such that at the arrival of the probe pulse, $c_a(t_0)$ has decreased to $c_a(t_0)e^{-\frac{\Gamma_a t_0}{2}}$. Since $c_b(t)$ is determined by $c_a(t_0)$ (see Eq. (9.21)) it too will be reduced by the same factor. The fact that the hole may decay before the probe pulse arrives leads to a damping in the core state population. The final expression for the induced electric field then reads

$$\vec{\mathcal{E}}_{\text{gen}}(\omega) = -\frac{2\pi\omega}{c} nl \sum_{a,b,r} c_b^{r*} c_a^r \langle a|z|b\rangle \frac{e^{-i(E_a - E_b - \omega - i\Gamma_a)t_0}}{E_a - E_b - i\frac{\Gamma_b}{2} - \omega}, \tag{9.27}$$

where we have dropped the τ dependence on the coefficients to lighten the notation.

The result in Eq. (9.27) corresponds to a series of absorption peaks, centred at the difference between the hole and the core states, $E_a - E_b$. The strength of the peaks is determined by a summation (integration) over all of the possible final states of the ionised electron, a.

9.3 Attosecond Absorption Spectroscopy in Krypton

In this section we present two examples of absorption spectra calculated from the theory presented above. Both examples are for atomic krypton, but we consider two different pairs of attosecond pulses and hence two different sets of hole and core states.

9.3.1 Atomic Parameters

The binding energies, the dipole matrix elements and the Auger rates for the relevant states in krypton are calculated by Eva Lindroth from Stockholm University. The methods used are presented in Refs. [69–71]. The fully relativistic calculations are done with the Hartree-Fock

Table 9.1 | Binding energies of the relevant states in krypton. All results are in eV.

$3p_{1/2}$	$3p_{3/2}$	$3d_{3/2}$	$3d_{5/2}$	$4s_{1/2}$	$4p_{1/2}$	$4p_{3/2}$
223.43	215.82	96.78	95.45	26.53	14.86	14.18

method in the framework of the Dirac equations. The binding energies of the electronic states are listed in Table 9.1.

The dipole matrix elements are needed to determine the transition probabilities for promoting a core electron to a hole. According to the Wigner-Eckart theorem, the dipole matrix elements can be factored into a geometrical part and a reduced matrix element as

$$\langle \gamma_a j_a m_a \mid z \mid \gamma_b j_b m_b \rangle = (-1)^{j-m} \begin{pmatrix} j_a & 1 & j_b \\ -m_a & 0 & m_b \end{pmatrix} \langle \gamma_a j_a \mid\mid \vec{r} \mid\mid \gamma_b j_b \rangle, \tag{9.28}$$

where j and m are the angular momentum quantum numbers of the involved orbitals. The label γ just indicates other specifications of the state. The reduced matrix element contains all information about the radial overlap and is independent of the m-values. We list the reduced matrix elements, $\langle \gamma_a j_a \mid\mid \vec{r} \mid\mid \gamma_b j_b \rangle$, as calculated within the Dirac-Fock approximation, for all the involved orbitals in Table 9.2.

The 4s level is bound by less than twice the binding energy of the $4p_{3/2}$ valence electrons and cannot autoionise. All of the $n = 3$ states are however above the threshold for autoionisation. Eva Lindroth has calculated both the Auger rates and the spontaneous radiative decay rates for the core states. The Auger rates are completely dominating, with the radiative lifetimes being several picoseconds and the Auger lifetimes being only a fraction of a femtosecond to a few femtoseconds. The Auger lifetimes are listed in Table 9.3.

The final atomic parameters needed in the model are the coupling strengths of the hole states to the continuum. We find the continuum states by solving a non-relativistic Schrödinger equation with a local potential constructed from the relativistic Dirac-Fock electron density. The continuum states are solved in a radial box of range 200 a.u. In

Table 9.2 | Reduced dipole matrix elements determining the transition rates between the different core and hole states in krypton. The results are in atomic units.

$\langle 3d_{3/2} \,\|\|\, \vec{r} \,\|\|\, 3p_{1/2} \rangle$	-0.601
$\langle 3d_{3/2} \,\|\|\, \vec{r} \,\|\|\, 3p_{3/2} \rangle$	0.271
$\langle 3d_{5/2} \,\|\|\, \vec{r} \,\|\|\, 3p_{3/2} \rangle$	-0.817
$\langle 4s_{1/2} \,\|\|\, \vec{r} \,\|\|\, 3p_{1/2} \rangle$	-0.118
$\langle 4s_{1/2} \,\|\|\, \vec{r} \,\|\|\, 3p_{3/2} \rangle$	-0.183
$\langle 4p_{1/2} \,\|\|\, \vec{r} \,\|\|\, 3d_{3/2} \rangle$	-0.258
$\langle 4p_{3/2} \,\|\|\, \vec{r} \,\|\|\, 3d_{3/2} \rangle$	-0.110
$\langle 4p_{3/2} \,\|\|\, \vec{r} \,\|\|\, 3d_{5/2} \rangle$	-0.337
$\langle 4p_{1/2} \,\|\|\, \vec{r} \,\|\|\, 4s_{1/2} \rangle$	1.378
$\langle 4p_{3/2} \,\|\|\, \vec{r} \,\|\|\, 4s_{1/2} \rangle$	-1.953

Table 9.3 | Auger transition lifetimes in krypton. The lifetimes are related to the transition rates through $\Gamma = \tau^{-1}$. All results are in fs.

$3p_{1/2}$	$3p_{3/2}$	$3d_{3/2}$	$3d_{5/2}$
0.66	0.61	13.3	12.8

Fig. 9.2 the radial dipole matrix elements

$$r_{ab} = \int_0^\infty dr\, \phi_a(r) r \phi_b(r) \tag{9.29}$$

are shown. For a given electron continuum energy, the matrix elements entering the calculation are obtained from the radial dipole matrix elements by multiplying the appropriate angular factors.

9.3.2 Ionisation from the 4p Level and Coupling to 3d

To address the hole in the 4p valence shell, we use a pump pulse with a central frequency of $\omega_1 = 50$ eV and a duration $\tau_1 = 450$ asec. The probe

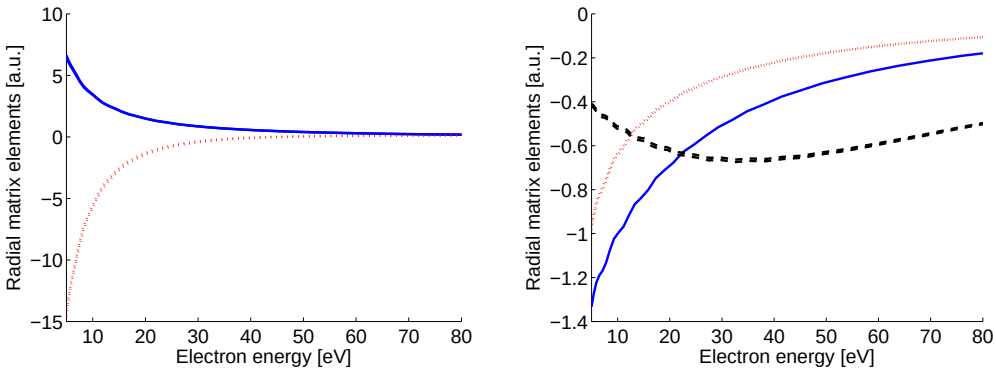

Figure 9.2 | (Left) The radial dipole matrix element between the 4p states in krypton and the s-wave continuum (blue curve) or the d-wave continuum (red curve). The overlaps are calculated for the $4p_{j=1/2}$ and $4p_{j=3/2}$ states. The radial difference in these states is very small and the difference in the matrix elements cannot be seen on the scale of the figure. (Right) The radial dipole matrix element between the 4s state in krypton and the p-wave continuum (blue curve) and the overlap between the 3d-states and the p-wave continuum (red curve) or the f-wave continuum (black curve).

pulse is centred at $\omega_2 = 81$ eV appropriate for the coupling of the 3d and 4p states and its duration is the same as the pump pulse, $\tau_2 = \tau_1 = 450$ asec. The duration of the pulses ensures that they are so spectrally narrow that the pump pulse cannot drive the 3d-4p–transition by itself. The strength of the pulses gives an overall scaling of the strength of the signal and the intensity is kept such that both pulses lead to interactions that are in the perturbative regime. Furthermore, we keep the intensity of the second pulse such that it induces bound-bound transitions, but sufficiently weak that we may ignore ionisation due to this pulse. The radial dipole moment is also much bigger at continuum electron energies around 35 eV than for kinetic energies around 65 eV (see Fig. 9.2), which is the kinetic energy of electrons ionised by the probe pulse. The spectral profiles of the two pulses are shown in Fig. 9.3.

We construct the signal from Eq. (9.6) by subtracting the contribution from the incoming field and by considering only the dominant term. The spectrum reads

$$S(t_0, \omega) \propto \mathrm{Re}\left(\vec{\mathcal{E}}^*_{\mathrm{in}}(\omega) \cdot \vec{\mathcal{E}}_{\mathrm{gen}}(\omega)\right), \tag{9.30}$$

where t_0 denotes the relative delay between the pulses. In a measurement, the contribution to the spectrum from the incoming field may be

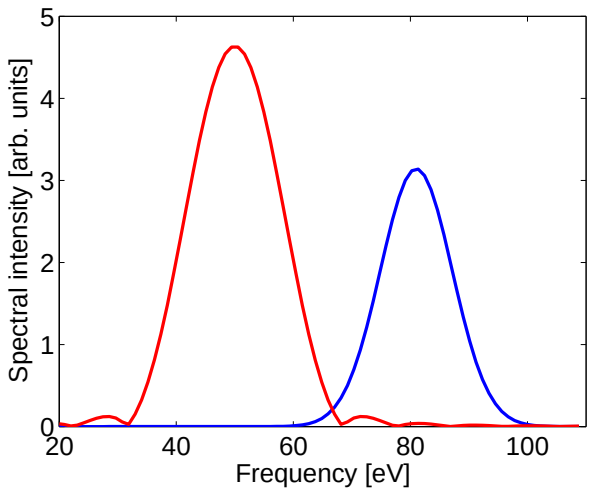

Figure 9.3 | Spectral profiles of the two attosecond pulses (in arbitrary units). The photon energy of the pump pulse, centred at 50 eV, is insufficient to drive the transitions from the 3d core levels to the 4p valence holes, which are just above 80 eV. The intensity of the probe pulse, centred at 81 eV, is insufficient to cause ionisation of the system.

subtracted by recording the absorption spectrum when the probe pulse precedes the pump pulse by a sufficiently long time that there is no overlap in the signals from the two pulses. The generated field is calculated from Eq. (9.27). The absorption spectrum is plotted in Fig. 9.4 as a function of the relative delay between the pump and the probe pulse. While the coefficients are calculated for the sine-squared envelope of the field, the field is assumed to be Gaussian in the plots of the spectrum to avoid any artificial tails extended to frequencies far from the central one.

In the spectrum, three lines are seen as originating from the 3d to 4p transitions, since the fourth possible line from the $3d_{5/2} \rightarrow 4p_{1/2}$ is forbidden by dipole selection rules. In the right part of Fig. 9.4 the signal at the centre of the three lines is plotted. The strongest line is from the $3d_{5/2} \rightarrow 4p_{3/2}$, which can be understood from the fact that the most electrons are involved here, with six electrons in the $3d_{5/2}$ states and four in the $4p_{3/2}$. The line shows no oscillations since there is only one way to populate each of the two states involved, as the $3d_{5/2}$ may only be populated via the $4p_{3/2}$ hole state.

Turning to the absorption line at 81.9 eV corresponding to the $3d_{3/2} \rightarrow$

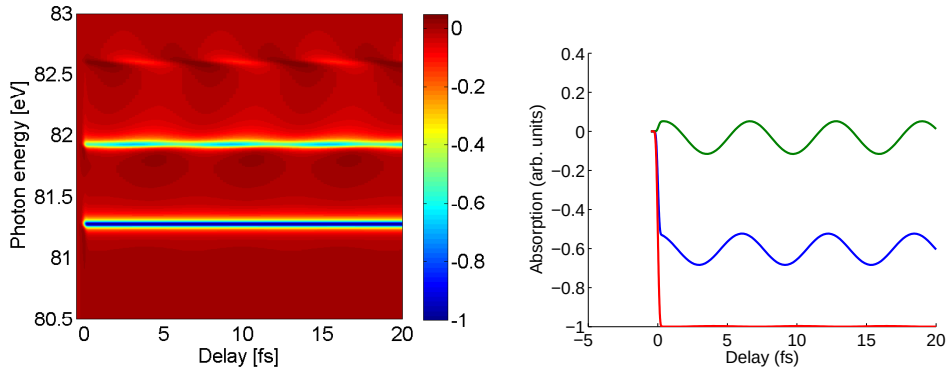

Figure 9.4 | (Left) Normalised absorption spectrum for holes in the 4p valence shell. The spectrum shows three lines at 81.3eV, 81.9eV and 82.6eV corresponding to the $3d_{5/2} \to 4p_{3/2}$, $3d_{3/2} \to 4p_{1/2}$ and $3d_{3/2} \to 4p_{3/2}$ transitions. (Right) Horizontal intersects through the lines. The lines are $3d_{5/2} \to 4p_{3/2}$(red), $3d_{3/2} \to 4p_{1/2}$(blue) and $3d_{3/2} \to 4p_{3/2}$(green).

$4p_{1/2}$ transition, we find that this is weaker and that it shows oscillations with a period of 6.2 fs, corresponding to an energy difference $\Delta E = \frac{2\pi}{T} = 0.68$ eV, which is exactly the difference between the two $4p$ states. The oscillations in the absorption line originate from the population of the core hole $c_{3d_{3/2}}$. A hole in $3d_{3/2}$ can be created through two different channels, either via an intermediate $4p_{1/2}$ hole or via a $4p_{3/2}$ hole, cf. Eqs. (9.21). These two channels may interfere either constructively or destructively, depending on the delay between the two pulses, because the time-evolution of the intermediate states is different:

$$\begin{aligned} c^r_{3d_{3/2}} &= -\langle 4p_{1/2}|z|3d_{3/2}\rangle \int dt'\, \vec{\mathcal{E}}_2(t'-t_0) e^{i(E_{4p_{1/2}}-E_{3d_{3/2}})t'} \\ &\quad \times \langle r|z|4p_{1/2}\rangle \int dt'\, \vec{\mathcal{E}}_1(t') e^{i(E_r-E_{4p_{1/2}})t'} \\ &\quad -\langle 4p_{3/2}|z|3d_{3/2}\rangle \int dt'\, \vec{\mathcal{E}}_2(t'-t_0) e^{i(E_{4p_{3/2}}-E_{3d_{3/2}})t'} \\ &\quad \times \langle r|z|4p_{3/2}\rangle \int dt'\, \vec{\mathcal{E}}_1(t') e^{i(E_r-E_{4p_{3/2}})t'}. \end{aligned} \tag{9.31}$$

A summation over the magnetic substates is implied. The oscillations in Fig. 9.4 are due to the second pulse being centred at t_0 and the integral acquiring a phase $e^{i(E_{4p_j}-E_{3d_{3/2}})t_0}$, which is different for the two terms in Eq. (9.31). Similarly to the experiment with strong-field ionisation[12],

in this perturbative regime we may think of the pump pulse as setting up a coherent superposition in the $4p$ valence shell. The superposition is either interfering constructively or destructively as we promote a $3d$ core electron to the valence hole. The dominant term goes via the $4p_{1/2}$ state and gives rise to the constant background in the signal, while the oscillations are due to the $4\mathrm{p}_{3/2}$ pathway.

For the weakest of the absorption lines, the $3\mathrm{d}_{3/2} \rightarrow 4\mathrm{p}_{3/2}$ line at 82.6 eV, the oscillations are still due to the two different pathways to the $3\mathrm{d}_{3/2}$ state and still the pathway via $4\mathrm{p}_{1/2}$ is dominant. This is not as obvious at it may sound, as different final states may contribute to the total signal through the sum(integral) over the free electron states, see Eq. (9.27). Since the time-evolution of the two 4p states is different, the pathway via the $4\mathrm{p}_{1/2}$ state leads to oscillations that are now greater than the constant signal originating from the $4\mathrm{p}_{3/2}$ pathway. This means that the absorption may actually be negative at some delays, that is, the generated field will add constructively to the incoming field.

Absorption spectroscopy with attosecond pump – attosecond probe pulses allows us to study the hole formation on a very short time scale by comparing the build-up of the absorption signal as the pulses overlap. Zooming in on only the area where the two pulses overlap, we are able to temporally resolve the hole formation on an attosecond timescale. This is shown in Fig. 9.5.

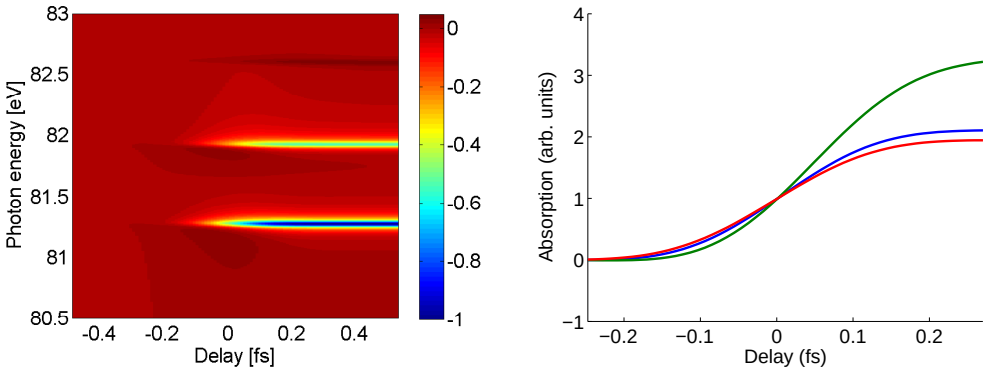

Figure 9.5 | Focusing only on the times when the two pulses overlap, we may resolve the build-up of the holes on an attosecond timescale. The left panel shows the absorption spectrum and the right panel shows the absorption for the three lines, normalised at $t_0 = 0$. The lines are the same as in Fig. 9.4.

In our model, we include no relaxation effects in the ion, treating the electrons as independent within the Hartree-Fock approximation. Hence, what we see as the build-up of the holes is mostly determined by the temporal profile of the two pulses involved. If many-electron effects are at play and give rise to a delay in the hole formation on the attosecond time-scale, the method proposed here might be able to reveal differences in the formation time by showing a delay between the rise of the absorption curves or short time oscillations in the absorption[67, 68]. The differences seen in the right panel in Fig. 9.5 are due to the interference between the different channels. The reason is the same as that for the oscillations in Fig. 9.4. No correlation effects are included in the construction of the time-dependent wave functions in this work.

9.3.3 Ionisation from the 3d Level and Coupling to 3p

Perhaps a more interesting case to study is when the pump pulse removes an inner-shell electron and the probe pulse then promotes a core electron to the hole. As an example, we propose using an attosecond pulse to remove an electron from the krypton 3d shell and then promote a 3p electron into the 3d hole. In this example, we furthermore require that the probe pulse spectrally is broad, such that it may also drive the transition from the 3p to the 4s state.

We calculate the absorption spectrum for a pump pulse centred at $\omega_1 = 100$ eV and with a slightly longer duration of $\tau_1 = 750$ asec such that it is spectrally narrower and does not populate the Rydberg states in the krypton atom. The probe pulse is centred at $\omega_2 = 160$ eV and has a duration of $\tau_2 = 100$ asec, which makes is spectrally broad enough to drive both the 3p $\rightarrow$ 3d and the 3p $\rightarrow$ 4s transitions. Again, we use a sine-squared envelope for the calculations of the atomic coefficients in Eq. (9.21), but a Gaussian pulse when plotting the spectra from the second term in Eq. (9.6) to avoid the tails of the pulse.

In Fig. 9.6 the absorption spectra as well as the absorption at the centre of the lines are plotted. Turning first to the 3p $\rightarrow$ 3d lines (top panel), we see that the finite lifetime of the 3d state now leads to a decrease of the signal as the probe pulse is delayed with respect to

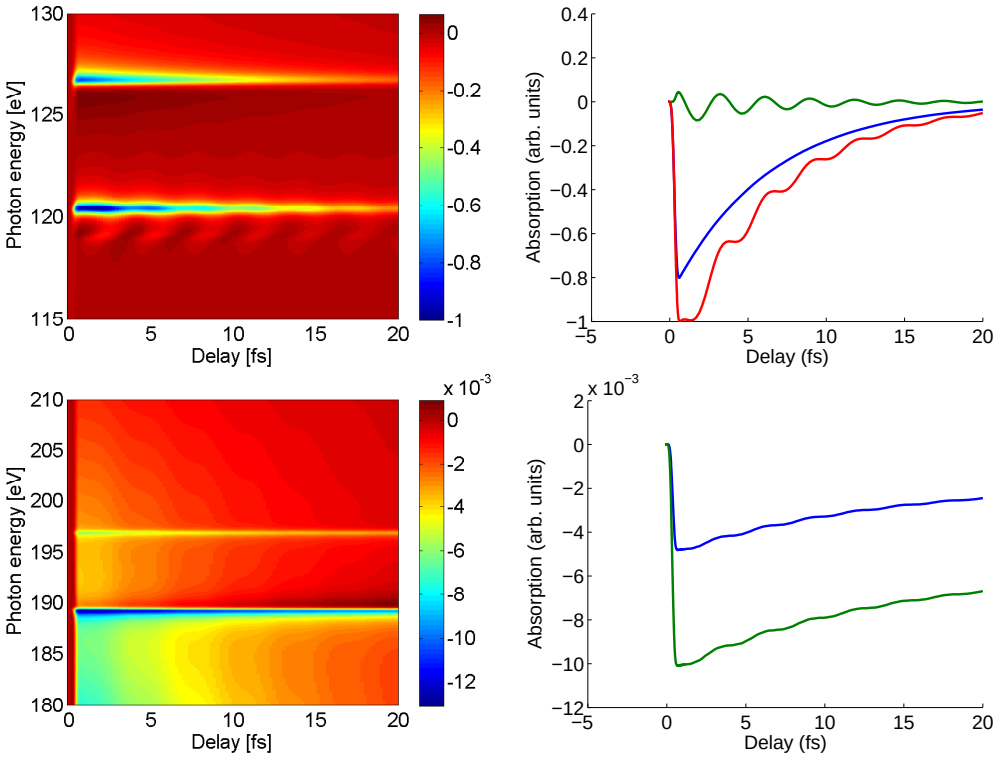

Figure 9.6 | Absorption spectra calculated for the set of pulses tuned to drive the transitions from the 3p level. The top spectra show the lines corresponding to the 3d levels and the bottom spectra are for the 4s level. The left figures are the full spectra and the right figures show the intersects at the centre of the absorption lines. Notice that the set of parameters mean that the absorption at the 3p $\rightarrow$ 4s lines is two orders of magnitude weaker than the 3p $\rightarrow$ 3d lines.

the pump pulse. Similarly to the first example, there are two different pathways to populate the $3p_{3/2}$ state, leading to interference between the channels and oscillations in the signal. This gives access to a direct time-domain measurement of both the lifetime of the 3d levels and the lifetime of the coherence in the 3d levels, through the decay of the signal and the decay of the oscillations. In our model the decay of the coherence is determined by the decay of the population, but the two may be on different time-scales. The lifetime of the 3d states is 13.3 fs for the $3d_{3/2}$ state and 12.8 fs for the $3d_{5d/2}$.

The 4s state (bottom panel in Fig. 9.6) is below the Auger threshold and is expected to live very long. The lifetime due to spontaneous radiative decay is $\approx$ 500 ps. With the choice of pump pulse aimed at

the 3d level, however, it is very sparsely populated and hence the signal is very weak. The decay in the absorption line, i.e. the decrease in the absolute signal, is the tail of the 3p to 3d transitions which extend even to these much higher energies. The signal from the 4s level is at about 1 % of the signal from the major lines.

The response to the removal of a krypton 3p electron was studied in [68], where it was shown that multielectron effects give rise to oscillations in the hole occupation on a 100 asec timescale. Multielectron effects are not included in our work, but the method presented here, should be able to resolve these, especially if the pump pulse is shorter than what is considered here. Our work gives an experimental protocol to test the response of the atom on an attosecond timescale.

Chapter

10 High-order Harmonic Spectroscopy

High-order harmonic generation (HHG) is often described in the three-step model[24] where the picture is that an electron in an atom or molecule is ionised, the electron travels in the continuum, and returns two-thirds of an optical period later to recombine with the parent ion. The structure of the high-order harmonic spectrum holds signatures of the evolution of the atomic or molecular ion while the electron is in the continuum, since the recombination process depends on the current state of the ion at the time of return. High-order harmonic specstroscopy has been used to probe the molecular structure[72, 73], the evolution of the electronic hole[74, 75], the molecular rearragement from the neutral ground state to the ionic[76, 77], and for tomographic reconstruction of the atomic or molecular orbital[78, 79].

The high-order harmonic spectrum usually consists of the odd harmonics of the fundamental laser field used to drive the HHG. The spectrum has a rapid drop-off for the low-order harmonics followed by a plateau of harmonics with close to equal amplitude ending in a rapid cut-off determined by the binding energy of the active electron and the laser intensity. The overall strength of the signal depends crucially on phase-matching conditions and the macrosopic propagation through the target medium, but models based on just a single atom or molecule can often describe a lot of the physics at play. The characteristic signals one looks for in the spectra are extension of the cut-off or the strength and

position of dips or bumps in the plateau region. The generated high-order harmonic radiation is calculated from the Fourier transform of the time-dependent atomic or molecular dipole moment, the dipole velocity or the dipole acceleration. Based on the arguments already presented in Sec. 9.1 we argue that the high-order harmonic signal relates directly to the Fourier transform of the dipole velocity.

10.1 On the Choice of Form in HHG Calculations

The question we address here is how the high-order harmonic spectrum is related to the response calculated from a single atom or molecule. Does it relate directly to the dipole (D_z),

$$S_{dip}(\omega) \propto \left| \int_{-\infty}^{\infty} dt \langle \Psi(t) | D_z | \Psi(t) \rangle e^{i\omega t} \right|^2, \tag{10.1}$$

the dipole velocity ($\dot{D}_z$)

$$S(\omega) \propto \left| \int_{-\infty}^{\infty} dt \langle \Psi(t) | \dot{D}_z | \Psi(t) \rangle e^{i\omega t} \right|^2, \tag{10.2}$$

or the dipole acceleration ($\ddot{D}_z$)

$$S_{acc}(\omega) \propto \left| \int_{-\infty}^{\infty} dt \langle \Psi(t) | \ddot{D}_z | \Psi(t) \rangle e^{i\omega t} \right|^2, \tag{10.3}$$

for a pump linearly polarised along z direction and a system described by $|\Psi(t)\rangle$? This question was addressed in Ref. [80], where the HHG spectrum was related to the norm-squared of the Fourier transform of the dipole acceleration. Also Refs. [81–83] related the HHG spectrum to the dipole acceleration. In a more recent work[84], however, a quantum-electrodynamical approach was taken and results corresponding to the ones of Ref. [80] were obtained except that the spectrum was shown to relate naturally to the dipole velocity. Currently, there is no consensus in the literature of what quantity to calculate in order to predict the harmonic spectrum generated by a single atom or molecule. For example,

in Refs. [85–87] the harmonic signal is calculated as the norm squared of the Fourier transform of the time-dependent dipole (Eq. (10.1)), while in Refs. [88–92] the spectrum is calculated as the norm squared of the Fourier transform of the time-dependent dipole acceleration (Eq. (10.3)).

In our analytical approach, we consider an incoming light pulse $\mathcal{E}_{in}(t - x/c)$ propagating in the x direction and linearly polarised along the z direction. We place the atom or molecule at the origin. The fundamental field will induce a dipole in the quantum system and harmonics will be generated as described by an additional field $\mathcal{E}_{\text{gen}}(x, t)$. The resulting total electric field is denoted by $\mathcal{E}(x, t)$. At a fixed observation point after the atom or molecule the spectral distribution function $S(\omega)$ is given by (see, for example, Ref. [93])

$$S(\omega) = |\mathcal{E}(\omega)|^2 = \frac{1}{4\pi^2} \left| \int_{-\infty}^{\infty} dt\, \mathcal{E}(t) e^{i\omega t} \right|^2 . \tag{10.4}$$

We are interested in the high-order harmonics and the fundamental, incoming field has no frequency components at the frequencies of interest. Hence, only the generated electric field contributes and

$$S(\omega) = |\mathcal{E}_{\text{gen}}(\omega)|^2. \tag{10.5}$$

We now refer back to Sec. 9.1 and particularly Eq. (9.9) which tells us that the generated electric field is proportional to the dipole velocity. We find

$$S(\omega) = \frac{4\pi^2}{c^2} \left| \dot{D}_z(\omega) \right|^2 , \tag{10.6}$$

showing that Eq. (10.2) is the correct choice of form for HHG calculations.

We now consider the relation of the spectrum to the formulation with the dipole and the dipole acceleration forms. If we assume that at large negative and positive times, that is long before and after the pulse, $D_z(t) = 0$ and $\dot{D}_z(t) = 0$ (see Refs. [83, 94, 95] for more general cases), partial integration gives

$$\dot{D}_z(\omega) = -i\omega D_z(\omega) \tag{10.7}$$

and

$$\dot{D}_z(\omega) = \frac{i}{\omega} \ddot{D}(\omega). \tag{10.8}$$

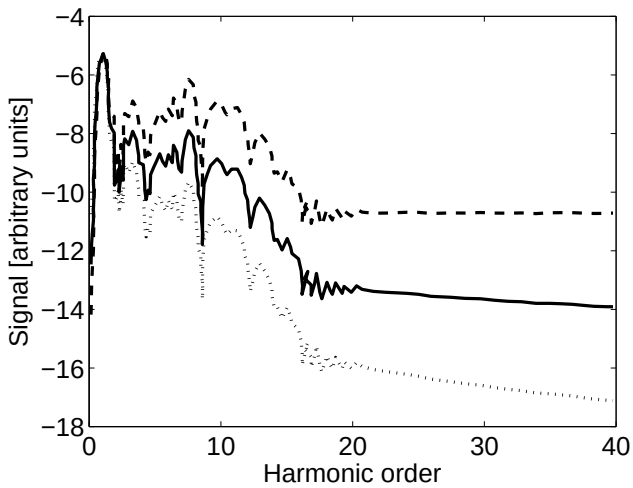

Figure 10.1 | High-order harmonic spectrum from hydrogen as a function of harmonic order for a 3 cycle pulse at a wavelength of 800 nm and an intensity of 3×10^{13} W/cm^2. The full curve shows $\log_{10}(|(\dot{D}_z(\omega)|^2)$, which is the signal up to trivial constants (see Eq. (10.6)) based on the velocity dipole form and is taken from reference [94]. The dashed curve shows $\log_{10}(\omega^2|(\dot{D}_z(\omega)|^2)$ which corresponds to the acceleration form, Eq. (10.3), and finally the dotted curve shows $\log_{10}(|(\dot{D}_z(\omega)|^2/\omega^2)$, which corresponds to the dipole form, Eq. (10.1). The curves have been scaled to the first peak in the spectrum of the full curve.

The corresponding spectra are obtained from Eq. (10.6), as

$$S(\omega) = \frac{4\pi^2\omega^2}{c^2}|D_z(\omega)|^2, \tag{10.9}$$

$$S(\omega) = \frac{4\pi^2}{\omega^2 c^2}|\ddot{D}_z(\omega)|^2. \tag{10.10}$$

Of particular interest here is the scaling with ω. Clearly, if the dipole acceleration as in Eq. (10.3) was taken as the fundamental form, one would obtain a different scaling with harmonic frequency ω in Eqs. (10.6), (10.9), and (10.10). In that case, the dipole velocity would be multiplied by ω^2 and the dipole form by ω^4, which is the underlying assumption in early works [80–83]. In other words, the way the spectra decrease as a function of ω depends on which form is taken as the fundamental reference from which to derive the spectra based on the other forms.

Fig. 10.1 illustrates this point. In the figure, the HHG spectrum for hydrogen is considered as a function of harmonic order for a 3 cycle

pulse with a sine-squared envelope for the vector potential, a central wavelength of 800 nm, and a peak intensity of 3×10^{13} W/cm^2. The full curve, taken from reference [94], shows $\log_{10}(|(\dot{D}_z(\omega)|^2)$, which is the signal up to trivial constants (see Eq. (10.6)) based on the velocity dipole form. As shown above, this is the form that relates directly to the field generated from a single atom or molecule. If erroneously the acceleration form of Eq. (10.3) were taken as the fundamental reference form, Eq. (10.8) would predict the result $\log_{10}(\omega^2|(\dot{D}_z(\omega)|^2)$ shown by the dashed curve. Finally, if – again by error – the dipole form of Eq. (10.1) were taken as the reference, Eq. (10.7) would predict the result $\log_{10}(|(\dot{D}_z(\omega)|^2/\omega^2)$ shown by the dotted curve in Fig. 10.1. As seen from the figure the dashed and the dotted curves generally differ from the correct full curve and in particular, they respectively over and under estimate the signal at harmonic high orders. Another consequence of the different scaling of the three forms is a change in minima positions and structures in the HHG spectra from molecules. Such minima may result from a destructive interference when the electron recombines after its excursion in the continuum. The position of the minima reflects the atomic positions at the instant of recombination as predicted [96] and observed [97, 98]. In Fig. 10.2 we illustrate the behaviour of the minimum in different forms. While the minimum is present in the case of the acceleration (dashed curve) and the velocity (full curve) form, the minimum has almost disappeared in the case of the dipole length form (dotted curve).

It is important to note that our aim here is to describe the single-system response and to set a standard for the choice of reference form when presenting theoretical HHG spectra. As discussed in the introduction, many calculations of high-order harmonic spectra are indeed carried out for single systems and the results of many HHG experiments are interpreted in terms of the single-system response. This approach is clearly an approximation since the full description of HHG requires inclusion of propagation through the medium, phase-matching effects, and absorption [99]. Other works have focused on these aspects and propagation effects may be very important depending on the experimental conditions. For example substantial efforts have been put into the calculation of macroscopic effects on the HHG spectrum[100–102], the influence on the generation of attosecond pulses[103, 104] and also

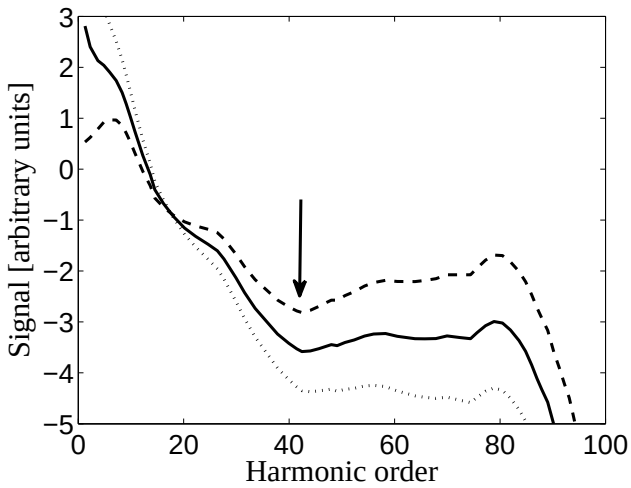

Figure 10.2 | Smoothed high-order harmonic spectrum for the hydrogen molecular ion for a 10 cycle pulse at 780 nm and peak intensity of 5×10^{14} Wcm^{-2}. The dashed curve is the acceleration form result $\log_{10}(|(\ddot{D}_z(\omega)|^2)$ taken from [96]. The full curve is the result with the velocity dipole form, $\log_{10}(|(\dot{D}_z(\omega)|^2/\omega^2)$, and the dotted curve is the result of the dipole form, $\log_{10}(|(D_z(\omega)|^2/\omega^4)$. The arrow indicates the position of the minimum at the 43rd harmonic as predicted by the acceleration form.

to investigate the effects of propagation on more delicate structures such as the Cooper minimum in argon [105]. In view of these works it is clear that no spectrum obtained by considering a single system can capture the full macroscopic response.

Chapter

11 Conclusion and Outlook

Attosecond physics is to a very high extend being driven forward by the advances in laser technology and optics. The first attosecond pulses were produced in the laboratory only a decade ago and the evolution has been very rapid ever since. In this work we have studied some applications of the attosecond pulses in time-resolved measurements. Since the attosecond pulses are weak, most experiments are performed using a combination of an attosecond pulse and a more intense femtosecond laser pulse. This is the case with the streaking measurements and the RABBITT technique for attosecond pulse trains. The challenge is that the intense laser pulse is not only probing the system, but also perturbing the system. The interpretation is not straight forward in terms of what is the temporal delay of interest and what are the shifts in the spectrum introduced by the measurement technique? The work presented here builds on analytical models and tries to identify some of the caveats and see how these effect the measurements.

Especially when it comes to the more complex systems, like the tungsten surface, there is a need for more data. Several models are proposed and all of them can seemingly reproduce the one number that is the relative delay measured in the experiment[6]. In this work, we presented one way of modelling the metal surface with a jellium model for the conduction band and a Bloch wave of localised electronic states for the core states, but these models do not include the Coulomb shifts or any

atomic effects. For smaller systems like atoms or molecules, numerical experiments may also be able to provide more data and provide the understanding that is needed in order to understand the more complex systems. We have also presented modelling of how the photoelectron distribution from a train of attosecond pulses in combination with the fundamental laser field can be used to perform time-resolved measurements. The RABBITT technique is in many ways very similar to the streaking technique and many of the same problems with interpreting a phase-delay in the spectrum as a temporal delay exist for the RABBITT measurement. The LAPE technique is not phase resolved and is in that sense perhaps more robust to some of the very subtle effects that affect the measurements, but the price to pay is a lower temporal resolution.

Finally, we have looked at attosecond absorption spectroscopy, where the signal is the absorption of the attosecond pulse instead of the emitted electrons. We have made a simple formulation of the absorption signal from the Maxwell wave equation and related the absorption signal to the expectation value of the dipole velocity, which can be calculated from quantum mechanical models. Absorption spectroscopy might be the easiest route towards attosecond pump – attosecond probe spectroscopy, as opposed to the streaking measurements where the probe is an intense femtosecond laser field. We have presented two examples of absorption spectra where two attosecond pulses are used as the pump and the probe. With attosecond pump – attosecond probe it will be possible to probe the formation of holes on the attosecond time-scale and perhaps see the rearrangement of the electron cloud which has been theoretically shown to be on the attosecond time-scale. Another advantage moving to the attosecond pump – attosecond probe is that the pulses involved will be weaker and the perturbation of the system will be smaller. In that sense, it will be easier to extract quantities that are system dependent without disturbing the system with the probe. A spin-off from studying the absorption process has been that we have been able to make some comments regarding high-order harmonic generation and show that the harmonic spectrum from a single atom or molecule is proportional to the norm-square of the dipole velocity.

11.1 Outlook

One of the great opportunities and challenges in strong-field physics and in ultrafast time-resolved measurements is the free electron lasers (FEL) that are currently starting to produce data at LCLS in Stanford and is being built at XFEL in Hamburg. The free electron lasers provide very high intensity in the ultraviolet to x-ray part of the electromagnetic spectrum and the new FEL sources are working hard to provide very short pulse durations, as short as a single femtosecond. Some of the very short pulse durations are reached using attosecond pulses to seed the FEL. It is a challenge to measure the characteristics of the FEL laser pulses just as it is difficult to measure the characteristics of the attosecond pulses. Techniques like the FROG-CRAB has been widely applied here and may also be useful for characterising the FEL pulses. The FROG-CRAB is however built on the strong-field approximation and more accurate modelling including for example the Coulomb potential might be able to provide a more accurate reconstruction for both attosecond pulses and for use with FEL.

All of the models presented in this work are based on the single-active-electron approximation, while other studies have shown that interesting many-electron dynamics take place on an attosecond timescale. It would be very interesting to be able to treat many-electron physics in the modelling and see the effect it has on the measured streaking spectra and what signatures we should look for in order to study the many-electron relaxation that takes place following ionisation. This also leads to the perhaps most interesting question in attosecond physics; can we see how the electron cloud rearranges prior to the nuclear rearrangement in a chemical reaction or can we even control the electronic rearrangement and by that control the chemical reaction?

In attosecond absorption spectroscopy it is clear that we have made a very crude model. We include no macroscopic propagation effects and no phase matching in the target. Including propagation effects in the model will lead to a better understanding of how to relate the measured absorption spectra to those calculated from a single atom or molecule. It will also be very interesting to calculate the atomic or molecular response more accurately for a many-electron system to see if the relaxation dynamics is visible in the absorption spectra and especially to

see how far we have to push the attosecond pulses in terms of duration and central photon energy before we can resolve the dynamics. The attosecond pulses needed are still not available in the laboratory, but the experimental progress is very rapid. It might not be very long before such experiments can be performed.

Chapter

12 Dansk resumé

Den naturlige tidsskala for elektroners bevægelse i atomer og molekyler er attosekundtidsskalaen, hvor 1 attosekund er 10^{-18} sekund (en milliardnedel af en milliardnedel af et sekund!). Ved hjælp af en teknik kendt som høj-harmonisk generation er det muligt at lave laserpulser, hvor varigheden er omkring 100 attosekunder. Disse kan bruges til at lave ekstremt hurtige tidsopløste målinger.

Attosekundpulser er så korte at man kan opløse svingningerne i det elektriske felt fra infrarødt laserlys. Man kan ved hjælp af en teknik kendt som attosekundstreaking direkte måle svingningerne i feltet og udnytte samme teknik til at se hvornår en elektron er blevet revet fri. På denne måde har man kunnet se hvor lang tid det tager en elektron at slippe ud fra en metaloverflade og endda hvor hurtigt en elektron bliver revet fri fra et neon atom. Eksperimenter har vist at der er 21 attosekunders forskel på hvor hurtigt elektroner bliver revet ud af to forskellige tilstande i neon, kendt som 2s og 2p. I denne afhandling præsenteres modeller for hvordan denne type tidsopløste målinger kan laves og hvordan man kan fortolke resultaterne. Vi studerer også hvordan et tog af attosekundpulser med en fast afstand kan bruges til at lave tidsopløste målinger og hvad man kan gøre med lidt længere pulser der ikke kan opløse svingningerne for infrarødt lys. Alle disse teknikker bygger på at sende en attosekund puls ind på det system man vil studere sammen med laserlys og så variere forsinkelsen mellem attosekundpulsen og ly-

set. Det signal man studerer er energifordelingen af de elektroner der på grund af attosekundpulsen bliver revet løs fra systemet og derefter bliver påvirket af det laserlyset.

Et alternativ er igen at sende to pulser ind på at system, men så se på absorptionen af den ene puls som funktion af forsinkelsen. Når en af pulserne har attosekund varighed er dette kendt som attosekund absorptionsspektroskopi. Absorptionen afhænger af præcis hvilken tilstand systemet er i når attosekund pulsen rammer det, men også af hvordan systemet udvikler sig efter pulsen har været der. I denne afhandling formulerer vi en model for hvordan man kan beregne absorptionssignalet ved at se på hvordan systemet udvikler sig i tiden.

Bibliography

[1] T. Brabec and F. Krausz, *Intense few-cycle laser fields: Frontiers of nonlinear optics*, Rev. Mod. Phys. **72**, 545–591 (2000).

[2] F. Krausz and M. Ivanov, *Attosecond physics*, Rev. Mod. Phys. **81**, 163 (2009).

[3] R. Kienberger, M. Hentschel, M. Uiberacker, C. Spielmann, M. Kitzler, A. Scrinzi, M. Wieland, T. Westerwalbesloh, U. Kleineberg, U. Heinzmann, M. Drescher and F. Krausz, *Steering Attosecond Electron Wave Packets with Light*, Science **297**, 1144–1148 (2002).

[4] R. Kienberger, E. Goulielmakis, M. Uiberacker, A. Baltuska, V. Yakovlev, F. Bammer, A. Scrinzi, T. Westerwalbesloh, U. Kleineberg, U. Heinzmann, M. Drescher and F. Krausz, *Atomic transient recorder*, Nature (London) **427**, 817–821 (2004).

[5] E. Goulielmakis, M. Uiberacker, R. Kienberger, A. Baltuska, V. Yakovlev, A. Scrinzi, T. Westerwalbesloh, U. Kleineberg, U. Heinzmann, M. Drescher and F. Krausz, *Direct Measurement of Light Waves*, Science **305**, 1267–1269 (2004).

[6] A. L. Cavalieri, N. Müller, T. Uphues, V. S. Yakovlev, A. Baltuska, B. Horvath, B. Schmidt, L. Blümel, R. Holzwarth, S. Hen-

del, M. Drescher, U. Kleineberg, P. M. Echenique, R. Kienberger, F. Krausz and U. Heinzmann, *Attosecond spectroscopy in condensed matter*, Nature (London) **449**, 1029–1032 (2007).

[7] J. Mauritsson, P. Johnsson, E. Mansten, M. Swoboda, T. Ruchon, A. L'Huillier and K. J. Schafer, *Coherent Electron Scattering Captured by an Attosecond Quantum Stroboscope*, Phys. Rev. Lett. **100**, 073003 (2008).

[8] M. Schultze, M. Fiess, N. Karpowicz, J. Gagnon, M. Korbman, M. Hofstetter, S. Neppl, A. L. Cavalieri, Y. Komninos, T. Mercouris, C. A. Nicolaides, R. Pazourek, S. Nagele, J. Feist, J. Burgd¨orfer, A. M. Azzeer, R. Ernstofer, R. Kienberger, U. Kleineberg, E. Goulielmakis, F. Krausz and V. S. Yakovlev, *Delay in Photoemission*, Science **328**, 1658 (2010).

[9] K. Klünder, J. M. Dahlström, M. Gisselbrecht, T. Fordell, M. Swoboda, D. Guénot, P. Johnsson, J. Caillat, J. Mauritsson, A. Maquet, R. Taïeb and A. L'Huillier, *Probing Single-Photon Ionization on the Attosecond Time Scale*, Phys. Rev. Lett. **106**, 143002 (2011).

[10] M. Uiberacker, T. Uphues, M. Schultze, A. J. Verhoef, V. Yakovlev, M. F. Kling, J. Rauschenberger, N. M. Kabachnik, H. Schröder, M. Lezius, K. L. Kompa, H.-G. Muller, M. J. J. Vrakking, S. Hendel, U. Kleineberg, U. Heinzmann, M. Drescher and F. Krausz, *Attosecond real-time observation of electron tunnelling in atoms*, Nature (London) **446**, 627–632 (2007).

[11] K. P. Singh, F. He, P. Ranitovic, W. Cao, S. De, D. Ray, S. Chen, U. Thumm, A. Becker, M. M. Murnane, H. C. Kapteyn, I. V. Litvinyuk and C. L. Cocke, *Control of Electron Localization in Deuterium Molecular Ions using an Attosecond Pulse Train and a Many-Cycle Infrared Pulse*, Phys. Rev. Lett. **104**, 023001 (2010).

[12] E. Goulielmakis, Z.-H. Loh, A. Wirth, R. Santra, N. Rohringer, V. S. Yakovlev, S. Zherebtsov, T. Pfeifer, A. M. Azzeer, M. F.

Kling, S. R. Leone and F. Krausz, *Real-time observation of valence electron motion*, Nature (London) **466**, 739 (2010).

[13] H. Wang, M. Chini, S. Chen, C.-H. Zhang, F. He, Y. Cheng, Y. Wu, U. Thumm and Z. Chang, *Attosecond Time-Resolved Autoionization of Argon*, Phys. Rev. Lett. **105**, 143002 (2010).

[14] M. Holler, F. Schapper, L. Gallmann and U. Keller, *Attosecond Electron Wave-Packet Interference Observed by Transient Absorption*, Phys. Rev. Lett. **106**, 123601 (2011).

[15] P. Eckle, A. N. Pfeiffer, C. Cirelli, A. Staudte, R. Doerner, H. G. Muller, M. Buettiker and U. Keller, *Attosecond Ionization and Tunneling Delay Time Measurements in Helium*, Science **322**, 1525–1529 (2008).

[16] C. P. J. Martiny, M. Abu-Samha and L. B. Madsen, *Counterintuitive angular shifts in the photoelectron momentum distribution for atoms in strong few-cycle circularly polarized laser pulses*, J. Phys. B: At. Mol. Opt. Phys. **42** (2009).

[17] V. S. Yakovlev, J. Gagnon, N. Karpowicz and F. Krausz, *Attosecond Streaking Enables the Measurement of Quantum Phase*, Phys. Rev. Lett. **105**, 073001 (2010).

[18] P. M. Paul, E. S. Toma, P. Breger, G. Mullot, F. Auge, P. Balcou, H. G. Muller and P. Agostini, *Observation of a Train of Attosecond Pulses from High Harmonic Generation*, Science **292**, 1689–1692 (2001).

[19] V. Véniard, R. Taïeb and A. Maquet, *Two-Color Multiphoton Ionization of Atoms Using High-Order Harmonic Radiation*, Phys. Rev. Lett. **74**, 4161–4164 (1995).

[20] S. Haessler, B. Fabre, J. Higuet, J. Caillat, T. Ruchon, P. Breger, B. Carré, E. Constant, A. Maquet, E. Mével, P. Salières, R. Taïeb and Y. Mairesse, *Phase-resolved attosecond near-threshold photoionization of molecular nitrogen*, Phys. Rev. A **80**, 011404 (2009).

[21] K. Varju, P. Johnsson, R. Lopez-Martens, T. Remetter, E. Gustafsson, J. Mauritsson, M. Gaarde, K. Schafer, C. Erny, I. Sola, A. Zair, E. Constant, E. Cormier, E. Mevel and A. L'Huillier, *Experimental studies of attosecond pulse trains*, Laser Phys. **15**, 888–898 (2005).

[22] F. Kelkensberg, W. Siu, J. F. Pérez-Torres, F. Morales, G. Gademann, A. Rouzée, P. Johnsson, M. Lucchini, F. Calegari, J. L. Sanz-Vicario, F. Martín and M. J. J. Vrakking, *Attosecond Control in Photoionization of Hydrogen Molecules*, Phys. Rev. Lett. **107**, 043002 (2011).

[23] L. Miaja-Avila, G. Saathoff, S. Mathias, J. Yin, C. L. o vorakiat, M. Bauer, M. Aeschlimann, M. M. Murnane and H. C. Kapteyn, *Direct Measurement of Core-Level Relaxation Dynamics on a Surface-Adsorbate System*, Phys. Rev. Lett. **101**, 046101 (2008).

[24] P. B. Corkum, *Plasma perspective on strong field multiphoton ionization*, Phys. Rev. Lett. **71**, 1994–1997 (1993).

[25] J. C. Baggesen and L. B. Madsen, *Theory for time-resolved measurements of laser-induced electron emission from metal surfaces*, Phys. Rev. A **78**, 032903 (2008).

[26] C.-H. Zhang and U. Thumm, *Attosecond Photoelectron Spectroscopy of Metal Surfaces*, Phys. Rev. Lett. **102**, 123601 (2009).

[27] A. K. Kazansky and P. M. Echenique, *One-Electron Model for the Electronic Response of Metal Surfaces to Subfemtosecond Photoexcitation*, Phys. Rev. Lett. **102**, 177401 (2009).

[28] C. Lemell, B. Solleder, K. Tőkési and J. Burgdörfer, *Simulation of attosecond streaking of electrons emitted from a tungsten surface*, Phys. Rev. A **79**, 062901 (2009).

[29] S. Gilbertson, X. Feng, S. Khan, M. Chini, H. Wang, H. Mashiko and Z. Chang, *Direct measurement of an electric field in femtosecond Bessel-Gaussian beams*, Opt. Lett. **34**, 2390–2392 (2009).

[30] J. Itatani, F. Quéré, G. L. Yudin, M. Y. Ivanov, F. Krausz and P. B. Corkum, *Attosecond Streak Camera*, Phys. Rev. Lett. **88**, 173903 (2002).

[31] Y. Mairesse and F. Quéré, *Frequency-resolved optical gating for complete reconstruction of attosecond bursts*, Phys. Rev. A **71**, 011401(R) (2005).

[32] J. M. Schins, P. Breger, P. Agostini, R. C. Constantinescu, H. G. Muller, G. Grillon, A. Antonetti and A. Mysyrowicz, *Observation of Laser-Assisted Auger Decay in Argon*, Phys. Rev. Lett. **73**, 2180–2183 (1994).

[33] M. Drescher, M. Hentschel, R. Kienberger, M. Uiberacker, V. Yakovlev, A. Scrinzi, T. Westerwalbesloh, U. Kleineberg, U. Heinzmann and F. Krausz, *Time-resolved atomic inner-shell spectroscopy*, Nature (London) **419**, 803–807 (2002).

[34] P. M. Echenique and J. B. Pendry, *Theory of image states at metal surfaces*, Progress in Surface Science **32**, 111–159 (1989).

[35] U. Hofer, I. L. Shumay, C. Reuss, U. Thomann, W. Wallauer and T. Fauster, *Time-Resolved Coherent Photoelectron Spectroscopy of Quantized Electronic States on Metal Surfaces*, Science **277**, 1480–1482 (1997).

[36] S. Link, H. A. Dürr and W. Eberhardt, *Lifetimes of image-potential states on the Pt(111) surface probed by time-resolved two-photon photoemission spectroscopy*, Applied Physics A: Materials Science & Processing **71**, 525–528 (2000).

[37] N. W. Ashcroft and N. D. Mermin, *Solid State Physics* (Thomson Learning, 1976).

[38] N. E. Christensen and B. Feuerbacher, *Volume and surface photoemission from tungsten. I. Calculation of band structure and emission spectra*, Phys. Rev. B **10**, 2349–2372 (1974).

[39] A. Zangwill, *Physics at Surfaces* (Cambridge University Press, 1988).

[40] C.-H. Zhang and U. Thumm, *Erratum: Attosecond Photoelectron Spectroscopy of Metal Surfaces [Phys. Rev. Lett. 102, 123601 (2009)]*, Phys. Rev. Lett. **103**, 239902 (2009).

[41] J. C. Baggesen and L. B. Madsen, *Secondary-electron cascade in attosecond photoelectron spectroscopy from metals*, Phys. Rev. A **80**, 030901(R) (2009).

[42] C. N. Berglund and W. E. Spicer, *Photoemission Studies of Copper and Silver: Theory*, Phys. Rev. **136**, A1030–A1044 (1964).

[43] P. A. Wolff, *Theory of Secondary Electron Cascade in Metals*, Phys. Rev. **95**, 56–66 (1954).

[44] E. Merzbacher, *Quantum Mechanics* (Wiley, second edition, 1970).

[45] L. Holmegaard, J. H. Nielsen, I. Nevo, H. Stapelfeldt, F. Filsinger, J. Küpper and G. Meijer, *Laser-Induced Alignment and Orientation of Quantum-State-Selected Large Molecules*, Phys. Rev. Lett. **102**, 023001 (2009).

[46] S. De, I. Znakovskaya, D. Ray, F. Anis, N. G. Johnson, I. A. Bocharova, M. Magrakvelidze, B. D. Esry, C. L. Cocke, I. V. Litvinyuk and M. F. Kling, *Field-Free Orientation of CO Molecules by Femtosecond Two-Color Laser Fields*, Phys. Rev. Lett. **103**, 153002 (2009).

[47] B. H. Bransden and C. J. Joachain, *Physics of Atoms and Molecules; 2nd ed.* (Prentice Hall, Harlow, 2003).

[48] M. W. Schmidt, K. K. Baldridge, J. A. Boatz, S. T. Elbert, M. S. Gordon, J. H. Jensen, S. Koseki, N. Matsunaga, K. A. Nguyen, S. Su, T. L. Windus, M. Dupuis and J. A. M. Jr, *General atomic and molecular electronic structure system*, J. Comp. Chem. **14**, 1347 (1993).

[49] E. P. Wigner, *Lower Limit for the Energy Derivative of the Scattering Phase Shift*, Phys. Rev. **98**, 145–147 (1955).

[50] C.-H. Zhang and U. Thumm, *Electron-ion interaction effects in attosecond time-resolved photoelectron spectra*, Phys. Rev. A **82**, 043405 (2010).

[51] A. S. Kheifets and I. A. Ivanov, *Delay in Atomic Photoionization*, Phys. Rev. Lett. **105**, 233002 (2010).

[52] S. Nagele, R. Pazourek, J. Feist, K. Doblhoff-Dier, C. Lemell, K. Tőkési and J. Burgdörfer, *Time-resolved photoemission by attosecond streaking: extraction of time information*, J. Phys. B **44**, 081001 (2011).

[53] J. Mauritsson, P. Johnsson, E. Gustafsson, A. L'Huillier, K. J. Schafer and M. B. Gaarde, *Attosecond Pulse Trains Generated Using Two Color Laser Fields*, Phys. Rev. Lett. **97**, 013001 (2006).

[54] N. Dudovich, O. Smirnova, J. Levesque, Y. Mairesse, M. Y. Ivanov, D. M. Villeneuve and P. B. Corkum, *Measuring and controlling the birth of attosecond XUV pulses*, Nat. Phys. **2**, 781–786 (2006).

[55] V. Véniard, R. Taïeb and A. Maquet, *Phase dependence of (N+1)-color (N>1) ir-uv photoionization of atoms with higher harmonics*, Phys. Rev. A **54**, 721–728 (1996).

[56] J. Caillat, A. Maquet, S. Haessler, B. Fabre, T. Ruchon, P. Salières, Y. Mairesse and R. Taïeb, *Attosecond Resolved Electron Release in Two-Color Near-Threshold Photoionization of $N2$*, Phys. Rev. Lett. **106**, 093002 (2011).

[57] C.-H. Zhang and U. Thumm, *Laser-assisted photoemission from adsorbate-covered metal surfaces: Time-resolved core-hole relaxation dynamics from sideband profiles*, Phys. Rev. A **80**, 032902 (2009).

[58] M. Abramowitz and I. A. Stegun, *Handbook of Mathematical Functions* (Dover Publications, 1970).

[59] L. B. Madsen, *Strong-field approximation in laser-assisted dynamics*, Am. J. of Phys. **73**, 57–62 (2005).

[60] L. Miaja-Avila, C. Lei, M. Aeschlimann, J. L. Gland, M. M. Murnane, H. C. Kapteyn and G. Saathoff, *Laser-Assisted Photoelectric Effect from Surfaces*, Phys. Rev. Lett. **97**, 113604 (2006).

[61] G. Saathoff, L. Miaja-Avila, M. Aeschlimann, M. M. Murnane and H. C. Kapteyn, *Laser-assisted photoemission from surfaces*, Phys. Rev. A **77**, 022903 (2008).

[62] L. Miaja-Avila, J. Yin, S. Backus, G. Saathoff, M. Aeschlimann, M. M. Murnane and H. C. Kapteyn, *Ultrafast studies of electronic processes at surfaces using the laser-assisted photoelectric effect with long-wavelength dressing light*, Phys.Rev. A **79**, 030901(R) (2009).

[63] R. W. Boyd, *Nonlinear Optics, third edition* (Elsevier, Amsterdam, 2008).

[64] M. B. Gaarde, C. Buth, J. L. Tate and K. J. Schafer, *Transient absorption and reshaping of ultrafast XUV light by laser-dressed helium*, Phys. Rev. A **83**, 013419 (2011).

[65] R. Santra, V. S. Yakovlev, T. Pfeifer and Z.-H. Loh, *Theory of attosecond transient absorption spectroscopy of strong-field-generated ions*, Phys. Rev. A **83**, 033405 (2011).

[66] H. Friedrich, *Theoretical Atomic Physics, second edition* (Springer, Berlin, 1998).

[67] S. Pabst, L. Greenman, P. J. Ho, D. A. Mazziotti and R. Santra, *Decoherence in Attosecond Photoionization*, Phys. Rev. Lett. **106**, 053003 (2011).

[68] J. Breidbach and L. S. Cederbaum, *Universal Attosecond Response to the Removal of an Electron*, Phys. Rev. Lett. **94**, 033901 (2005).

[69] T. Mooney, E. Lindroth, P. Indelicato, E. Kessler and R. D. Deslattes, *Precision measurement of K and L transitions in xenon: Experiment and theory for the K, L, and M levels*, Phys. Rev. A **45**, 1531 (1992).

[70] P. Indelicato and E. Lindroth, *Relativistic effects, correlation and QED corrections on $K\alpha$ transitions in medium to very heavy atoms*, Phys. Rev. A **46**, 2426–2436 (1992).

[71] P. Indelicato, S. Boucard and E. Lindroth, *Relativistic and many-body effects in K, L, and M shell ionization energy for elements with* $10 \leq Z \leq 100$ *and the determination of the 1s Lamb shift for heavy elements*, Eur. Phys. J. D **3**, 29–41 (1998).

[72] M. Lein, N. Hay, R. Velotta, J. P. Marangos and P. L. Knight, *Role of the Intramolecular Phase in High-Harmonic Generation*, Phys. Rev. Lett. **88**, 183903 (2002).

[73] R. Torres, N. Kajumba, J. G. Underwood, J. S. Robinson, S. Baker, J. W. G. Tisch, R. de Nalda, W. A. Bryan, R. Velotta, C. Altucci, I. C. E. Turcu and J. P. Marangos, *Probing Orbital Structure of Polyatomic Molecules by High-Order Harmonic Generation*, Phys. Rev. Lett. **98**, 203007 (2007).

[74] O. Smirnova, Y. Mairesse, S. Patchkovskii, N. Dudovich, D. Villeneuve, P. Corkum and M. Y. Ivanov, *High harmonic interferometry of multi-electron dynamics in molecules*, Nature (London) **460**, 972–977 (2009).

[75] Y. Mairesse, J. Higuet, N. Dudovich, D. Shafir, B. Fabre, E. Mével, E. Constant, S. Patchkovskii, Z. Walters, M. Y. Ivanov and O. Smirnova, *High Harmonic Spectroscopy of Multichannel Dynamics in Strong-Field Ionization*, Phys. Rev. Lett. **104**, 213601 (2010).

[76] S. Baker, J. Robinson, C. Haworth, H. Teng, R. Smith, C. Chirila, M. Lein, J. Tisch and J. Marangos, *Probing proton dynamics in molecules on an attosecond time scale*, Science **312**, 424–427 (2006).

[77] C. B. Madsen, M. Abu-samha and L. B. Madsen, *High-order harmonic generation from polyatomic molecules including nuclear motion and a nuclear modes analysis*, Phys. Rev. A **81**, 043413 (2010).

[78] J. Itatani, J. Levesque, D. Zeidler, H. Niikura, H. Pepin, J. C. Kieffer, P. B. Corkum and D. M. Villeneuve, *Tomographic imaging of molecular orbitals*, Nature (London) **432**, 867 (2004).

[79] D. Shafir, Y. Mairesse, D. M. Villeneuve, P. B. Corkum and N. Dudovich, *Atomic wavefunctions probed through strong-field light-matter interaction*, Nature Phys. **5**, 412–416 (2009).

[80] B. Sundaram and P. W. Milonni, *High-order harmonic generation: Simplified model and relevance of single-atom theories to experiment*, Phys. Rev. A **41**, 6571–6573 (1990).

[81] J. H. Eberly and M. V. Fedorov, *Spectrum of light scattered coherently or incoherently by a collection of atoms*, Phys. Rev. A **45**, 4706–4712 (1992).

[82] D. G. Lappas, M. V. Fedorov and J. H. Eberly, *Spectrum of light scattered by a strongly driven atom*, Phys. Rev. A **47**, 1327–1335 (1993).

[83] K. Burnett, V. C. Reed, J. Cooper and P. L. Knight, *Calculation of the background emitted during high-harmonic generation*, Phys. Rev. A **45**, 3347–3349 (1992).

[84] D. J. Diestler, *Harmonic generation: Quantum-electrodynamical theory of the harmonic photon-number spectrum*, Phys. Rev. A **78**, 033814 (2008).

[85] A. D. Bandrauk, S. Chelkowski, S. Kawai and H. Lu, *Effect of Nuclear Motion on Molecular High-Order Harmonics and on Generation of Attosecond Pulses in Intense Laser Pulses*, Phys. Rev. Lett. **101**, 153901 (2008).

[86] J. Zhao and Z. Zhao, *Probing H_2^+ vibrational motions with high-order harmonic generation*, Phys. Rev. A **78**, 053414 (2008).

[87] P. B. Corkum, *Plasma perspective on strong field multiphoton ionization*, Phys. Rev. Lett. **71**, 1994–1997 (1993).

[88] J. Tate, T. Auguste, H. G. Muller, P. Salières, P. Agostini and L. F. DiMauro, *Scaling of Wave-Packet Dynamics in an Intense Midinfrared Field*, Phys. Rev. Lett. **98**, 013901 (2007).

[89] M. Y. Ivanov, T. Brabec and N. Burnett, *Coulomb corrections and polarization effects in high-intensity high-harmonic emission*, Phys. Rev. A **54**, 742–745 (1996).

[90] M. Lein, N. Hay, R. Velotta, J. P. Marangos and P. L. Knight, *Role of the Intramolecular Phase in High-Harmonic Generation*, Phys. Rev. Lett. **88**, 183903 (2002).

[91] J. Levesque, D. Zeidler, J. P. Marangos, P. B. Corkum and D. M. Villeneuve, *High Harmonic Generation and the Role of Atomic Orbital Wave Functions*, Phys. Rev. Lett. **98**, 183903 (2007).

[92] E. P. Fowe and A. D. Bandrauk, *Nonlinear time-dependent density-functional-theory study of ionization and harmonic generation in CO_2 by ultrashort intense laser pulses: Orientational effects*, Phys. Rev. A **81**, 023411 (2010).

[93] R. Loudon, *The quantum theory of light* (Clarendon Press, Second Edition, Oxford, 1983).

[94] Y.-C. Han and L. B. Madsen, *Comparison between length and velocity gauges in quantum simulations of high-order harmonic generation*, Phys. Rev. A **81**, 063430 (2010).

[95] A. D. Bandrauk, S. Chelkowski, D. J. Diestler, J. Manz and K.-J. Yuan, *Quantum simulation of high-order harmonic spectra of the hydrogen atom*, Phys. Rev. A **79**, 023403 (2009).

[96] M. Lein, N. Hay, R. Velotta, J. P. Marangos and P. L. Knight, *Interference effects in high-order harmonic generation with molecules*, Phys. Rev. A **66**, 023805 (2002).

[97] T. Kanai, S. Minemoto and H. Sakai, *Quantum interference during high-order harmonic generation from aligned molecules*, Nature **435**, 470–474 (2005).

[98] C. Vozzi, F. Calegari, E. Benedetti, J.-P. Caumes, G. Sansone, S. Stagira, M. Nisoli, R. Torres, E. Heesel, N. Kajumba, J. P. Marangos, C. Altucci and R. Velotta, *Controlling Two-Center Interference in Molecular High Harmonic Generation*, Phys. Rev. Lett. **95**, 153902 (2005).

[99] M. B. Gaarde, J. L. Tate and K. J. Schafer, *Macroscopic aspects of attosecond pulse generation*, J. Phys. B: At. Mol. Opt. Phys. **41**, 132001 (2008).

[100] B. W. Shore and K. C. Kulander, *Generation of Optical Harmonics by Intense Pulses of Laser Radiation – I. Propagation Effects*, Journal of Modern Optics **36**, 857–875 (1989).

[101] E. Constant, D. Garzella, P. Breger, E. Mevel, C. Dorrer, C. L. Blanc, F. Salin and P. Agostini, *Optimizing high harmonic generation in absorbing gases: Model and experiment*, Phys. Rev. Lett. **82**, 1668 (1999).

[102] C. Jin, A.-T. Le and C. D. Lin, *Medium propagation effects in high-order harmonic generation of Ar and N_2*, Phys. Rev. A **83**, 023411 (2011).

[103] A. S. Sandhu, E. Gagnon, A. Paul, I. Thomann, A. Lytle, T. Keep, M. M. Murnane, H. C. Kapteyn and I. P. Christov, *Generation of sub-optical-cycle, carrier-envelope-phase–insensitive, extreme-uv pulses via nonlinear stabilization in a waveguide*, Phys. Rev. A **74**, 061803(R) (2006).

[104] T. Tuchon, C. P. Hauri, K. Varjú, E. Mansten, M. Swoboda, R. Lopez-Martens and A. L'Huillier, *Macroscopic effects in attosecond pulse generation*, New J. Phys. **10**, 025027 (2008).

[105] J. P. Farrell, L. S. Spector, B. K. McFarland, P. H. Bucksbaum, M. Guhr, M. B. Gaarde and K. J. Schafer, *Influence of phase*

matching on the Cooper minimum in Ar high-order harmonic spectra, Phys. Rev. A **83**, 023420 (2011).